Pulsed plasma synthesis of Si and SiGe nanocrystals

Akshatha Mohan

The cover is locally enhanced plasma formed at the holes in the grounded grid electrode in the PECVD (plasma enhanced chemical vapour deposition) system ASTER (Amorphous silicon thin film experimental reactor). Image credit, Arjen de Waal.

ISBN 978-90-393-6814-5

Pulsed plasma synthesis of Si and SiGe nanocrystals

Synthese van nanokristallen van Si en SiGe in een pulserend plasma

(met een samenvatting in het Nederlands)

Proefschrift

ter verkrijging van de graad van doctor aan de Universiteit Utrecht
op gezag van de rector magnificus, prof.dr. G.J. van der Zwaan,
ingevolge het besluit van het college voor promoties
in het openbaar te verdedigen op
maandag 28 augustus 2017
des middags te 4.15 uur

door

Akshatha Mohan

geboren te Mysore, India

Promotoren: Prof.dr. R.E.I. Schropp

Prof.dr. J.K. Rath

This research is a part of the Joint Solar Programme (JSP) of Hyet Solar and the Stichting voor Fundamenteel Onderzoek der Materie (FOM), which is part of the Netherlands Organisation for Scientific Research (NWO), project 09JSP50: Quantum dot based thin film silicon solar cell

To Amma & Appa...

Contents

Chapter 1: Introduction

Abstract

The main objective of the thesis is to synthesize non embedded, free standing Si and SiGe nanoparticles in the gas phase in a single step in a dedicated plasma reactor. The characterization of the synthesized nanoparticles and attaining the optimum plasma parameter space for their synthesis is central to this thesis.

In this chapter an overview of the various reports on plasma synthesis of Si and SiGe nanoparticles is provided. One section is dedicated to highlight the advantages of plasma synthesis of nanoparticles. More importantly, the potential applications of these non-toxic particles made from abundant elements are discussed.

The outline summarizes the main results of this thesis.

1.1 Silicon and silicon germanium nanoparticles

Currently bulk crystalline silicon (c-Si) is the unrivalled material in the modern technological era making it indispensable in microelectronics and photovoltaic industry. Silicon, apart from being naturally abundant, is also non-toxic and stable under ambient conditions. Its well-studied semiconducting properties, high electronic quality and its ability to be doped with group III and V elements to effectively control their conductivity makes Si unprecedented for electronic applications. However, the same cannot be said about its optical applications; the band gap, though favorable for absorption in the visible region, is less than the optimum value as its absorption is hindered by its indirect band structure, which occurs via phonon-photon coupling, making Si an inefficient absorber and poor emitter even at liquid He temperatures.

One well known way to enhance the optical properties of indirect band gap semiconductors is by downscaling them to their nanoscale counterparts. The indirect band gap structure of bulk silicon and direct band gap structure of nanostructured silicon is given in Fig. 1 (a) and (b) respectively. Band-gap engineering, by downscaling the size of Si to the nanometer dimension, has shown to be very effective in obtaining room temperature photoluminescence (PL) prominently observed in quantum dots (QDs) [1, 2]. QDs are materials with size less than the exciton Bohr radius, which is defined as the minimum natural separation between the electrons in the conduction band and their corresponding holes in the valence band. The exciton Bohr radius of silicon is 4.2 nm. When quantum confinement effects come into play, the semiconductor band gap can be engineered by varying the size of the QDs.

The band-gap energy of Si QDs can be described by “particle in a box” which renders strong size dependence, effectively leading to an increase in band gap [3, 4] as well as enhancement in PL efficiency [5]. Decreasing the size of the QD effectively leads to increasing the band gap (Fig. 1 (d)), hence by changing the size, PL emission can be tuned across a wide range. One possible reason for the observation of PL can be the quantum confinement which allows phonon-free optical transitions [5, 6, 4, 7]. Quantum confinement severely changes the properties of nanocrystals (NCs) compared to bulk material, because of the enhanced overlap between the electron and hole wave functions which increases radiative recombination probability [8]. In addition, improved emission occurs due to a decrease in non-radiative recombination events, which diminish as compared to bulk silicon as small mid-gap defects and impurities grow out of the dots as they are thermodynamically unfavorable [9]. The beneficial opto-electrical properties arising from quantum confinement can be harnessed in new fields of semiconductor applications.

Another group IV semiconductor that is currently experiencing revival due to its potential in opto-electronic hetero-structures with Si is germanium [10]. The optical

absorption coefficient and electron mobility of Ge surpasses that of Si [11, 12]. Additionally, as Ge has a higher value of dielectric constant, it has a larger exciton Bohr radius of 24.3 nm [13]. Therefore quantum confinement effect manifests itself even for relatively large Ge NCs.

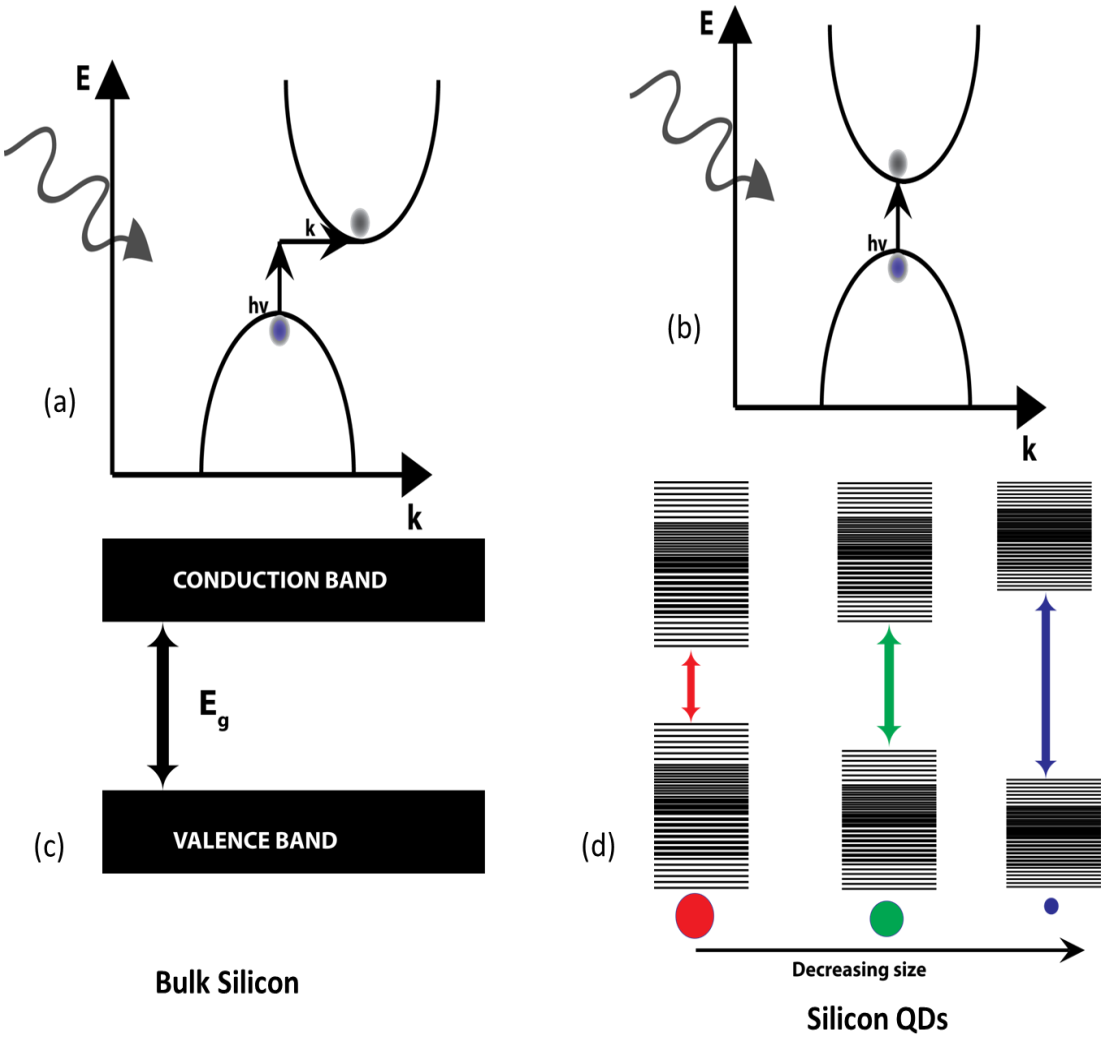

Fig. 1.1 (a) Indirect band gap structure of bulk c-Si (b) when Si is downscaled to nanometer regime, it leads to direct band gap like structure (c) fixed energy levels of macroscopic crystal (d) splitting of energy levels of Si QDs due to quantum confinement effect, the band gap increases with decreasing size of the NC.

Furthermore mixing Si and Ge together to make SiGe alloy NCs offers a whole new degree of freedom to tune their opto-electronic properties, by changing the relative contents of both materials. Alloy NCs can be used to meet multiple requirements of nanoparticle size and properties. Compositional variation of the alloy NCs alters the optical and physical properties, while maintaining a small size. For photovoltaic applications, SiGe alloys can be designed to absorb a wide range of the solar spectrum, by varying their composition.

The formation of powder in plasma is a sequence of four steps as shown in Fig. 1.2. QDs, the material of our interest, are polymerization precursors leading to powder, thus a significant part of the thesis is dedicated to understand the powder formation. Detailed review papers on the gas phase synthesis of Si NCs, highlighting the fundamental mechanisms of particle formation, size dependent features, and technological applications can be found in [14, 15, 16].

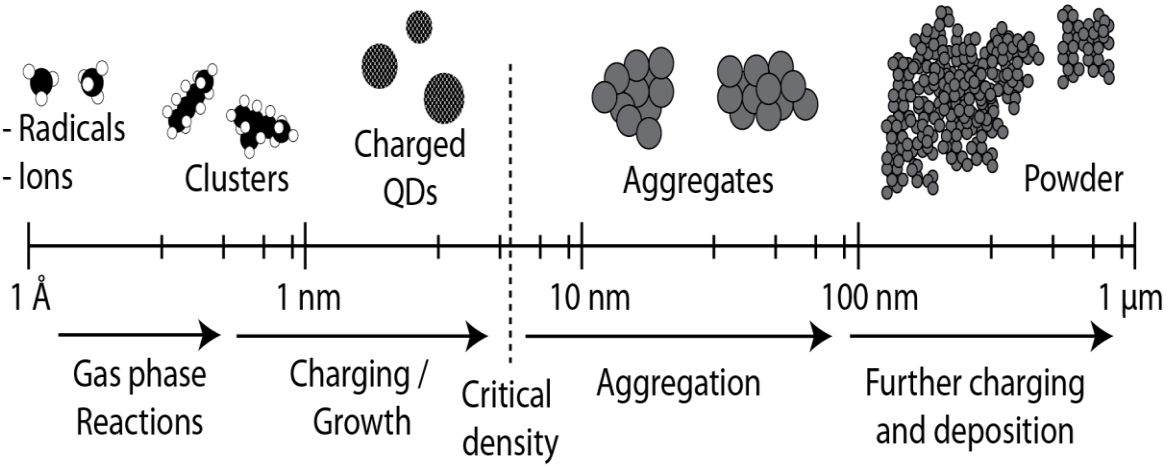

Fig. 1.2: Nucleation and growth of silane particles in a PECVD plasma, image credit [17].

1.2 Plasma synthesis of silicon and silicon germanium nanoparticles

Various techniques have been employed to synthesize Si nanocrystals and nanoparticles (NPs) such as sputtering [18, 19] ion implantation [20, 21], laser pyrolysis [4], solution synthesis [22, 23] and plasma deposition [24]. The main drawback of sputtering and ion implantation is that they require additional intensive heat treatments for inducing crystallization and the formed NC is bound in a host matrix restricting their ease of handling and manipulation. For instance, to obtain free standing Si NCs from these matrices, the surrounding medium must be removed by etching, bringing an extra post-production step. Additional steps of post annealing to induce crystallization and etching the matrix surrounding the NC and the inherent low throughput of the processes makes this method unattractive for large scale applications. Laser pyrolysis does not have this drawback but suffers from rapid particle agglomeration as the particles are usually electrically neutral. For instance, Borsella *et al.* [25] reported a particle size distribution with particle sizes ranging between 1-100 nm for their laser pyrolysis process. Solution synthesis routes on the other hand offer excellent size control capable of producing free-standing luminescent NCs. Nonetheless, the lengthy reaction times (typically requiring several hours) and multiple steps involved together with very low production rates makes them non-viable for mass production [26]. Also solution synthesis, especially for group III-V and group IV semiconductors with high melting point is limited by the boiling point of the solvents.

Plasma processes inherently capable of high temperatures have an edge for the production of the nanostructures requiring high temperatures for their crystallization.

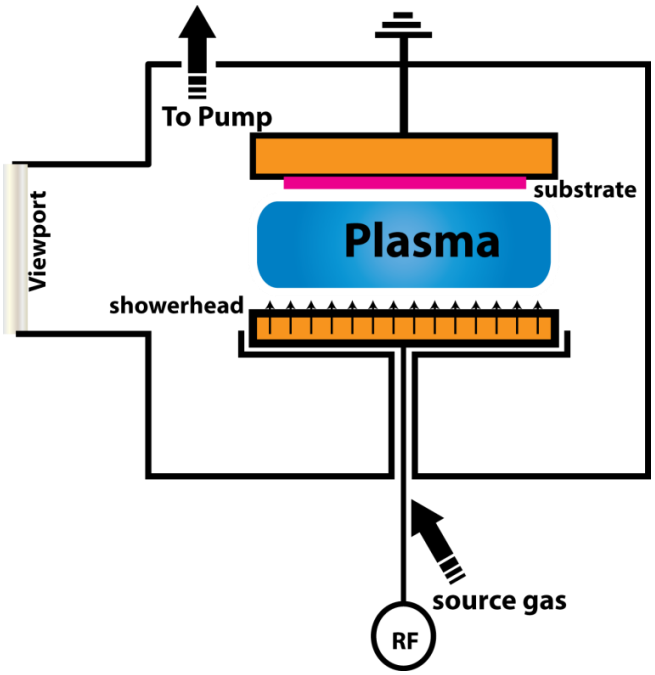

Fig. 1.3 Schematic diagram of a PECVD reactor, with plasma between the top grounded electrode and the bottom powered electrode. In this case, source gas is fed in to the bottom shower head electrode and substrate is mounted on the grounded electrode. The viewport is used to do optical diagnostics.

Plasma-assisted gas phase processes have the potential to overcome the aforementioned disadvantages. An example of a schematic plasma reactor is given in Fig. 1.3. In the following section we highlight the advantages of gas phase plasma processes to produce free standing; i.e, non-agglomerated and non-embedded Si NCs with precise size control in a single step. We will extend this technique also for fabricating SiGe alloy NCs.

Reports on alloying of NCs in the gas phase, especially Si and Ge, is sparse. Limited reports include non-thermal plasma to produce free standing SiGe alloy NCs [27]. SiGe alloy NCs have been produced using germanium tetrachloride in non-thermal plasma reactor which is cheaper and safer alternative to germane (GeH_4) [28]. SiGe alloy NC inks without any ligands have also been produced by laser pyrolysis [29]. SiGe inks are SiGe NPs distributed in a stable dispersion followed by sonication and filtration. SiGe alloy NCs have been synthesized in two-stage hot wall aerosol reactor, the first reactor produces Si seed particles, which are fed into the second reactor where a mixture of silane (SiH_4) and GeH_4 are added [30]. The desired morphology and composition is obtained by changing the composition of the gases or the partial pressure. In this study we will show that we have been successful in producing SiGe alloy NCs with excellent control of their size and composition.

1.2.1 Tuning particle size and crystallinity

Once a regime for Si NC formation in a plasma deposition process is identified, a wide range of recipes can be adapted by altering the plasma parameters to modify the Si NC morphology and crystallinity. Precise size control of nanoparticles (NPs) can be obtained by varying the gas residence time in the discharge region or by pulsing the RF power ON (t_{ON}) and OFF times (t_{OFF}). Varying the flow rate is used as a tool to control the size and size dispersion of the NCs in continuous plasma [31]. Particle growth can be controlled by varying the plasma ON time, for example NCs with sizes less than 2 nm with a size dispersion of 0.4 nm were obtained in a pulsed plasma [32]. As a consequence the PL spectra can be tuned, by changing the t_{ON} [33].

Particle crystallinity can also be tuned by changing the ratio of precursor gases SiH_4:H_2, changing the plasma power, or the gas residence time. A detailed study of the effects of these parameters to tailor the NC size and crystallinity is provided in Chapter 5.

1.2.2 High throughput

The plasma process promises to deliver one of the highest throughputs among other synthesis methods. Recently, high yield techniques of gas phase synthesis of luminescent Si nanocrystals in low pressure non-thermal plasma, which has a process yield of 14–52 mg h^{-1} [34], and in an expanding thermal plasma, which has a yield of 600 mg h^{-1} [24]have been reported. CO_2 laser induced pyrolysis of silane was used to produce Si nanoparticles at high rates (20-200 mg h^{-1}) [35].

1.2.3 Surface functionalization and passivation

The production of bare particles in a plasma gives the opportunity to apply various surface functionalizations. Attaching organic monolayers to the surface of the NC is required to impart solubility in a variety of solvents, which is useful for a range of applications and stabilizes the PL properties against degradation [36, 37]. A high quantum yield of more than 60% was obtained for NCs functionalized with organic ligands [38, 39]. Molecules attached to the NC surface contribute to passivating dangling bonds which are sites for non-radiative recombination process which causes quenching of PL [40]. All-gas phase functionalization and passivation of Si NC has also successfully been demonstrated using the two-stage plasma approach with the ability to attach a wide range of grafting molecules [41]. Si NCs are synthesized in the first non-thermal plasma reactor and dragged into the second reactor. In the second reactor, surface functionalization is performed by plasma assisted in-flight grafting of organic molecules. Reactive radicals of the organic ligands are formed through electron impact dissociation, which enables the reaction of the organic ligands with

the surface of the silicon NCs. Using a two-stage plasma process, in flight etching of NC to obtain the desired size and luminescence across the entire optical spectrum has been shown [42, 43]. An example of functionalization of hydrogen terminated Si NPs by hydrosilylation with organic ligands is given in Fig. 1.4.

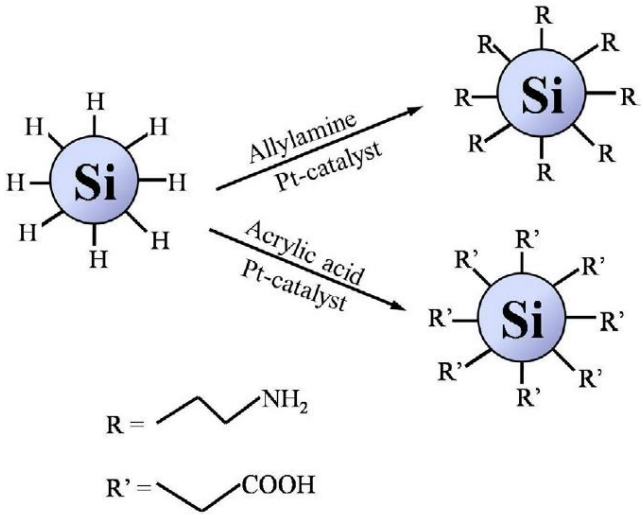

Fig. 1.4: Functionalization of hydrogen terminated Si NPs by hydrosilylation reaction using allylamine and acrylic acid (Image credit [44]*).*

1.2.4 Integration into nanoscale devices

Implementation of Si QDs in nanoscale device structures has met with enormous technical challenges, hence there are only a few reports so far. S. Oda's group has fabricated single electron transistors [45, 46] and cold electron emitters [47] from plasma produced NCs. Plasma produced cubic silicon NCs have been used to synthesize nanoparticle based vertical transistors [48] which could provide a new paradigm in nanoelectronic devices.

1.2.5 Particle charging and particle heating

Particles immersed in the plasma are usually unipolar and negatively charged, due to the higher electron temperature and mobility compared to ions. This unipolar charge resulting in mutual repulsion retards the rate of coagulation, leading to a narrow size distribution [49, 50]. NCs in the plasma experience intense heating through energetic reactions on their surface such as electron-ion recombination and hydrogen recombination reactions. Selective NC heating leads to particle temperatures of up to 900 K and it plays a

crucial role in particle crystallization in plasmas [34, 14]. NPs immersed in low temperature plasma (where the gas temperature is close to room temperature) attain crystallization temperatures, which is referred to as selective NC heating. Particle charging and selective nanoparticle heating makes plasma an attractive tool to overcome coagulation and obtain crystalline particles in our case and is highlighted in Chapter 4 and 5 respectively. This also enables processing even at room temperatures. These advantages make plasma processing of NCs both scientifically appealing and commercially viable.

1.3 Potential applications of silicon and silicon germanium nanoparticles

The size dependent band gap of Si makes it a desirable candidate for light emitting diode applications where different colors of the spectrum can be realized using the same material [34, 51]. In the earlier section we already mentioned the application of Si NCs in nanoelectronic devices such as single electron transistors which can be integrated into devices. Si and SiGe NCs also exhibit size dependent improvements in dielectric constants, charge storing capacity and surface reactivity making them strong candidates for potential applications other than solar cells, listed below.

1.3.1 Battery applications

Si is an attractive anode material in lithium ion batteries owing to its exceptionally high charge storage capacity. Volume expansion causes enormous mechanical stress in a brittle material during lithiation, which leads to loss of charge retention. Unique micromechanics of nanostructured Si can overcome this drawback, as these nanostructures have high reversible life cycles and increased surface to volume ratio. Such small dimensions do not permit the micromechanical and deformation processes that happen in bulk [52] [53].

1.3.2 Photovoltaic applications

Silicon NCs are of interest for potential applications in photovoltaics because bulk silicon dominates the commercial solar cell market. The most crucial power loss mechanisms in single-bandgap solar cells (inability to absorb photons with energy less than the band gap and thermalization of photons above the band gap) can be overcome by third generation concepts of tandem cells and spectral conversion [54]. In the first concept, Si NCs by virtue of their size dependent band gap energy can achieve higher efficiencies by absorbing light from a wider solar spectrum. Third-generation QD solar cells show the potential to engineer the band gap and theoretically, 42.5% and 47.5% for two-cell and

three-cell tandem stacks, respectively, can be achieved compared with 29% for a single junction Si cell, according to the S–Q limit [55]. A potential schematic diagram of two cell tandem solar cell incorporating Si and SiGe NCs is given in Fig. 1.5.

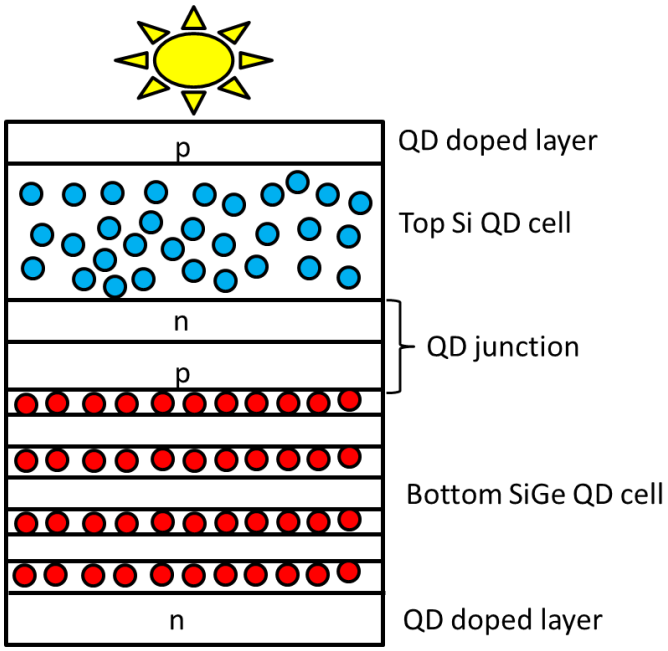

Fig. 1.5: Schematic of a two cell tandem solar cell using Si and SiGe NCs to harness a wider solar spectrum with a judicious combination the two materials.

In the second concept, NCs can be utilized for advanced photon management (up and down conversion). Upconversion is the process of single exciton generation with multiple low energy photons and down conversion is the process of multiple exciton generation after absorption of a single high-energy photon. For instance, incorporation of Si-QDs as down-shifting material on the window side of a c-Si solar cell improves the photocurrent generation and the power conversion efficiency increases from 11.90 to 13.37% [56].

1.3.3 Biological applications

Si QDs are significantly less toxic alternative to the conventional existing QDs such as cadmium compounds which are known to be toxic and thus unsuitable for biological applications. Recently Si QDs are emerging as fluorescent probes for many biological applications, particularly for cellular imaging [57]. The tunable fluorescence signatures, the high PL quantum efficiency, and the stability against photobleaching make the silicon NCs ideal candidates for substituting the fluorescent dyes in some biological assays and fluorescence imaging techniques [58]. For instance, water-dispersible Si QDs have been demonstrated to be robustly taken up by pancreatic cancer cells and used for live cell imaging [59]. Si QDs can thus be used as non-toxic optical probes for biomedical applications.

1.3.4 Thermoelectric materials

Thermoelectric devices, which involve conversion of thermal energy into electricity are expected to play an important role in conversion of waste heat into electricity to improve the efficiency of thermal cycles and in cooling applications. Thermoelectric device efficiency ZT is given by $ZT = S^2\sigma T/k$, where σ is the electrical conductivity, S is the Seebeck coefficient, k is the thermal conductivity, and T is the absolute temperature. For a successful thermoelectric device, the value of ZT should be well in excess of unity, in other words a material with high electrical conductivity and low thermal conductivity is desired. The thermal conductivity can be reduced by employing thin films of nanomaterials as grain boundaries and interfaces in these films can induce phonon scattering, reducing thermal conductivity and improving thermoelectric performance [60, 61]. Highly doped NCs, especially those produced using plasmas, are promising candidates as building blocks for thin film-based thermoelectric devices [61, 62]. An impressive thermoelectric figure of merit value (ZT) of 1.84 is obtained for n-type SiGe nanostructured alloys. This high value is attributed to the reduction of the thermal conductivity caused by the scattering of low, medium, and high wavelength phonons by atomic size defects, dislocations, and grain boundaries that are present due to the formation of nanocrystalline grains in the bulk material [63].

1.4 Aim and Outline of the thesis

The main objective of this thesis is to design, construct, and integrate a new dedicated reactor in the existing VHF-PECVD system ASTER (more details in Chapter 2) where now a complete QD solar cell can be made. The proof of the concept of this reactor is provided by demonstrating a fast and simple technique to synthesize non embedded, free standing NCs in the gas phase in a single step. Our materials of interest in this thesis are Si and SiGe NCs. Using Si and SiGe QDs a wide variety of materials with optical absorption at different parts of the solar spectrum can be made. Thus, with a judicious combination of such materials a fuller solar spectrum can be harvested.

Chapter two introduces the main deposition and characterization techniques used for Si and SiGe NPs in this thesis. This includes VHF-PECVD (very high frequency-plasma enhanced chemical vapor deposition), OES (optical emission spectroscopy), VI (voltage-current) probe, TEM (transmission electron microscopy), HRTEM (high resolution TEM), HAADF-STEM (high-angle annular dark-field-scanning transmission electron microscope), EDS (energy dispersive x-ray spectroscopy), XRD (x-ray diffraction), and Raman Spectroscopy.

Chapter three is concerned with dust formation kinetics in silane hydrogen plasma by optical and electrical diagnostics. We were able to observe a periodic fluctuation in both emission intensity and electric current of the dusty plasma. The trends of frequency of fluctuations are studied as a function of substrate temperature and gas flow. However, we do not observe these fluctuations in non-dusty plasmas. We propose a hypothesis involving the periodic formation and ejection of the dust cloud. These experiments lay the foundation for following chapters where we estimate the appropriate time scales for pulsing the plasma for optimal NC production.

Chapter four focusses on the proof of the concept of the dedicated NP reactor by demonstrating the various ensembles of NPs formed in different plasma zones, including free standing quantum sized NPs. In addition, amorphous and aggregated NPs are also found. Optical and structural characterization results of these NPs are discussed. We highlight the importance of excess energetic electrons in the locally enhanced plasmas for the formation of free standing NPs.

Chapter five discusses plasma pulsing and the effect of pulsing time on the size, morphology and crystallinity of the NPs. Both plasma off time (t_{OFF}) and on times (t_{ON}) are discussed after characterizing plasma with time resolved OES and the NPs structurally and optically. t_{OFF} studies are done at various time scales with respect to the gas residence times and it is found that a t_{OFF} longer than the residence time is favorable for the growth of quantum sized NPs. With application of various t_{ON} periods, different phases of growth of NPs are studied, by means of extensive microscopic studies. The different phases are found to lead to NPs with different morphologies and crystallinity. We probe the polycrystalline cauliflower shaped NPs and hypothesize a growth mechanism according to which in the initial gas phase single polycrystalline particles are formed out of single nuclei which branch out and further grow epitaxially to form the cauliflower shaped NPs formed in the various plasma processes.

Chapter six is concerned with optimizing the parameter space to increase the crystallinity of the Si NPs in the gas phase growth process. Various plasma parameters such as the applied power and pressure are studied to investigate their effect on particle size, morphology and crystallinity. The highlight of this chapter is the focus on the effect of inter-electrode distance on particle size and crystallinity, which is sparsely studied so far. We establish how a larger inter-electrode distance opens up a wider parameter space for the synthesis of crystalline Si NPs.

Chapter seven is dedicated to the study of alloy SiGe NPs which has received meagre attention in VHF-PECVD plasmas. We have successfully synthesized highly crystalline and homogeneously alloyed SiGe NCs. NCs with size of 12 nm have been produced with remarkable control over their composition by altering the precursor GeH_4 gas flow. The homogeneous alloy composition has been verified by XRD, EDS and Raman yielding excellent consistency.

Chapter 2: Experimental methods

Abstract

The experimental techniques and concepts carried out for research within the scope of this thesis are described in this chapter. The first section presents Si and SiGe nanoparticle synthesis using plasma enhanced chemical vapor deposition in the ASTER system. Nanoparticle characterization techniques used for optical and structural probing such as Raman spectroscopy, X-ray diffraction and transmission electron microscopy are explained in the second section.

In addition, optical and electrical plasma characterization methods (optical emission spectroscopy and current-voltage (VI) probe, respectively) are reported in the third section.

2.1 Nanoparticle synthesis: plasma enhanced chemical vapor deposition

Plasma based surface processes are indispensable for manufacturing large area electronic devices and processing large scale integrated circuits (ICs) for the microelectronics industry. Plasma-enhanced chemical vapor deposition (PECVD) has been an important technique for thin film depositions and recently it has been applied for the synthesis and surface modification of nanostructured materials for optoelectronics and photovoltaic applications.

The plasma process in a PECVD is sustained between two electrodes and is driven by a RF power supply, a very high frequency (VHF) of 60 MHz in our case. The powered electrode is connected to the RF generator through an impedance matching network, which adapts the impedance of the power source to ensure optimal energy transfer to the discharge. The other electrode is the grounded electrode. The substrate is mounted on the grounded or the powered electrode depending on the purpose of the process (deposition and etching respectively) due to the difference in the energy of positive ions reaching the electrodes [64].

As these discharges are electrically driven, the applied power preferentially heats the mobile electrons, while the ions due to their heavy mass, exchange energy by collision with the background gas, hence $T_e >> T_i$, where T_e and T_i are the electron and ion temperature. Accelerated electrons in the oscillating electric field dissociate the feedstock gas, ionize a gas molecule thereby creating an extra free electron which in turn collides with another molecule, for example,

$$\mathrm{SiH_4 + e^- \rightarrow SiH_3^+ + H + 2e^-} \qquad \text{Eq. (2.1)}$$

This avalanche of reactions will result in a plasma containing positive ions and free electrons. A steady state is reached when the loss of charged particles to the reactor wall is balanced by their production [65]. The radical and ionic species formed contribute to the growth of the layer.

Plasmas in capacitively coupled reactor can be divided into two regions, the *bulk plasma* (in the center between the electrodes) and the *sheath* (the positive space charge region close to the electrodes). To explain the electrical properties, let us consider a quasi-neutral plasma, i.e., a plasma having nearly equal density of positive ions and electrons ($n_i \approx n_e$). As the net charge density $\rho = e\,(n_i - n_e)$ is zero, the electric potential ϕ and the electric field E_x is zero. As the thermal velocity of the electrons is at least 100 times that of ions (at the same temperature) diffusion coefficient is higher for electrons. Fast moving electrons are lost to the walls leading to an imbalance between the electron and ion

densities that in turn causes charge separation and creates an electric field which compensates the difference in electron and ion velocity. The electric field acts to slow the electrons and speed up the ions until both diffuse at the same rate. The resulting diffusion is called ambipolar diffusion, because both charged species (ambi means both) diffuse together. This leads to a potential profile which is positive in the bulk of the plasma and falls sharply to zero near the walls (Fig. 2.1). This potential, known as the plasma potential $V_{p,}$ confines the electrons to the bulk of the plasma and accelerates the ions from the plasma that enter the sheath towards the electrodes. This yields energetic ion bombardment on the electrodes. Electrons are expelled from the sheath, so all the ionization and dissociation processes must occur in the bulk. Hence plasma emission due to the excited molecules is mainly present in the bulk. In most systems, the grounded area (which includes the grounded electrode and the walls of the reactor) is larger than the powered electrodes. This asymmetric configuration results in a negative DC self-bias voltage V_{DC} on the powered electrode. The difference in electrode areas would result in a net electron current per RF period which is prohibited by a negative DC shift [66].

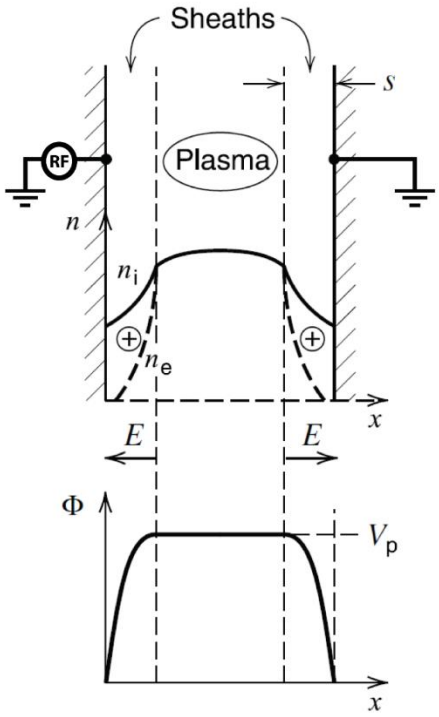

Fig. 2.1: Schematic diagram of average densities, electric field, and potential after the formation of sheaths, taken from [64]

2.1.1 The ASTER deposition system

Most of the experimental results in this thesis are obtained using the ultra-high vacuum multi-chamber deposition system ASTER (Amorphous Semiconductor Thin Film Experimental Reactor). This system features five deposition reactors, mounted to a central

transport chamber: one for p-type depositions (reactor 2), one for n-type depositions (reactor 3), two for intrinsic silicon depositions (reactor 1 & 4) and one dedicated reactor for nanoparticle (NP) deposition (reactor 5) (Fig. 2.2). The load lock and the robot arm ensure that samples are loaded and unloaded into the chamber without breaking vacuum in the deposition chambers. Substrates up to 10 × 10 cm^2 are mounted in a holder that is subsequently clamped to the upper grounded electrode. The holder including the substrate can be transported between the different chambers by means of the robot arm. Substrate temperatures between room temperature and 400^0C can be used. Power is supplied to the matching network with adjustable capacitors connected to the powered electrode. The matching network is tuned to match the impedance of the plasma reactor with the output impedance of the RF power supply.

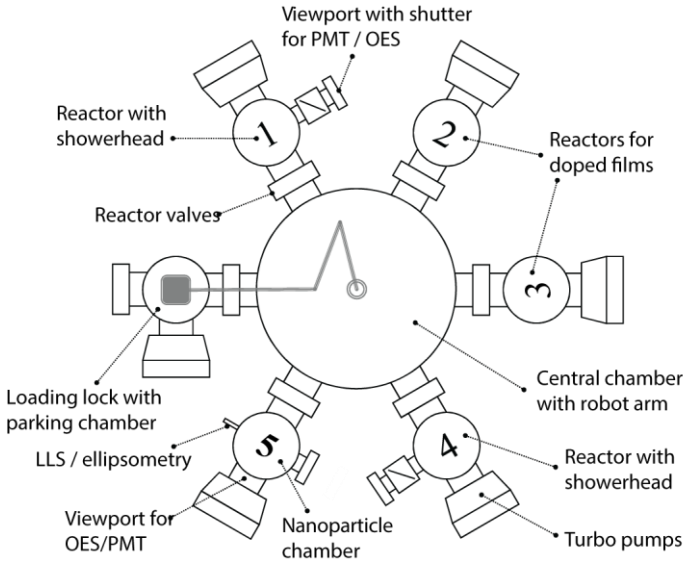

Fig. 2.2: Schematic top-view of the ASTER multi-chamber PECVD system [17].

The deposition chambers are equipped with viewports to monitor the plasma, either visually or using a spectrometer. Reactor 1 is used in this thesis for initial plasma studies, as it is equipped with a viewport for optical diagnostics and an MKS current-voltage (VI) probe for electrical diagnostics. In the intrinsic silicon chambers the inter-electrode distance can be changed from 5 to 27 mm. In the NP reactor (chamber 5) the inter-electrode distance can be changed from 5 to 25 mm. These reactors are equipped with showerhead-type powered electrodes, to secure homogeneous distribution of the feedstock gas into the plasma. The amount of reflected power (measured with a Rhode & Schwarz power meter) can be minimized to less than 5 % of the input power. Actual “coupled power” can be obtained from the VI probe. Potentially in this system a complete quantum dot solar cell can be fabricated.

To avoid oxygen and water contamination the background pressure needs to be several orders lower than the process pressure. The typical background pressure obtained is

in the order of 10^{-8} mbar. To reach this vacuum level the reactor is constructed of stainless steel with copper sealed flanges, viewports, and feedthroughs. The pumping system for each reactor consists of a turbo molecular pump backed by a rotary vane pump. The turbo molecular pump can be bypassed by closing a gate valve directly at the inlet of the turbo molecular pump and opening a valve in a by-pass line [67].

The background pressure is measured by a Penning type ionization gauge. The process pressure is measured by a capacitive membrane pressure gauge (Baratron) which measures the pressure (i.e. the force applied to the membrane) independent of the type of gas used.

The gas supply system consists of stainless steel tubes with metal sealed couplings. The gas flows are controlled by all-metal mass flow controllers. The gasses are mixed close to the shower head. The process pressure is controlled by adapting the pumping speed by means of a variable valve (VAT) in the bypass pumping line. Silane and germane are pyrophoric gasses which form solid oxide particles already at room temperature when in contact with oxygen. In the plasma solid semiconductor particles (clusters of Si and SiGe) can be formed. The rotary vane pump is equipped with an oil filter to pump gases and gas-borne particles. To dilute the exhaust gas to a silane and germane concentration < 1% and prevent backflow of air at the exhaust exit the exhaust line is permanently flushed with nitrogen.

2.2 Plasma characterization

In-situ diagnostic techniques are essential tools for any fabrication process. Here, they help to correlate material properties to plasma properties. This is particularly important for NPs formed in a dusty plasma, where the quality of the particles depends sensitively on the plasma parameters and reactor geometry. In industrial process, in-situ probes allow the processing to be aborted after a particular step if anything wrong is detected by in-situ diagnostics, thereby sparing the costs of further process steps [68].

2.2.1 Optical emission spectroscopy (OES)

OES is a non-invasive technique to probe the plasma which can provide spatial and temporal information (the set-up details can be found Fig. 3.3). The plasma emits light as various excited species undergo optical transitions in an electron impact excitation or dissociation giving rise to specific emission peaks. By measuring the wavelength and intensities of these peaks it is possible to identify and quantify certain species in the plasma. The emission peaks are like finger prints which give information about concentrations of light emitting species, the electron density, and the electron temperature. Quantitative analysis of emission spectra is complicated as the emission intensity from a specific species is proportional to its concentration, but the proportionality constant depends on the electron

density and the quantum efficiency of the excitation process. As the electron density depends on the RF power and the gas mixture, and the quantum efficiency on total pressure and gas mixture, the proportionality constant is never really a constant [69]. Also a direct intensity measurement always needs a calibration of the setup to a known intensity, which is difficult in a plasma chamber. Therefore, OES is used to provide insight on distinct emission energies and intensity ratios which are most often used in combination with empirical relations. For instance, the electron temperature can be determined by measuring the H_α/H_β ratio [70]. The Balmer lines associated with the dissociation of H_2 and the transition from n = 3 to n = 2 is called H_α and n = 4 to 2 is H_β.

A typical emission spectrum obtained for instance in a SiH_4 + H_2 plasma is given in Fig. 2.3. The emission from Si* and SiH* (emitting at 289 and 414 nm, respectively) are associated with the dissociation of SiH_4 whereas the Balmer H_α (656 nm) and H_β (490 nm) spectral lines originate from the dissociation of hydrogen molecules [71]. As an example, the SiH radical is formed by electron impact of silane which yields an excited silane molecule [65]

$$e^- + SiH_4 \rightarrow SiH_4^* + e^- \qquad \text{Eq. (2.2)}$$

The excess energy in SiH_4^* is released when it is dissociated into the fragments

$$SiH_4^* \rightarrow SiH^* + H_2 + H \qquad \text{Eq. (2.3)}$$

The excited SiH^* spontaneously release its excess energy by emitting a photon at a wavelength around 414 nm, which gives the bluish color to the discharge.

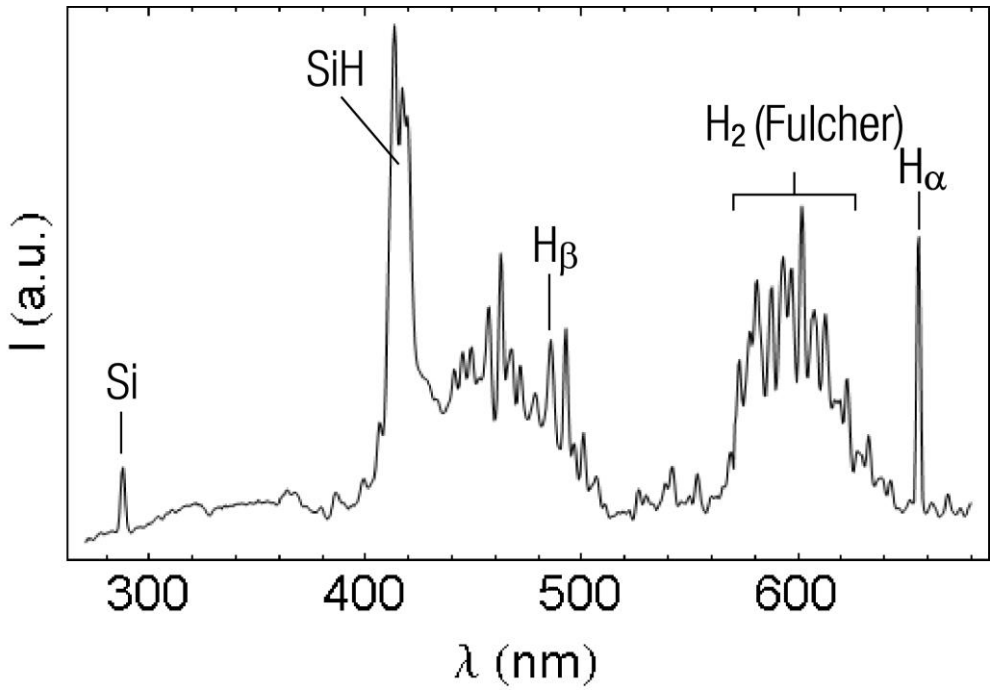

Fig. 2.3: Typical OES spectrum of a SiH_4 +H_2 plasma [17]

OES is recorded through the quartz viewport of the reactor using a fiber optic cable that guides the plasma light to a monochromator, which is coupled to a photodetector. The spectrometer Avantes MC2000 equipped with a grating was used for full spectrum measurements. Gaussians are fitted to the peaks in the emission spectrum after background subtraction.

2.2.2 VI probe

In PECVD process, the knowledge of coupled power and understanding the state of the plasma is important. The reflected power recorded by the power meter is subtracted from the forward power to estimate the power coupled to the plasma. However, the actual power coupled to the plasma can be much less, due to the loss in the cables and the matching network. This loss substantially increases with increasing plasma frequency [68]. Hence it is imperative to have a VI probe attached to the VHF power source between the matching network and the reactor to estimate the real time voltage $|V|$, current $|I|$ and the phase difference $\emptyset$ between them. The phase lag between the plasma current and the voltage, provides information whether the plasma is in a capacitive or a resistive regime [72]. The applied power is given by $P = |V| * |I| * \cos\emptyset$. In our set up, reactor 1 is fitted with a MKS VI probe between the matching network and the RF electrode (the set-up details can be found Fig. 3.3) for the electrical plasma diagnosis and to monitor the delivered power accurately.

2.3 Nanoparticle characterization

Various diagnostic techniques are available for NP characterization and each technique offers several advantages, but also comes with its limitations. Raman spectroscopy is a simple and reliable technique to get a first quick estimate of particle size and morphology. X-ray diffraction (XRD) similarly provides information on material morphology, but data acquisition is time consuming, plus it only provides information on the volume average of nanocrystals from the broadened peak. XRD is also not sensitive to individual sizes in a multimodal size distribution of particles. Using Transmission Electron Microscopy (TEM), multimodal size distribution analysis can be done, however this is challenging for a densely packed NP ensemble and, in addition, sample preparation is time consuming [73].

2.3.1 Raman spectroscopy

When light interacts with a material, most of the photons are scattered elastically by a process called Rayleigh scattering. However, a small fraction of the photons are inelastically scattered, which is utilized during Raman spectroscopy to investigate local

atomic arrangements through bond frequencies and lattice vibration (phonon) frequencies of the sample. Raman spectroscopy is an important diagnostic tool used to analyse NP morphology and size distribution.

Raman interaction leads to two possible outcomes; the sample absorbs energy (to a virtual state) and the emitted (scattered) photon has lower energy than the incident photon or the sample loses energy and the emitted photon has a higher energy than the incident photon. The scattered photon has either gained energy and thus exhibits a lower wavelength (anti-Stokes shift) or it has lost energy which leads to a higher wavelength (Stokes shift). This outcome is related to the density of states of the different phonons in the sample. The scattered light spectrum contains information about the sample's vibrational modes and thereby its composition. The different measured modes in case of silicon are given in table 2.1. This is used to detect and analyse amorphous and crystalline features of silicon NPs.

Table 2.1: Various modes for amorphous and crystalline silicon

Mode	Raman shifted peak position
Amorphous silicon transverse-acoustic (TA)	~ 150 cm^{-1}
Amorphous silicon longitudinal-acoustic (LA)	~ 330 cm^{-1}
Amorphous silicon longitudinal-optic (LO)	~ 440 cm^{-1}
Amorphous silicon transverse-optic (TO)	~ 480 cm^{-1}
Silicon nanocrystals / Grain boundaries TO	~ 510 cm^{-1}
Crystalline silicon TO	~ 520 cm^{-1}

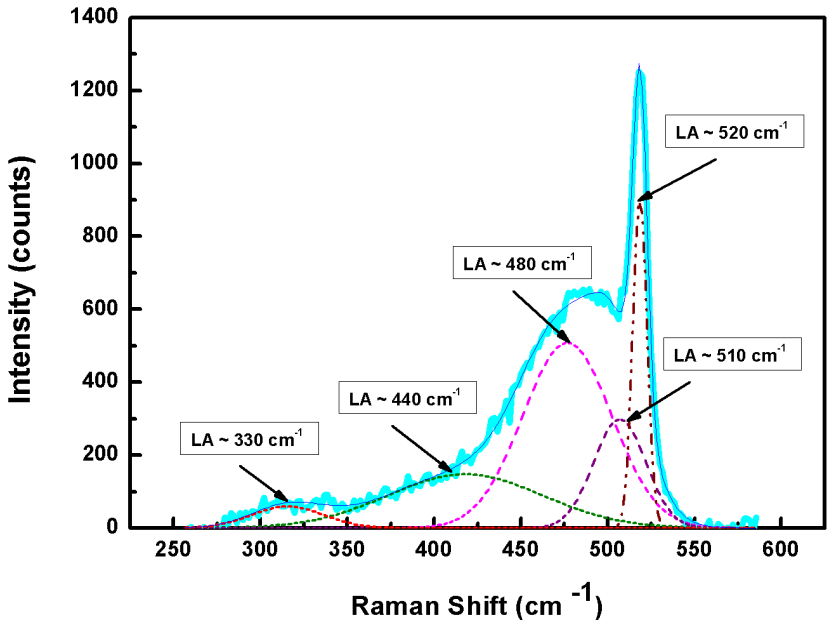

Fig. 2.4: Example of a Raman spectrum of mixed phase Si NPs deposited on Corning Eagle XG glass substrate.

Fig. 2.4 shows a Raman spectrum analyzed by fitting a number of Gaussian peaks to the raw spectrum, after subtracting the baseline, measured on mixed phase Si NPs deposited on Corning Eagle XG glass substrate. The different Gaussian fits associated with various phonon modes are also shown. The areas of these peaks are then divided, resulting in the Raman crystalline fraction, R_C [74]:

$$R_C = \frac{I_{510}+I_{520}}{I_{480}+I_{510}+I_{520}} \qquad \text{Eq. (2.4)}$$

Here, I_x denotes the Gaussian fitted peak area associated with the Raman shift at x cm^{-1}. Although R_C gives a quantitative measure for the crystalline fraction, it does not correspond to a volume fraction. It is however an extremely useful quantity to compare the crystalline fraction of different samples.

The crystalline ratio was calculated from Raman spectra obtained ex situ with an inVia Renishaw microscope equipped with an Argon laser (wavelength of 514.5 nm), a grating with 1800 lines mm^{-1} and a CCD detector to study the vibrational modes of the nanoparticles. The laser power density is fixed at 0.3 W/mm^2 and we use only 1% of the laser power to ensure we do not crystallize the sample. This was confirmed by taking three successive measurements and checking their reproducibility. To prevent heating the sample was placed slightly lower than the focus and the spot size was 50 µm.

2.3.2 Transmission electron microscopy (TEM)

TEM is an extremely sensitive characterization tool which can be used to investigate the crystallographic structure and structural defects as it provides resolution down to a few atoms. The high magnification or resolution of TEM is due to the small electron wavelength, λ_e, given by de Broglie relationship

$$\lambda_e = \frac{h}{p} = \frac{h}{m_o v} = \frac{h}{\sqrt{2qm_o V}} = \frac{1.226 \times 10^{-9}}{\sqrt{V}} \qquad \text{Eq. (2.5)}$$

where p is the momentum of the particle, m_o and q are the electron mass and charge, h is Planck's constant, v is the electron thermal velocity and V is the accelerating voltage. For instance, for an accelerating voltage of 200 keV, λ_e is 0.00274 nm.

In TEM, electrons are emitted from an electron gun and focused by electromagnetic lenses to form a beam which illuminates the sample. The electron beam interacts with the sample and is scattered or diffracted by the atoms. The emergent electron wave contains information about the potential distribution in the sample. As the electron wave transvers the sample, both the amplitude and phase can change, giving rise to image contrast. Different types of contrasts arise, such as diffraction contrast, mass contrast, and phase contrast. Coherent elastic interaction of electrons with a crystalline sample produces

diffraction contrast. HRTEM (High Resolution TEM) measurements increase the resolution of the image and allow the detection of lattice fringes providing information about the crystalline structure of the material.

To obtain lattice images, a large objective aperture is placed in the back focal plane of the objective lens so that it allows many beams to pass including the direct beam. Phase contrast is obtained by the interference of the direct beam and the diffracted beam (Fig 2.5. (a)). In the bright field (BF) mode, the aperture is placed which allows only the direct beam to pass (Fig. 2.5 (b)). So the image is formed from the weakening of the direct beam after interaction with the sample. Hence mass thickness and diffraction contrast contribute to image formation, so the thick areas, heavy atoms and crystalline regions will appear darker. In the dark field mode (DF), the direct beam is blocked and one or more of the diffracted beams is allowed to pass though the aperture (Fig. 2.5 (c)). As the diffracted beam has interacted with the sample useful information about planar defects can be extracted.

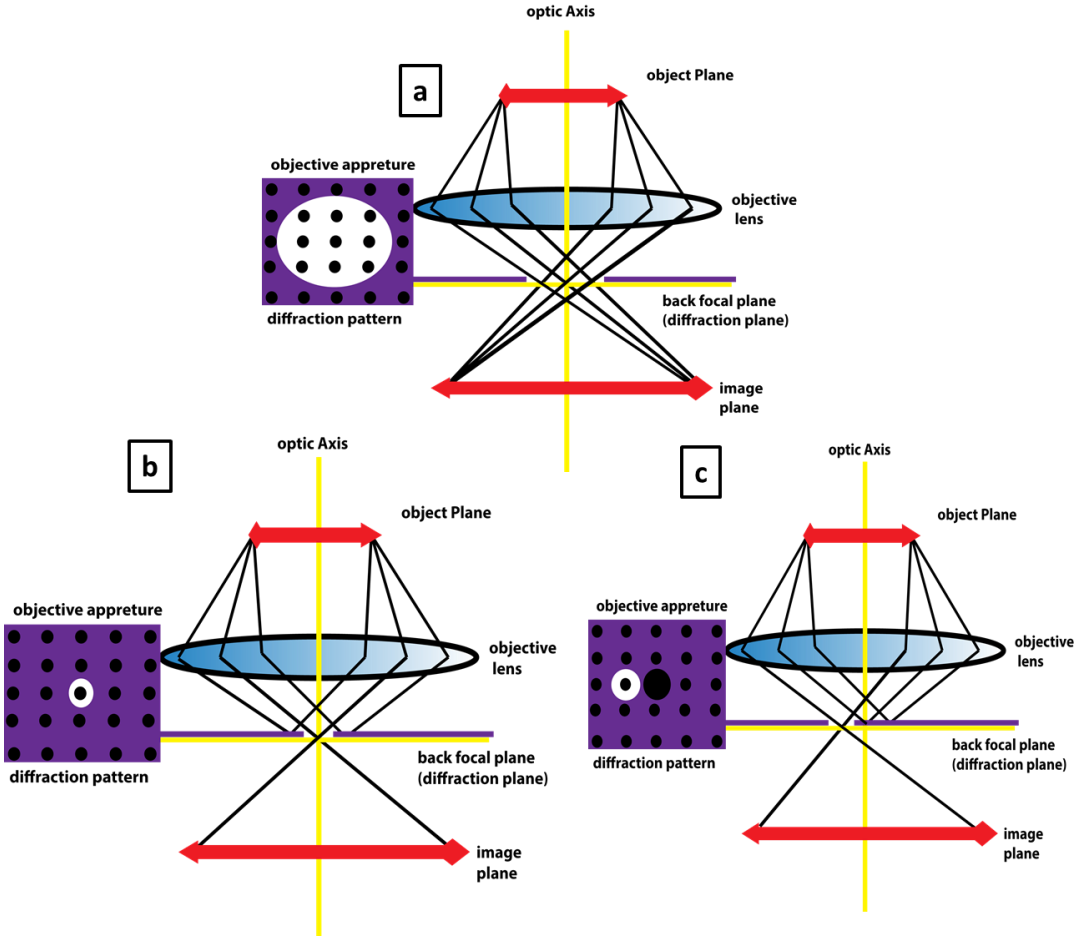

Fig. 2.5: Simplified representation of ray trace leading to first intermediate image of the objective lens in various image modes (a) HRTEM mode (b) BF mode (c) DF mode. Image adapted and modified from http://www.microscopy.ethz.ch/TEM_BF.htm

For elemental analysis, EDS (Energy dispersive X-ray spectroscopy) is used. For EDS mapping windowless 100 mm^2 SDD (silicon drift detectors) EDS detectors are used. SDD

detector converts X-rays emitted from atoms into electronic signals which are sent to pulse processor that measures the electronic signals to determine the energy of each X-ray detected which is sent to the EDS software. Imaging is done using a FEI Tecnai TF20ST/STEM with a liquid nitrogen cooled EDAX EDS detector. It relies on the interaction of X-ray and the material. As each element has its unique atomic structure, by examining this interaction it is possible to identify the particular element and its relative proportion. Atoms within the sample contain ground state electrons in discrete energy levels bound to the nucleus. A beam of electrons is focused on the sample being studied, which excites an electron in the inner shell, ejecting it from the shell, thereby creating an electron-hole in its place. An electron from a higher energy shell fills its place and to maintain the energy difference, X-ray is emitted between the two electrons' states. This energy difference is characteristic of the specimen atomic number from which it is derived.

Structural characterization of deposited particles has been done with a Tecnai 10 and a JEOL ARM 200 Transmission electron microscope operated at 200 kV. Fast Fourier Transform (FFT) analysis of HRTEM images was used to detect local crystal orientations and periodicities within the particles studied.

Inclusions of less dense material and/or material of different compositions or voids can be detected using high angular annular dark field – scanning transmission electron microscopy (HAADF-STEM) imaging. The HAADF detector uses the electrons scattered over large angles for imaging. The HAADF detector is therefore mass sensitive, which means that higher brightness in the image corresponds to the presence of (a larger concentration of) heavier atoms and vice versa.

2.3.3 X Ray diffraction (XRD)

XRD is a characterization technique to probe the arrangement of atoms within a crystal. It additionally provides information about average crystalline size and residual stress in a material. However, as the diffracted X-rays have low intensity, especially for low atomic number materials, thin film XRD requires special grazing incidence optics and information acquired over large area to maximize signal from the crystalline volume. Grazing incidence XRD (GI XRD) (Panalytical X'Pert MPD diffractometer) enables measurements on thin films as its penetration depth is only on the order of a few nm. Diffraction data is acquired by exposing powder samples to Cu-K_α X-ray radiation, which has a characteristic wavelength (λ) of 1.5418 Å. High resolution goniometer with optically encoded sample positioning enables step size of 0.0001°. At smaller angles of incidence, the beam will not penetrate (or refract) very deep into the sample and total external reflection occurs when this angle is less than the critical angle, i_c. The majority of the X-ray beam is then reflected, and the refracted beam propagates parallel to the interface.

The X-ray beam incident on a sample is diffracted by the crystallographic planes. In a typical experiment, the diffracted intensity is measured as a function of 2θ, where θ is the incident angle, which yields the diffraction pattern. This diffraction pattern is used to identify the specimen's crystalline phases and to measure its structural properties. According to the Bragg condition, the diffracted beam shows constructive interference if the following is satisfied:

$$2d\ sin\ \theta = n\lambda \qquad \text{Eq. (2.6)}$$

where λ is the X-ray wavelength and d represents the orientation dependent interatomic distance in the solid given by

$$d = \frac{a}{\sqrt{h^2+k^2+l^2}} \qquad \text{Eq. (2.7)}$$

where [hkl] represents the crystal orientation and where the lattice constant a = 0.543 nm for bulk c-Si. Bragg interference peaks at 28.4^0, 47.5^0 and 56.1^0, corresponding to the (111), (220) and (311) crystal planes, respectively, are observed for crystalline Si NPs. The grain size d_g can be estimated from the FWHM of the interference peaks $w\ (2\theta)$ at an angle (2θ) using Scherrer's formula [75]. Here κ is dimensionless shape factor, with a value close to unity, for our calculations we have used the κ = 0.9, but this value varies with the shape of the crystal.

$$d_g = \frac{\kappa\lambda}{w(2\theta)cos\theta} \qquad \text{Eq. (2.8)}$$

However it is important to note that the Scherrer formula estimates the volume average size of the size distribution.

Chapter 3: Probing periodic oscillations in silane dusty plasma*

Abstract

The effect of the growth of dust particles on plasma dynamics and vice versa is studied in this chapter. To estimate the dust formation time scale in a silane–hydrogen plasma, optical and electrical plasma diagnostics are performed. Optical studies with optical emission spectroscopy and electrical studies with plasma Voltage Current probe are done both in dusty and non-dusty plasma regimes. A periodic fluctuation in emission intensity and plasma current is observed in a dusty plasma regime. The trends of the frequency of fluctuations with varying substrate temperatures and gas flows are studied. However, no such fluctuation is observed in the non-dusty plasma. It is hypothesized that this fluctuation arises from the periodic formation and ejection of a dust cloud when a critical dust particle size is reached.

* Published as
A. Mohan, C.M. van der Wel, R.E.I. Schropp, and J.K. Rath. "Probing periodic oscillations in a silane dusty plasma in a very high-frequency plasma enhanced chemical vapor deposition process." *Can. J. Phys.* **92** 744–748 (2014)
DOI : http://dx.doi.org/10.1139/cjp-2013-0611

3.1 Dust formation in silane-hydrogen plasma

Plasma enhanced chemical vapor deposition (PECVD) is a widely used technique for thin film silicon deposition. Nanoparticle and dust formation in a silane–hydrogen discharge in PECVD can have a deleterious or beneficial effect on the deposited layer depending on the growth conditions of silicon material. In-situ laser light scattering (LLS) and spatially resolved optical emission spectroscopy (OES) measurements have shown that certain silicon plasmas produce a significant amount of in-situ particulate contamination or plasma dust [76, 77]. Plasma dusts may lead to voids and defects in the deposited layers and degrade the performance of the solar cell. In this case plasma dust has a deleterious effect on the deposited layer. With shrinking device sizes, the size of the dust particles produced during silane plasma processing can be larger than the layer thickness, embedding the layer and causing electrical shunts. Presence of dust makes the plasma non-uniform leading to non-uniform layers for large device areas. Also when the dust particles reach the pump, they result in equipment down time and loss of Si precursors which do not participate in deposition.

Incorporating silicon nanoparticles with well controlled size in photoactive amorphous layers, leading to 'polymorphous' material, on the other hand, has been shown to be beneficial: it leads to high open circuit voltage of deposited solar cells and it has been claimed to have better stability against light soaking [78]. Moreover, it has been proposed that the use of a layer of silicon quantum dots in a multi-junction solar cell would allow to surpass the Shockley–Queisser energy conversion efficiency limit [79] by trapping light from a wider solar spectrum, while reducing losses associated with non-absorption of below-band gap photons and lattice thermalization loss. Incorporating quantum dots (QDs) is a way to engineer the band gap, and theoretically the radiative efficiency limit of 42.5% and 47.5% for two-cell and three-cell tandem stacks, respectively, can be achieved, compared to 29% for a single junction Si cell according to the S-Q limit [55].Here we attempt to find precise control of plasma processes to obtain the desired particles to be embedded in the layer or removed from the gas phase depending on the choice of the material for the device.

In PECVD the source gases (SiH_4 and H_2 in our case) are dissociated by electron impact. Source gas mixture is supplied between two parallel capacitively coupled electrodes on which an oscillating electric field is applied. The free electrons (which are sometimes provided by an external source) are accelerated by the oscillating electric field and collide with the gas molecules. If the collisions are sufficiently energetic, they result in the ionization of gas molecules and create extra free electrons, which in turn collide with other gas molecules. An avalanche of reactions follows, resulting in plasma containing free electrons and (positive) ions sustaining a discharge between the electrodes. As the mass of the electrons is much lower than the mass of the ions, the electrons pick up most of the RF energy enabling them to travel very fast. They are also hardly scattered by the ions. This

leads to loss of electrons to the walls and the electrodes, leading to a positive potential in the plasma bulk. The ions and radicals which are produced in the plasma are deposited on a substrate which is mounted on one of the electrodes (usually the grounded electrode).

As the bulk plasma has a positive time averaged potential, the negatively charged clusters or neutral clusters which collide with electrons collecting net negative charges remain electrostatically trapped in the plasma volume due to the potential barrier across the sheath. If these clusters collide with one or more positive ions, they become neutral clusters and exit the plasma by diffusion. As the electron capture cross section depends on the size of the cluster [80], particles with sizes less than 2 nm are not trapped in the plasma bulk.

The model for different phases in the growth from precursors to powder in a silane-based discharge have been extensively described elsewhere [81]. The formation of plasma dust is a sequence of four steps as shown in Fig. 3.1. The nucleation phase leads to the formation of clusters of 100-1000 silicon atoms, after which there is a period of charging and growth of particles. At a certain critical size of 3-10 nm diameter and at a particle density of 10^{16}-10^{18} m^{-3}, these particles aggregate into multiple charged aggregates of 10-100 nm. Further growth proceeds by acquiring negative charge until charging effects prevent further agglomeration. Finally their growth continues by attachment of positive ions or neutrals, at a rate similar to thin film deposition, forming powder. The powder that is formed is either lost to the electrodes or walls of the reactor, or pumped out because of the laminar gas flow towards the pump, or it is trapped in between the sheaths until the plasma is turned off.

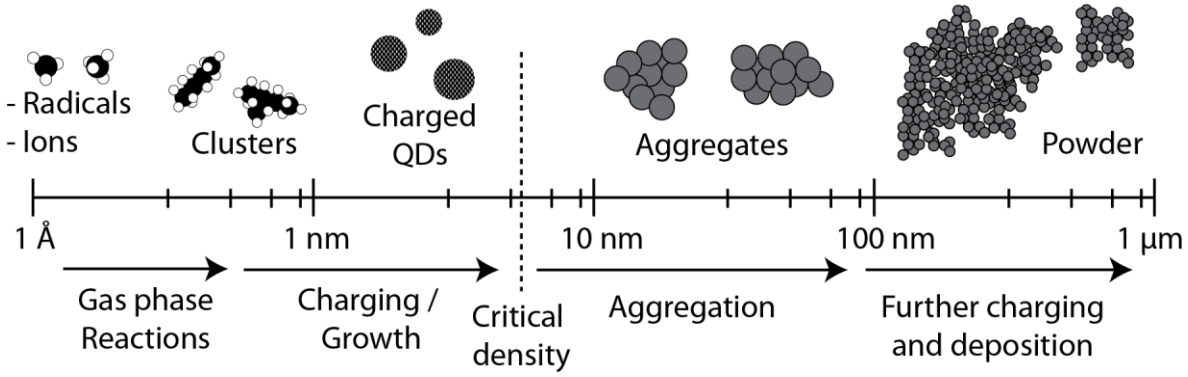

Fig. 3.1: Nucleation and growth of silane particles in a PECVD plasma; Image credit [17].

3.2 Transition from non-dusty to dusty regime

As is illustrated in Fig. 3.1, growth of clusters through polymerization reactions to a certain critical size and density, and charging, leads to the formation of multiply charged aggregates with sizes of 10–100 nm [82]. The formation of larger aggregates offers a greater

capture cross section for electrons [80]. Powders act as electron traps resulting in negatively charged particles with charges of the order of 10–3000 elemental charges (proportional to the dust radius) [81].

During the coagulation step, when the aggregate size becomes higher than a critical value (around 6 nm), their concentration decreases [83]. The clusters start to gather a steady flux of ions and electrons. After coagulation, the particles reach size of tens of nm there by greatly increasing the cross section for capturing electrons, lowering the electron density in the plasma. As the power supplied to the plasma is constant, the energy per electron increases, leading to higher electron temperature. This negative charge prevents further coalescence of the dust particles and also prevents the particles from entering the plasma sheath boundary, trapping them in the plasma bulk when the plasma is known to be in the γ' (dusty) regime. The critical phenomenon of plasma transition from the so-called α (non-dusty) to the γ' (dusty) regime [80, 83] occurs when the electron losses on the particles surface becomes higher than that on reactor walls. Consequently these properties are reflected in the optical emission which is clearly visible even by visual inspection (Fig. 3.2). The optical emission in the γ' (dusty) regime (Fig. 3.2 (b)) is clearly more pronounced as more electrons have higher energy to excite different plasma species.

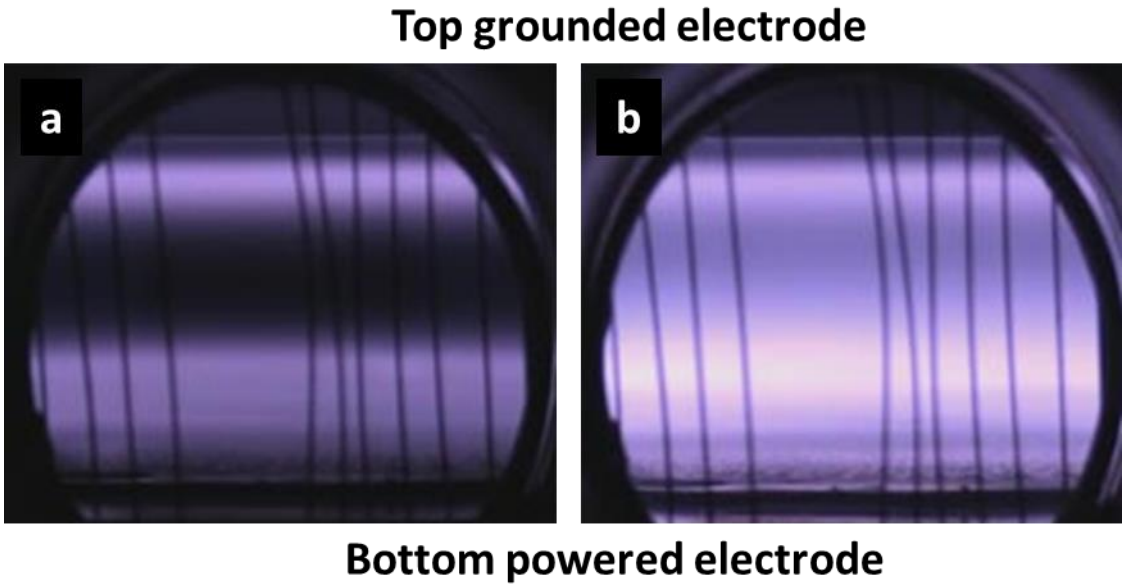

Fig. 3.2: Optical emission of silane plasma in the α regime (a) Optical emission in the γ' regime (b), visible from the view port (image taken from [84]*). The plasma parameters were hydrogen flow dilution R = 45, substrate temperature T_s = 200°C , inter electrode distance d = 27 mm. The transition from α regime to γ' regime was done by changing the applied power, P from 13 W to 16 W.*

Powder formation is a continuous process that is occurring in the plasma, so there are always clusters being generated to contribute to film growth (in non-dusty regime) or converted into powder (in dusty regime). This is determined by the residence time of the species in the bulk plasma. Agglomeration can only be reached when the particles have

enough time to reach the critical density before they are expelled from the plasma: the competition between the initial particle growth time and silane cluster residence time separates the dusty and the non-dusty regime [85]. Also the flow pattern is important: in a showerhead design, the gas flows in through a grid in one of the electrodes to allow a homogeneous laminar flow favoring and sustaining dust formation [72].

This transition to a more dissipative regime is accompanied by significant changes in plasma characteristics, such as higher bulk emission, reduction in self-bias voltage, and increase in ionization and deposition rates. A dust-free plasma can be made into a dusty one by increasing one or more of the deposition parameters, such as the applied power density, process gas pressure, or inter-electrode distance, and decreasing one or more parameters, such as the hydrogen dilution R (H_2/SiH_4) and the substrate temperature [72, 86, 87, 88, 89, 90].

Our interest in dusty plasmas originates from our goal to produce the particles of interest, a special class of semiconductors called QDs that appear at the transition from the non-dusty to dusty regime [91]. Studies on time evolution of particle density and size by Boufendi et al. [92] using transmission electron microscopy have shown that when the cluster size becomes larger than 6 nm, the transition from α to γ' regime takes place. At the onset of this transition, the density of particles drops and their radius increases by aggregation [91]. Thus, using a pulsed plasma silicon QDs (size less than 5 nm) could be generated, as shown by a few other groups [33, 93]. In chapter 5 of this thesis, we will show how to use pulsed plasmas to obtain a finer control of silicon nanoparticles.

QDs are the polymerization precursors leading to powder, and a thorough understanding of their formation and growth is the key to control dust. QDs are materials with size less than the exciton Bohr radius, spatially confining the electrons and holes. The exciton Bohr radius of silicon is 4.2 nm [94]. For radii smaller than this, quantum confinement effects come into play, rendering size dependent optoelectronic properties. Our materials of interest are silicon and silicon-germanium QDs. Thus with a judicious combination of different QDs a wide variety of materials with different band gap can be made to harvest a wider solar spectrum.

With this goal in mind, we have designed a new plasma chamber (chamber 5) to grow and extract nanoparticles in the gas phase in a single step for implementation in a solar cell (details in Chapter 4 of this thesis). This chamber is a part of the ultrahigh vacuum multi-chamber very high frequency PECVD deposition system ASTER. More technical details on ASTER can be found in Chapter 2 and [71]. But prior to this solar cell application, it is crucial to have utmost control over particle formation in the plasma to strengthen our understanding on the dynamics of dusty plasma processes, which is presented in this chapter.

3.3 Recording optical and electrical diagnostics of dusty and non-dusty plasma

The experiments described here are performed in chamber 1 of ASTER, which is equipped with a viewport for optical diagnostics and a MKS current voltage (VI) probe for electrical diagnostics as shown in Fig. 3.3. As described in chapter 2, the new chamber of ASTER (chamber 5) is designed for the single step synthesis of silicon quantum dots. Because the QDs are formed at the transition of the non-dusty plasma to the dusty phase, a thorough understanding of the behavior of these plasmas is necessary. We probe the plasma with non-invasive techniques: optically with in situ optical emission spectroscopy (OES) and electrically with a built-in VI probe (details provided in experimental section in Chapter 2).

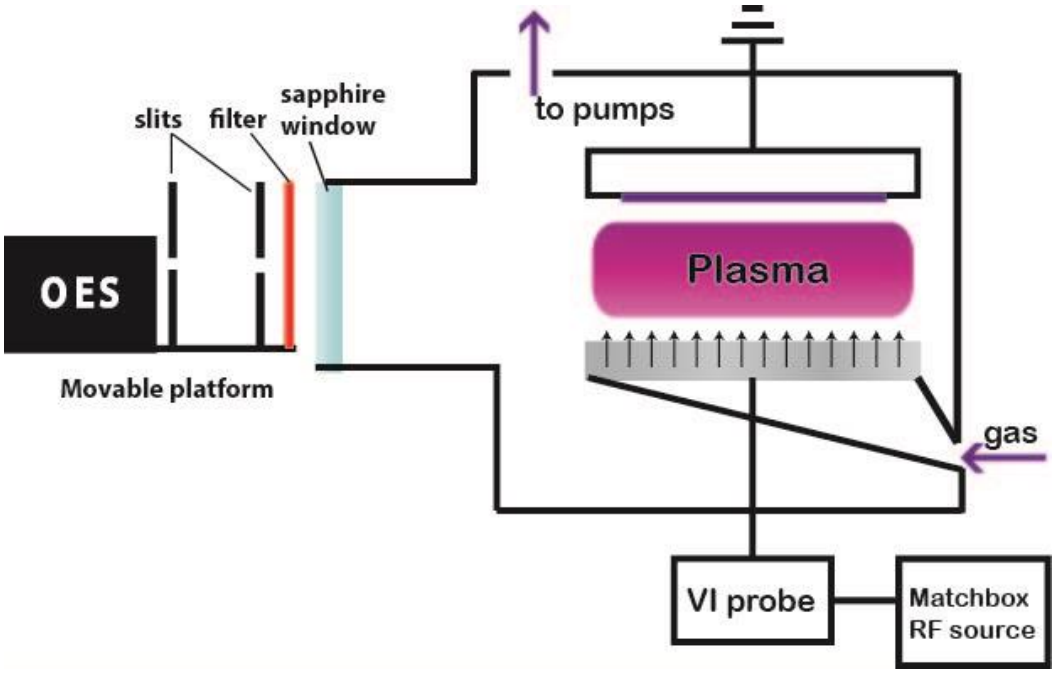

Fig. 3.3: In situ experimental setup for optical and electrical diagnostics of dusty and non-dusty plasma regime in chamber 1 of ASTER.

The emission of photons from the large number of excited species in the plasma leads to characteristic lines in the emission spectrum monitored with OES. The agglomeration of dust particles leads to a transition from the α to γ' regime where the particles have a higher electron capture cross section, in turn decreasing the electron density and increasing the electron temperature. These properties are reflected in the enhanced emission of the plasma as a larger fraction of electrons have higher energy to excite different plasma species, hence having a broader emission profile and higher bulk emission [84, 95].

Light emission experiments were done with Hamamatsu H5783-04 photomultiplier tube (PMT) as detector. The PMT opening was provided with appropriate interference filters for the desired wavelengths of specific lines (SiH*, Balmer H_α, and Balmer H_β at 413.8, 656, and 486 nm respectively). For a few cases, an optical emission spectrometer Avantes Avaspec-2048-USB2, equipped with a grating, was used to record axial emission profiles

from the plasma for full spectrum measurements. In this case, the light from the plasma chamber was focused on an optical fiber which led the light into the spectrometer. This system is mounted on a stage that can be moved in the vertical direction, perpendicular to the plane of the electrode. The optical emission data with the interference filters matched well with the spectrometer data for the above mentioned wavelengths of interest.

For the electrical measurements of the plasma, the electrode potential (V), plasma current (I), and their relative phase (ϕ) were measured directly using an MKS VI probe attached between the matchbox and the powered electrode. The plasma impedance (Z = V/I) and delivered power (P = VI cos ϕ) can also be calculated.

Optical and electrical measurements were performed in both non-dusty and dusty regimes in very high frequency PECVD process by altering the plasma parameters according to the regime we desired as given in Table 3.1. The non-dusty regime is our standard deposition condition for device quality a-Si:H. Decreasing the inter-electrode distance from 27 to 10 mm will decrease the probability of dust formation, but in our case, the combination of increasing power and pressure at small inter-electrode distance counteracts this effect and the plasma is in the dusty regime. The transition from the non-dusty to the dusty regime was observed by a change in emission profile and higher bulk emission (observed both with OES and visually through the viewport of the chamber) and also by the shift in plasma impedance Z towards a more resistive plasma. More details on dusty plasma and OES can be found in ref. [95]. For each measurement the plasma was switched on, left to stabilize for 60 s, before doing the optical and electrical measurements for 100 s.

Regime	Freq-uency (MHz)	Power (W)	Pressure (mbar)	Substrate temp. (° C)	SiH_4 : H_2 flow (sccm)	Electrode distance (mm)
Dusty Plasma	60	17.5	3	180	5:100	10
Non-Dusty Plasma	60	5	0.16	180	35:175	27

Table 3.1: Plasma parameters used for OES and V-I measurements for dusty and non-dusty regime.

3.4 Results and discussions

3.4.1 Optical and electrical measurements

The presence of a large number of excited species in the plasma produces significant emission. The plasma emission intensity gives information about concentrations of certain radicals in the plasma, the electron temperature, relative changes in emission spectrum and knowledge of which regime the plasma is in. In a silane-hydrogen plasma for instance, Si* emission intensity can be correlated to deposition rate [96] and the electron temperature

can be determined from the ratio of H_α/H_β [97]. Dust particles have a direct influence on plasma properties and hence, also the emission observed in the plasma shows clear changes.

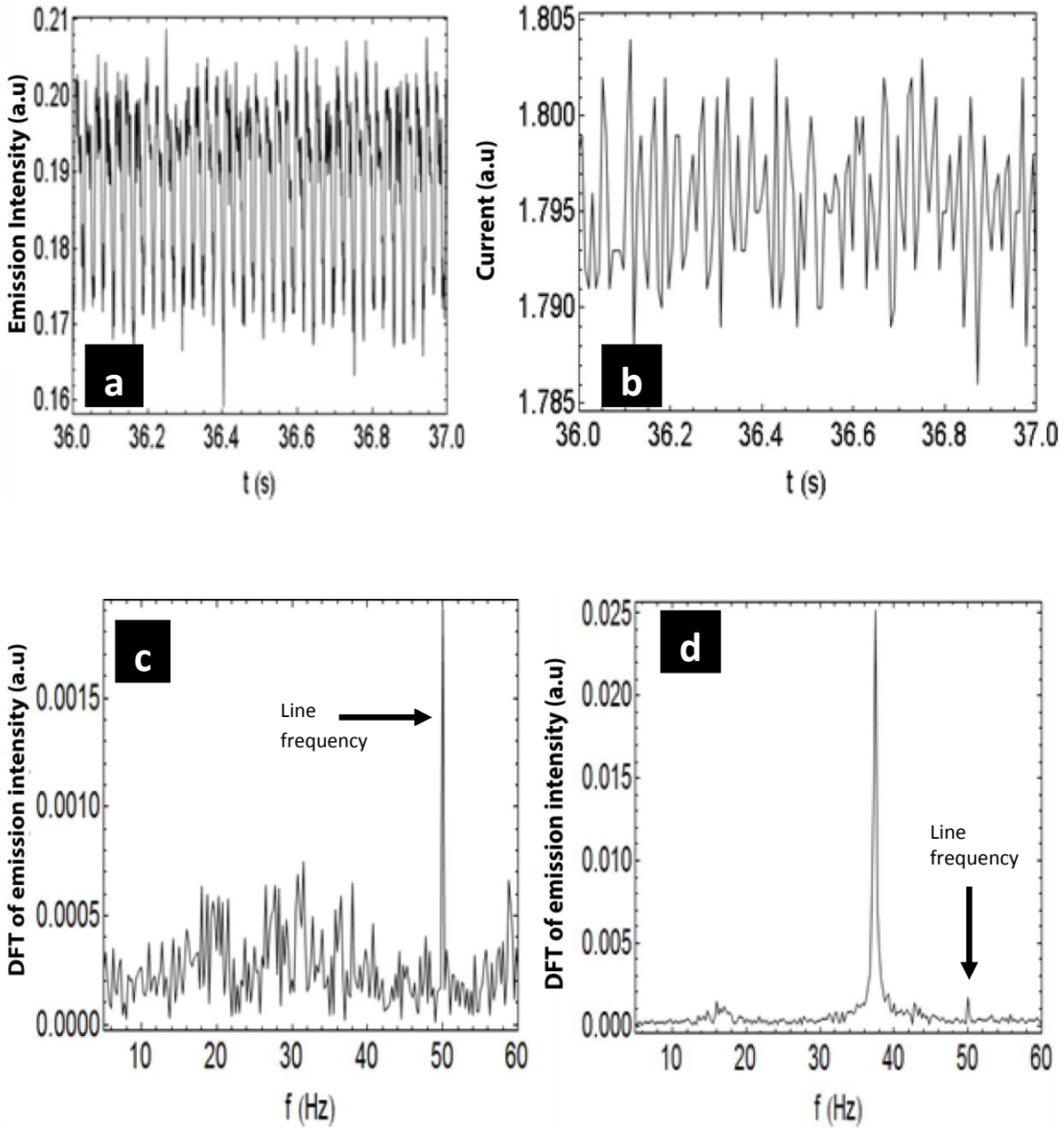

Fig. 3.4: (a) Emission intensity of SiH in the dusty regime. (b) Current through the plasma in the dusty regime. (c) DFT of emission intensity of SiH* signal in the non-dusty regime. (d) DFT of SiH* emission intensity in the dusty regime. Plasma parameters for non-dusty and dusty regimes are given in Table 3.1.*

The optical emission lines of SiH*, Balmer H_α and H_β at 413.8, 656, and 486 nm, respectively, were recorded by using appropriate filters and the photomultiplier tube, and the plasma current was measured using the VI-probe, both for the non-dusty and the dusty regimes, as described in the experimental section. The output parameters of both optical and electrical measurements probed with OES and VI probe, respectively, showed a

patterned periodic oscillation in the dusty regime. However, for the same measurements performed in the non-dusty regime, there was no fluctuation in either optical or electrical measurements, but a weak signal fluctuating at 50 Hz was identified (as will be clear from the Fourier transform spectra), in all measurements, which is the line frequency. No fluctuation of the ratio H_α/H_β, which is related to the electron temperature [70] could be detected with OES in both regimes. This could be masked by the low signal to noise ratio for the required acquisition times. Some examples of the fluctuation are displayed in Fig. 3.4 (a to d). In order to quantify these oscillations, the data were then subjected to discrete Fourier transform (DFT). More detailed analysis can be found in [17].

Each measurement series in a particular plasma condition (given in Table 3.1) and emission wavelength has two sets of data series: emission intensity series (Fig 3.4 (a)) and current intensity series (Fig 3.4 (b)). In both the series, the plasma was left to stabilize for 60s after plasma ignition and then a measurement lasting 100s was taken. This measurement was divided in to 4 blocks of 25 seconds each. Each block was subjected to a discrete Fourier transform.

As the VI probe has a sampling frequency of approximately 133 Hz, the current DFT has a Nyquist frequency of 67 Hz. Frequencies above this limit are displayed as mirror images of the below frequency. So the DFTs were cropped to a range of 5-60 Hz, and Lorentzian fitting was done to the peaks after averaging over the stable plasma period. The resulting peak positions from emission and current are combined in Fig. 3.5. Here it should be noted that the synchronously recorded DFTs in both plasma current and emission overlapped each other perfectly at 38 Hz, which is the dominant fluctuation frequency although other frequencies with weak signal in the range 10-50 Hz were observed.

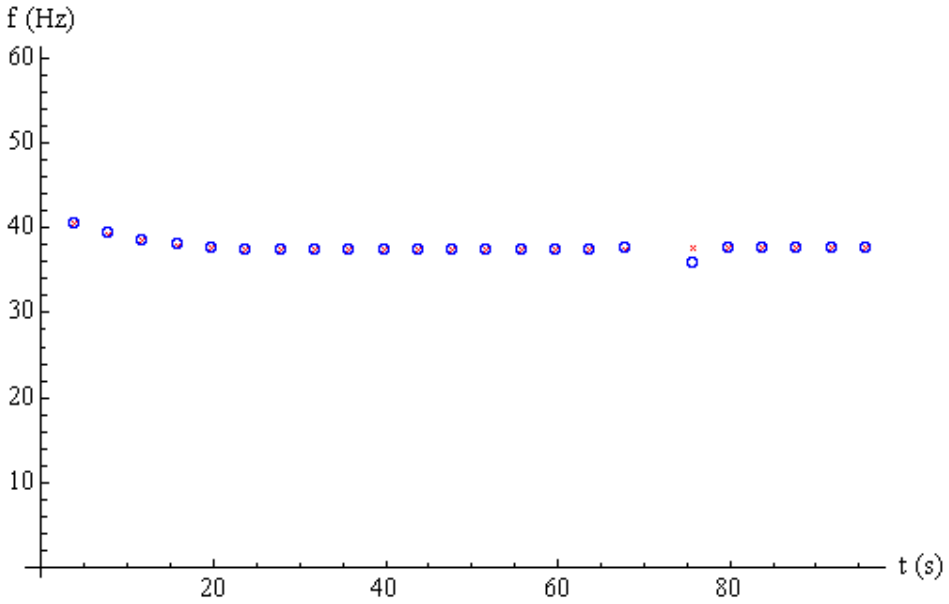

Fig. 3.5: Combined peaks from emission of SiH line (crosses) and plasma current (circles) frequencies, for the plasma in the dusty condition.*

3.4.2 Effect of substrate temperature and gas flow on the fluctuation frequency

The fluctuation frequencies of both SiH* and H_α lines in the dusty regime showed similar trends with overlap of emission and current frequencies at 38 Hz. For a deeper understanding of these periodic fluctuations, variation of frequencies of H_α at different substrate temperatures and total gas flows are studied. As it can be seen in Fig. 3.6 (a) and (b), an increase in substrate temperature was observed to have an inverse effect on fluctuation frequency, whereas increasing the total gas flow has the opposite effect.

The effect of substrate temperature and gas flow rate on the dusty plasma is complex. For our reactor it has been shown that a substrate temperature of 50°C, 157°C and 280°C results in an average gas temperature of 34°C, 54°C and 78°C respectively for a flow of 50 sccm [71]. These values were calculated without plasma between the electrodes and no applied RF power. These average values are an underestimation of the actual temperatures between the electrodes because of the small heat capacity of the gas in the reactor.

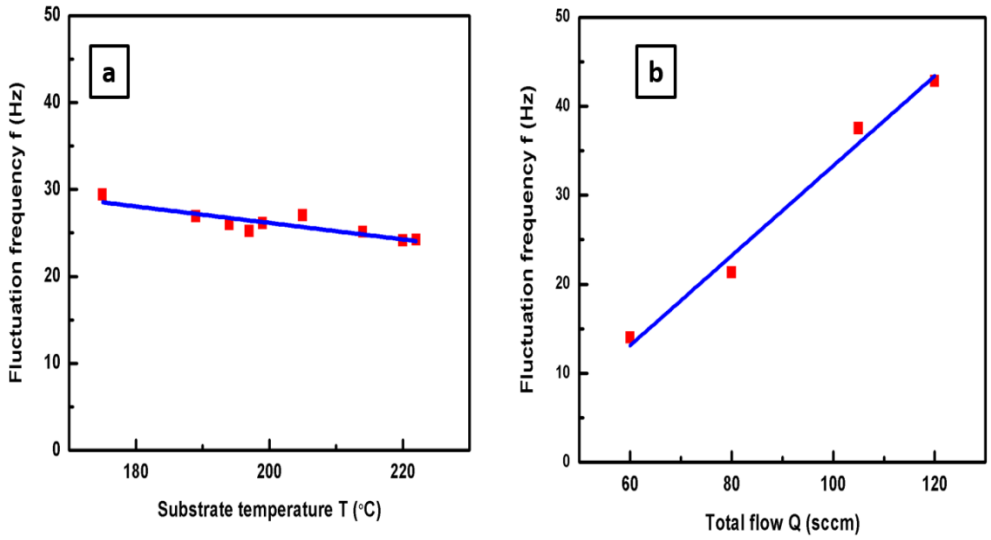

Fig. 3.6 (a): Linear fitting of fluctuation frequency f (for the H_α emission) versus substrate temperature at constant gas (SiH_4 + H_2) flow of 105 sccm (b) Linear fitting of fluctuation frequency f (for the H_α emission) versus total gas (SiH_4 + H_2) flow at constant substrate temperature of 180 °C (line is guide to the eye).

The dynamics of dust in the plasma are governed by forces at play on the dust particles. There are several forces acting on the dust particle (exhaustive review of which can be found in [81, 98]); the most relevant here are the ion drag force and the neutral drag force. Ion drag force results from the momentum exchange between positive ions and the dust particle. Since the ion flux in a discharge is directed from the center towards the sheaths the force tries to push the particles away from that central region towards the

electrodes. The ion drag force is composed of two components: the collections force and the orbit force. The collections force results from direct collisions between ions and dust particles. The orbit force results from the momentum exchange during the electrostatic interaction between a dust particle and a positive ion that is passing the particle. Similar to the ion collection force the neutral drag force results from the momentum exchange between neutral atoms or molecules and the dust particle [98]. The neutral drag force is proportional to particle cross section (πr^2), the directed flux of gas atoms or molecules hitting the dust particle ($n_g v_g$) and the momentum transfer per collision ($m_g v_{th}$). Here r is the radius of the particle, n_g is the gas density, v_g is the gas velocity, m_g here is the mass of a neutral atom/particle and v_{th} is the thermal gas velocity. As $n_g v_g$ is proportional to gas flow rate Q, neutral drag force scales as $r^2 Q$ [99].

Various reports have shown that a higher substrate temperature can suppress dust formation [80, 82, 91, 71, 100]. These references highlight the following points, the largest temperature dependence on polymerization reactions is found in the initial polymerization reactions. The rate of these reactions is enhanced by vibrational excitation of the silane molecules in the plasma. However, according to Landau-Teller theory [101], the relaxation of these vibrational excitations at the walls and in the plasma bulk, depend exponentially on the gas temperature. So, at higher gas temperatures, the vibrational excitation of silane molecules is reduced, and makes all the reactions of cluster growth much longer. Therefore, in plasmas with a higher gas temperature, caused by higher substrate temperature, the critical cluster size and concentration for coagulation is reached slower. A higher gas temperature reduces polymerization rate of silyl ions into larger polysilanes. Also lower gas density at higher gas temperature leads to slower growth of particles.

Another study using mass spectrometry in a reactor replica to the present study, has shown a decrease in count rate for higher mass ions with increasing temperature, confirming a negative influence of the gas temperature on cluster formation [102]. This confirms the hypothesis that a higher substrate temperature suppresses polymerization reactions of silyl into larger polysilanes. Hence with increasing gas temperatures, the formation of clusters slows down, consequently so does the frequency of fluctuation.

An increase of flow rate results in lower gas residence time, lower silane depletion and a higher deposition rate. The higher deposition rate is due to the availability of more precursors at higher gas flow. The lower silane depletion is due to the limited electron-SiH_4 dissociation rates due to short residence times or low electron-molecule collision frequencies, resulting in reduced silane consumption and depletion [103]. The continuous admission and evacuation of the neutral source gases, creates a neutral drag force which increases with increasing flow. Moreover an increasing flow rate has a pronounced effect on the dust growth rate and thus the frequency of oscillation increases.

In literature, similar fluctuations have been observed in dusty plasmas, each with different periods of fluctuation, depending on the plasma parameters and the type of

particles in the plasma. Different diagnostic tools, such as high resolution imaging, laser light scattering (LLS), and microwave cavity, have been used to study the formation and evolution of dust and its effect on the fluctuation [72, 99, 104, 105]. However, most of the research is based on SiH_4:Ar plasma, and only a limited study on fluctuations has been done on SiH_4:H_2 plasma [106].

In ref [72], the laser light scattering intensity was shown to have reproducible periodic fluctuations depending on partial pressure, gas temperature and rf voltage conditions in a continuous SiH_4 plasma. Also the presence of dust was shown to have an influence on the electrical characteristics of the discharge. Electron density fluctuations in a dusty SiH_4:Ar plasma was observed in ref. [99], using microwave resonance technique. The electrodes of the capacitively coupled reactor simultaneously serve as a microwave cavity, to determine electron density in the plasma. A low power probing microwave is coupled into the cavity by means of an antenna and the resonance frequency is determined by tuning the microwave frequency to maximum transmission. In the paper they determined the dependencies of this oscillation period on external plasma parameters such as flow rate, pressure, rf power, and gas composition. This fluctuation was explained as competition between dust trapping electrostatic force and dust expelling neutral drag force. As electrostatic force scales with R, and the neutral drag force scales with R^2, after a certain particle size, the neutral drag force becomes the dominant one which initiates expulsion and the particles are pushed away creating conditions for the nucleation of fresh dust particles.

In ref. [106] the intrinsic μc-Si:H layers are deposited in a dusty and powder free regime by altering the process conditions. In-situ plasma dynamics were monitored by LLS and infrared laser-based silane sensor (ILSS) was used to monitor silane dissociation efficiency. The time emission of Fulcher series was measured by OES and it was found that, during a powder-free non-dusty regime no fluctuation was observed although for the dusty regime a strong oscillation related to the cycle of dust production and ejection was observed. Further they have demonstrated that initial stages of powder formation has a beneficial effect on the efficiency of the grown μc-Si:H devices.

Based on our observation and the observations supplemented in literature, it can be hypothesized that the fluctuations arise from periodic formation and ejection of a dust cloud from the plasma bulk when a critical dust size is reached. The experimental results shown in Fig. 3.6 (a) and (b) supports such a hypothesis; the frequency of fluctuation increased with silane flow rate, which may be attributed to faster growth of dust with increased precursor flux, whereas it decreased with increase in substrate temperature, which may be attributed to slower polymerization reaction in the gas phase [102].

We also tried to measure the LLS intensity with the Hamamatsu H5783-04 PMT diode. Again at both angles (0^o and 90^o), no scattered signal could be detected from the dust particles. The inability to experimentally detect dust particles does not necessarily imply their inexistence. Rayleigh scattering occurs when the radius of the particles is much smaller

than the wavelength of incident light, which is the case for silicon nanoparticles, expected to be detected in our case. Then the Rayleigh scattering intensity of the particle of radius *R*, for the wavelength of the incident light λ, at a distance *r* from the plasma is given by

$$I_{scat}(\Theta) = I_0 \frac{8R^6}{\lambda^4 r^2} \left| \frac{m^2 - 1}{m^2 + 1} \right|^2 (1 + cos^2\Theta)$$

Here m is the ratio of indices of refraction of $\eta_{dust}/\eta_{medium}$ and Θ is the angle between the source and the detector.

As it can be seen in the equation, the Rayleigh scattering intensity is proportional to the sixth power of particles radius. Also as it's difficult to deduct the stray light from reflections of the chamber and to avoid saturation of the detector, the experiments as in our case is usually done at 90°. Then, as it can be seen in the equation, the scattered intensity is a factor of 2 lower compared to experiments done at 0°. For nanometer sized silicon particles, the scattered intensity is extremely low making their detection more challenging as is demonstrated in Fig. 3.7 [17]. For the calculations, the value of m used is 4.5 and the detector is placed at a distance of 15 cm for 633 nm laser, which is a very close approximation to our case.

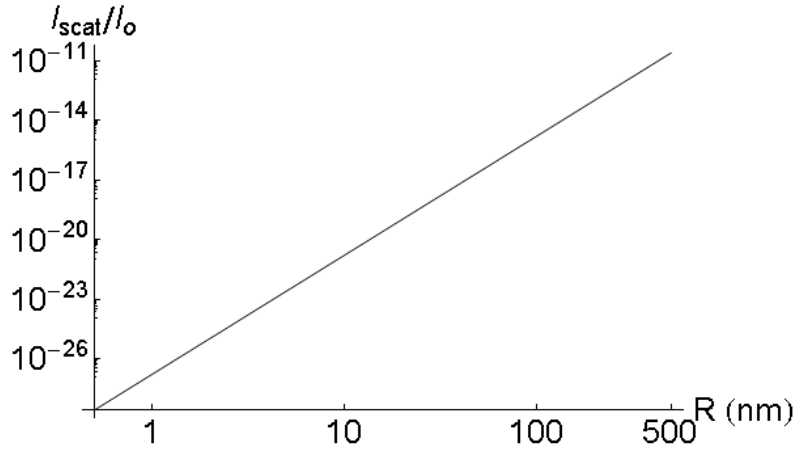

Fig. 3.7: Theoretical calculation of Rayleigh scattering intensity at 633 nm.

3.5 Relation with Chapter 5

The motivation behind investigating the oscillations found in the optical emission intensity and plasma current intensity was to get an estimate of dust formation time scales. This provides a suitable parameter space for use in pulsing plasmas to obtain precise particle sizes (Extensive work done on pulsing plasmas is reported in Chapter 5 of the thesis). As can be seen in the Fig. 3.8, the black lines represent the fluctuations found in the plasma. We

intend to use pulsing times (red lines in Fig. 3.8), smaller than the plasma oscillations, so we can stop the growth of dust and obtain quantum sized particles.

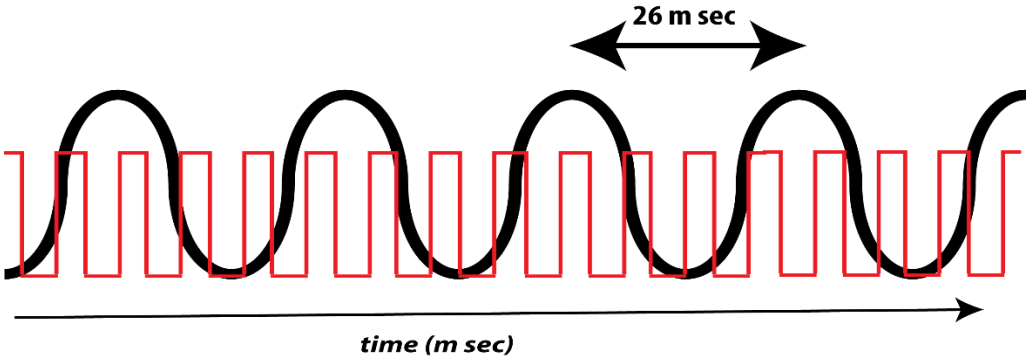

Fig. 3.8: Schematic representation of frequency observed in emission and current (black line) and intended pulsing frequency (red line) of the VHF power.

We report a detailed investigation of using different pulsing ON times and OFF times in Chapter 5, and their influence on the size of particles obtained. However the absolute value of the frequency we observe here (in chamber 1) is actually different from the pulsing frequency we use in the nanoparticle chamber (chamber 5). This is because the geometry of both the reaction chambers, the position of the pump, and the substrate holder for the collection of particles are different in the two chambers, which are also the parameter space that influence the growth of particles, hence, the frequency. A direct correlation between the two frequencies in the two chambers is not accurately possible, but the physical mechanism is the same.

3.6 Conclusions

We studied the plasma fluctuation in a dusty regime of a silane–hydrogen gas mixture in a very high frequency PECVD process. Our study aims at establishing a method to precisely control the particle size in a dusty plasma, by pulsing the plasma at time scales shorter than the fluctuations that we observe. In this way, we can interrupt the particle growth before the critical size is reached and extract them to be implemented in a quantum dot solar cell.

Periodic fluctuations observed in the dusty regime manifest themselves in the overall plasma emission intensity as well as in their electrical behavior. Increased temperatures reduced the pulsing frequency; however, increasing the gas flow increased the pulsing frequency. No such fluctuation in the non-dusty regime could be detected. It can be hypothesized that these fluctuations arise from periodic formation and ejection of dust clouds in the plasma bulk when a critical dust size is reached

Chapter 4: Gas phase synthesis of two ensembles of silicon nanoparticles†

Abstract

The design and operation of a dedicated custom designed nanoparticle reactor to synthesize silicon (Si) nanoparticles is studied in this chapter. Si nanoparticles are synthesized in the gas phase in a single step in the plasma reactor. The synthesized Si nanoparticles belong to two different phases exhibiting different structural and optical properties. Particles produced in the bulk of the plasma are aggregates of cauliflower shaped crystalline particles. Particles produced in the locally enhanced plasma regions at holes present in the grounded electrode contains a mixture of free-standing quantum sized crystalline (mean size of 2.95 nm) and amorphous particles (mean size of 15 nm). We provide insight on different plasma processes leading to the formation of aggregates and free-standing particles. We hypothesize that the free standing particles are formed due to the excess energetic electrons present in locally enhanced plasma regions.

† Published as
A. Mohan, M.M. de Jong, I. Poulios, R.E.I. Schropp and J.K. Rath. Gas phase synthesis of two ensembles of silicon nanoparticles *J. Phys. D: Appl. Phys.* **48** 375201 (2015).
DOI: 10.1088/0022-3727/48/37/375201

4.1 Plasma production of silicon nanocrystals

Plasma processes have versatile applications spanning aerospace, biomedical, automotive, and waste management industry [64]. Plasma processes, particularly capacitively coupled radio-frequency glow discharges capable of uniform depositions on large substrates, are crucial for manufacturing large area micro-electronics devices. Amorphous silicon thin films grown in such discharges are at the core of a large number of devices such as solar cells, thin film transistors (displays), and particle detectors. A very important technique for material processing such as thin film deposition, nanostructure fabrication, and surface etching and modification by employing a plasma is the plasma enhanced chemical vapor deposition (PECVD) technique.

The growth, formation, and extraction of silicon nanoparticles (NP) in silane plasmas is well established. The production of silicon NPs for instance in capacitively coupled discharges and expanding thermal plasmas can easily be scaled up to large areas and to high throughput for industrial purposes [24, 107]. Silicon nanoparticles produced by remote PECVD by S. Oda's group have been successfully applied to nanoelectronic devices [108]. The potential technological applications of Si nanocrystals encompass optoelectronics devices including silicon-based light emitting diodes [109], nanoelectronics devices such as single electron transistors [45, 46], lithium-ion batteries [52], and photovoltaic devices [54]. Owing to their low toxicity, silicon nanoparticles are also making their place in biological systems requiring a fluorescent agent [57]. More details of the above listed potential applications of silicon NPs are described in chapter 1. Besides being commercially viable for novel applications, the promising approaches for establishing quantum confinement effects observed at nanometric dimensions of silicon make them scientifically stimulating.

The ease of integration into a nanoscale device [45, 46], processing even at room temperatures and the ability to apply a variety of surface functionalizations and passivation of silicon nanocrystals [39, 41] sets apart the synthesis of nanocrystals in plasma reactors from other gas phase processes such as laser pyrolysis. L. Mangolini et al. have synthesized nanoparticles by plasma process in the gas phase and further passivated them with various organic ligands through a process called hydrosilylation [39]. Surface passivation by liquid phase has long reaction times and the additional step of transferring the nanocrystals into different surface treatment reactors after synthesis. This disadvantage is overcome by gas phase surface functionalization by plasma assisted in-flight grafting of organic molecules in an adjacent reactor as demonstrated by the same group [41]. Recently, high yield techniques of gas phase synthesis of luminescent nanocrystals in a low pressure non-thermal plasma, which has a process yield of 14-52 mg/hour [34], in an expanding thermal plasma, which has a yield of 600 mg/hour [24] and in microwave plasma with production rate of 0.1-10 gram/hour [110] have been reported.

Let's focus our attention on silicon NPs produced in high frequency capacitively coupled PECVD discharges by various groups. M. Shiratani et al. have successfully demonstrated the gas phase synthesis of Si NPs [32]. They have used replicas of multi-hole plates for RF and grounded electrodes, separated by only 2 mm from each other and restricting the gas flow to one dimension. The nanoparticles are apparently produced in the holes where the plasma is sustained, which are then transported to the substrate in the downstream. In their study, pulsed plasma is the key to produce the desired nanoparticles size. The obtained Si QD films show promising features for solar cell applications with dark and photo conductivities in the range of 10^{-11}-10^{-9} S/cm and 10^{-5}-10^{-4} S/cm, respectively. T. Ifuku et al. used a modified molecular beam epitaxy set up using a plasma cell to create a remote plasma in a very high frequency capacitively coupled discharge and the silicon nanocrystals were extracted from the cell into a diffusion chamber through an orifice when the desired particle size was reached [45, 93]. Pulsing the hydrogen gas flow in a silane plasma was key to produce monodisperse nanoparticles in this process. N. Chaabane et al. have used a standard capacitively coupled reactor to produce particles in the plasma and the particles are collected by a liquid N_2 cooled substrate on a third electrode with a floating potential, placed at the side wall [111]. The particles can be switched from 100% amorphous to 100% nanocrystalline by changing the voltage bias to the substrate. This is attributed to the large contribution of positively charged nanocrystals (which could either originate from the plasma or acquire their positive charge when crossing the sheath) to film deposition and structure. Kortshagen's group has produced nanocrystals in both a PECVD reactor [112] and in a system with two spatially distinct zones (diffuse plasma for growth of particles and constricted plasma for particle annealing/crystallization) resulting in the formation of cubic nanocrystals for nanoelectronic devices [113].

Particle formation in a silane-hydrogen discharge is a multi-step process involving nucleation, agglomeration, and growth by deposition on the surface of independent particles, similar to thin film deposition; in depth details of which are presented in ref [81]. Charging and growth of clusters to a certain critical size and density leads to the formation of multiply charged aggregates. Cauliflower-shaped agglomerates, which are composed of very small crystalline subsystems (2 nm), are found to occur at time scales of 5 to 30 seconds. A thorough microscopic study on the formation and growth of cauliflower shaped clusters is provided in Chapter 5. These "subsystems" formed at very short timescales are expected to play a significant role in dust formation [114]. For a long duration (> 30 s) plasma, which is basically a continuous plasma (like the one reported here), occurrence of several well defined particle sizes, correlating to separate particle generation modes, has been reported [83].

4.2 Silicon nanoparticle synthesis in dedicated plasma reactor

The silicon nanoparticles reported in this thesis are synthesized in a dedicated nanoparticle reactor. This reactor is a recent addition to the existing reactors in a multi-chamber VHF PECVD system ASTER (Amorphous Silicon Thin Film Experimental Reactor) (more details found in [71] and chapter 2). In this section we report the construction and operation of the dedicated VHF PECVD plasma reactor to grow silicon NPs in a single step.

The main advantage of our nanoparticle reactor design is that it is well adapted to standard capacitively coupled plasma reactors. Our reactor design is a triode system, in which the RF electrode and the electrode with the substrate holder are similar to that of the other reactors of the ASTER multichamber system, thus, allowing the handling of the substrate and gas feeding similar to other chambers and making it possible to fabricate devices. The specialty of this nanoparticle reactor is that the grounded grid electrode, placed between the RF electrode and the substrate electrode, controls and confines the plasma. The bulk plasma creation of nanoparticles can be tuned by a wide range of parameters such as inter-electrode distance, *d*, *p.d* product, pulsing of applied power, etc., independent of the substrate (as the substrate is not located in the plasma zone). The substrate, mounted to the grounded electrode, can be biased (floating potential) and even cooled (by liquid N_2), to vary the particles collection. Moreover, as this reactor is part of a multi-chamber PECVD reactor, a complete silicon quantum dot solar cell can be realized.

Another specialty of this reactor is that it has multiple viewports through which various optical diagnostics can be done in-situ in the chamber. To monitor the thickness and growth rate of the growing film in-situ the ports are available to do spectroscopic ellipsometry in the chamber. A monochromatic light source can be placed at one of the ports and the analyzer and photomultiplier tube can be placed in the opposite port for the measurements. By measuring the change in polarization of the outgoing light information about the dielectric particle properties of the deposited film can be extracted. There is also a possibility to perform laser light scattering (LLS) experiments, with the available view ports (at 0°, 6°, and 90°) to give us supplementary information on particle concentration. However, as mentioned in chapter 3, the Rayleigh scattering intensity is proportional to the sixth power of the radius of the particles. The concentration of dust produced in our case was insufficient to obtain sufficient intensity of scattered light at the output port, under all angles. In the future, there is a potential to improve the sensitivity of the diagnostic setup to gather this additional information.

As illustrated in Fig. 4.1, this NP reactor has two parallel electrodes between which the source gases SiH_4 and H_2 are dissociated by applying an oscillating radio-frequency electric field. The bottom showerhead electrode in addition to being the powered electrode also ensures homogenous and laminar flow of the source gases. A VHF frequency of 60 MHz was used for all depositions. The impedance of the plasma reactor can be matched to the

power input system through a set of adjustable capacitors in a matchbox. The free electrons accelerated by the electric field collide with gas molecules, creating additional free electrons. Each ionization process creates an extra free electron, which rapidly increases the density of free electrons and ions. The radicals and ionic species formation leads to an avalanche of reactions which creates “protoparticles” [115], subsequent clustering of which results in well-defined nanoparticles. These nanoparticles leave the plasma through the holes of the top grounded grid electrode and reach the substrate that is clamped at the top of the reactor. The substrate is maintained at temperatures lower than the gas temperature, which facilitates a thermophoretic effect [116]. Also the pump port located above the substrate aids in the collection of the particles upstream by drag force, against the gravity effect on the particles.

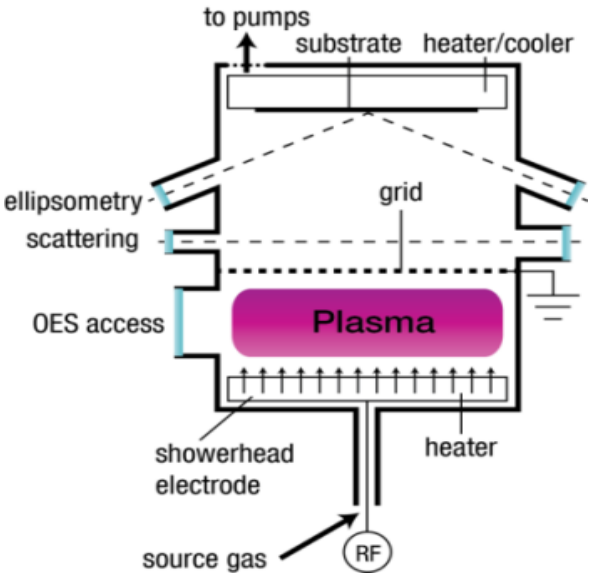

Fig. 4.1: Schematic design of the nanoparticle reactor.

For the production of the particles mentioned in this chapter, a flow of 2 sccm of SiH_4 and 25 sccm of H_2 at a reactor pressure of 0.8 mbar was used. A power of 70 W was applied to the bottom electrode. The amount of reflected power was minimized to less than 5% of the input power. No external heating was applied to the substrate kept at room temperature, unless it is cooled for improving particle collection. A picture of the top grid electrode, which serves as the grounded electrode through which the particles escape the plasma to reach the substrate, is shown in Fig. 4.2 (a). The grid grounded electrode has 240 (through)-holes with a diameter of 5 mm and 2 mm depth, all through the thickness of the electrode plate. These holes are squarely distributed as shown in Fig. 4.2 (a). The distance between the bottom powered electrode and the grounded grid top electrode is 1 cm and this gap can be changed with spacers. The substrate was kept at a distance of 6 cm from the grid grounded electrode. The radius of the electrode is 10 cm and the total radius of the reactor is 16 cm.

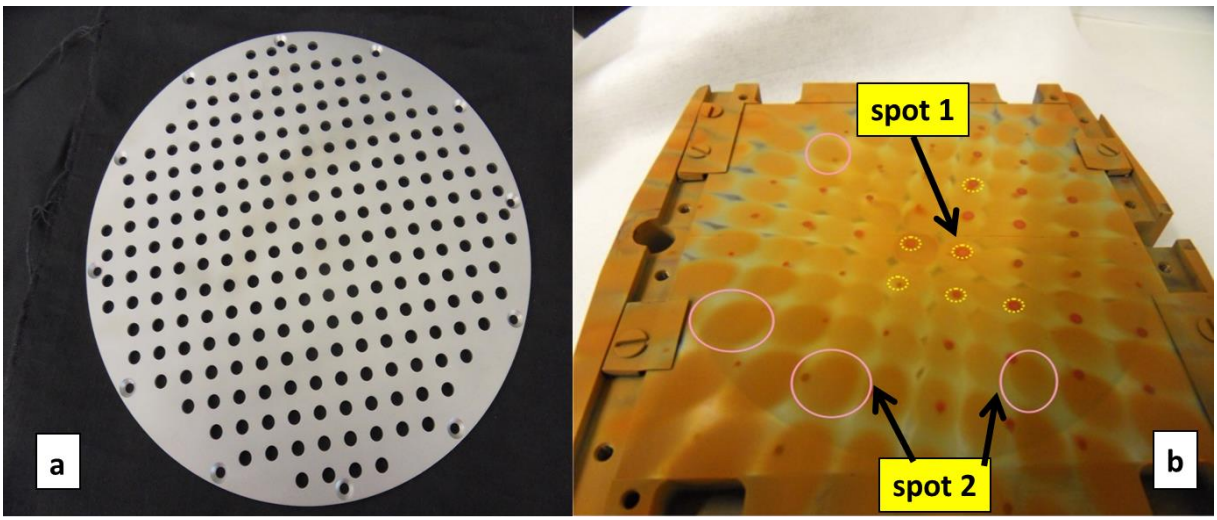

Fig.4.2 (a): The top grounded grid electrode which acts as an assembly of holes through which the nanoparticles escape the plasma zone to reach the substrate (b) : The substrate with nanoparticles formed and collected from the plasma bulk (dotted circles) spot 1 and intense plasma in the holes (solid circles) spot 2.

4.3 Topography of the electrode and the nanoparticles formed

The topography (presence of holes or grooves) of the electrode surface in plasma reactors affects the flow of gases, the plasma, and the layer deposited. The depth and width of the holes in the electrode and the bias applied on the electrode can greatly influence the kind of plasma formed and the nature of the layer. The well-known use of a showerhead electrode for instance in capacitively coupled reactors ensures homogeneous distribution of feedstock gas, preventing depletion and aiding in uniform thin film depositions.

The appearance of luminous plasma-spots in the holes in the cathode (RF electrode), visible even with the naked eye under certain experimental conditions has been reported by various groups [117, 118]. Experimental investigations have revealed that electron-neutral impact excitations and ionization processes play a pivotal role in the formation and sustenance of these spots. The shape, emission intensity, and appearance of the spots depends mainly on the geometry, bias, and potential of the electrode and on the discharge current.

Boundaries of capacitively coupled RF plasma reactors usually include at least one grounded grid or perforated plate for laminar gas flow. When increasing RF powers an intense localized plasma (a plasmoid) can spontaneously ignite in a hole of a grounded grid used to confine an RF plasma [119]. The grounded grid here is used to divide the reactor into two chambers (upper and lower chambers). The upper chamber contains an RF electrode connected to 13.56 MHz generator and matching network, similar to conventional parallel plate plasma reactors. The appearance of the plasmoid is accompanied by the reduction in

DC self-bias voltage, a higher current density and higher energy ions. The RF power density used in this reference was an order of magnitude higher than for usual plasma processing conditions. In this case when the RF voltage was increased to up to 425 V, an intense plasmoid spontaneously ignited in the grounded grid orifice and the self-bias voltage to RF voltage (V_{sb}/V_{RF}) dropped to a strongly negative value of -0.6 V (from an initial value of 0.3 V). Such a strong drop in self-bias voltage could only be interpreted as relative increase in effective grounded area (hence increasing electrode area asymmetry) by the plasmoid presumably by acting as a conducting bridge between the upper and the lower chamber. The only conduction channel for the flow of RF current to the lower chamber is to funnel through the plasmoid hole. It is thought that the bright emission pattern is caused by the momentary extremely high RF current density forced to flow towards the RF electrode sheath. The extremely high RF current density in small cross sections of plasmoids causes intense optical emission and strong heating and is capable of melting and destroying reactor components.

The trajectory in which the electrons are ejected in the plasmoid discharge distinguishes it from a hollow cathode effect. The sheath electric field-lines are divergent in a plasmoid which enables the plasmoid to conduct RF current to external grounded areas which are much larger than its own cross section in contrast to the hollow cathode effect which conducts current only to its small ground area.

Similarly in our nanoparticle reactor, the topography of the holes has a prominent effect on the plasma in the vicinity of the holes, and produces a locally enhanced discharge. The enhancement can be attributed to the stream of highly dense group of electrons which increase the local ionization rate. As the electrons are blocked from the grounded grid electrode due to the potential in the sheath, they can only leave through the narrow holes of the electrode, increasing the electron density at these plasma spots.

The picture of the substrate after deposition is shown in Fig. 4.2 (b). The pattern of particles collected on the substrate mirror the top grounded grid electrode in Fig. 4.2 (a). Two distinct kinds of particles are visible on the substrate. The dotted circles outline the areas where the particles, which are formed in the bulk of the plasma, are collected and henceforth, these locations will be called spot 1. The solid lines outline the area where the particles, which are formed due to the locally enhanced plasma in the holes, are collected and, henceforth will be called spot 2. The collection of particles produced due to the locally enhanced plasma form bigger spots and covers a greater area, this is because the particles created here have a larger escape angle in contrast to the particles formed in the bulk, and this can clearly be seen in Fig. 4.2 (b), Fig. 4.3 and Fig. 4.4. As is evident in Fig. 4.2 (b), there are two distinct kinds of particles which according to our hypothesis have their origin at two different places in the plasma. These particles have different structural and optical properties. The particles grown in the plasma bulk are significantly large (~100 nm) crystalline agglomerates, and the particles produced at the locally enhanced discharges are a mixture of crystalline particles (2-5 nm) and amorphous particles (10-25 nm). Hence to

synthesize quantum sized particles, care must be taken that large particles are not produced in the bulk (example by pulsing), details can be found in chapter 5.

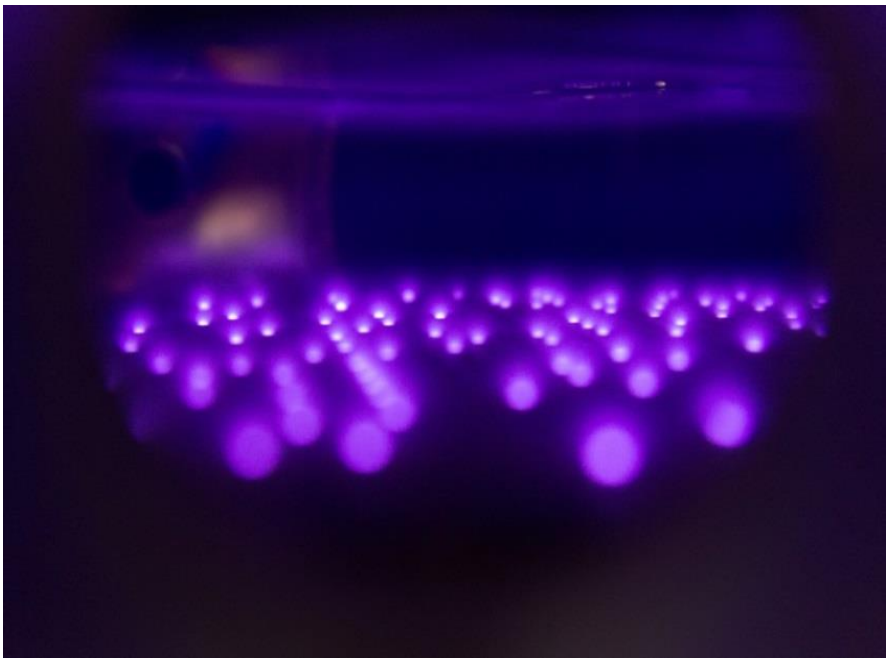

Fig. 4.3: Intense plasma formed in the assembly of holes, visible at the top of the grounded grid electrode. The areas of the plasma spots at the outlet are larger than the size of the holes, in accordance with the larger spots found on the substrate.

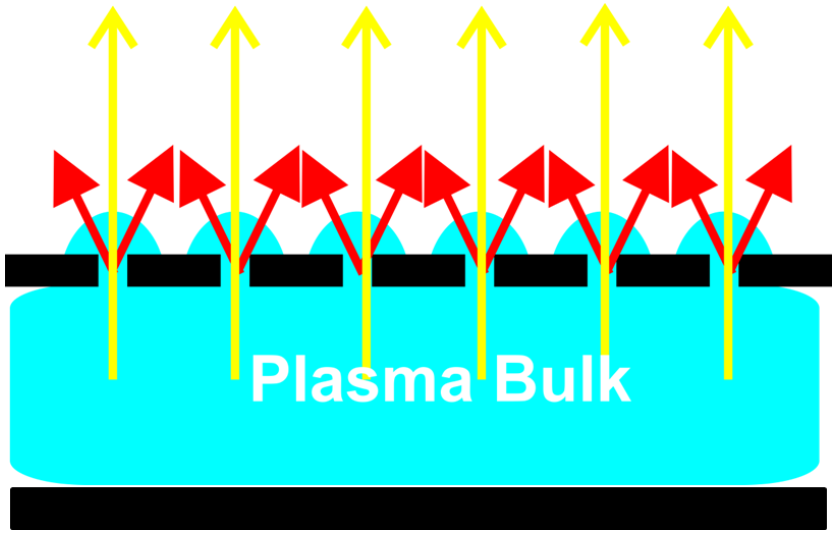

Fig. 4.4: The cross sectional schematic image of proposed particle origin and flow from bulk and locally enhanced plasma regions to the substrate. The red lines indicate the direction of flow of particles from the locally enhanced discharges and the yellow lines indicate the flow of particles from the bulk plasma.

4.4 Characterization of crystallinity and discussion

The Raman spectra of the as-deposited films at both the spots are given in Fig. 4.5 (a) and (b). Both spectra are fitted after base-line correction taking into account the TO (transverse-optic), LO (longitudinal optic), LA (longitudinal acoustic), of amorphous phase and the TO peak of crystalline grains and GB (grain boundaries). We observe that spot 2 has a spectrum dominated by a broad peak centered at 478 cm^{-1}, which is characteristic of a-Si:H films.

For particles at spot 1, dividing the area of TO peaks of crystalline grains and GB to the total TO area (amorphous +crystalline peaks), the Raman crystalline fraction R_c can be calculated as

$$R_c = \frac{I_C + I_{GB}}{I_A + I_{GB} + mI_C} \qquad \text{Eq (4.1)}$$

For a small grain size, we can take the calibration factor as unity, with m=1, we obtained Raman crystalline ratio of 81.24 % (neglecting stress effect). Stress free nature of Si NC's synthesized in the gas phase are by virtue of their free standing morphology [24].

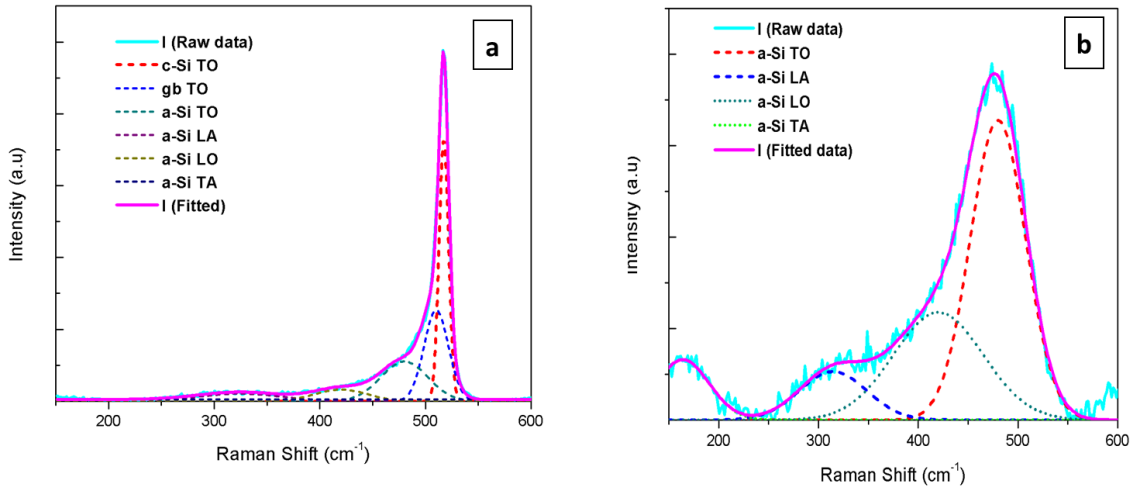

Fig. 4.5: Raman spectra of particles at (a) spot 1 and at (b) spot 2 on the substrate. Fitting curves of the transverse acoustic (TA), longitudinal acoustic (LA) , longitudinal optic (LO) vibration peaks of the amorphous and of the transverse-optic (TO) vibration peaks of amorphous, grain boundary, and crystalline components are also shown.

Our observed Raman shift is about 6 cm^{-1} from the bulk c-Si Si-Si TO peak, which indicates that the particles have a mean size of 4 nm [120]. This relation between the Raman shift and particle size is calculated in ref [120] using the phonon confinement model where dispersion is calculated in the Keating model. The presence of grain boundaries for particles with sizes less than 20 nm leads to the confinement of phonons which strongly alters the vibrational properties of the silicon nanoparticles. The translational symmetry of such a

crystal lattice of finite size is no longer conserved [121]. This leads to a red shift of the phonon peak for smaller nanocrystals. The smaller the crystal, the more intense is the phonon confinement effect and consequently the larger the red shift.

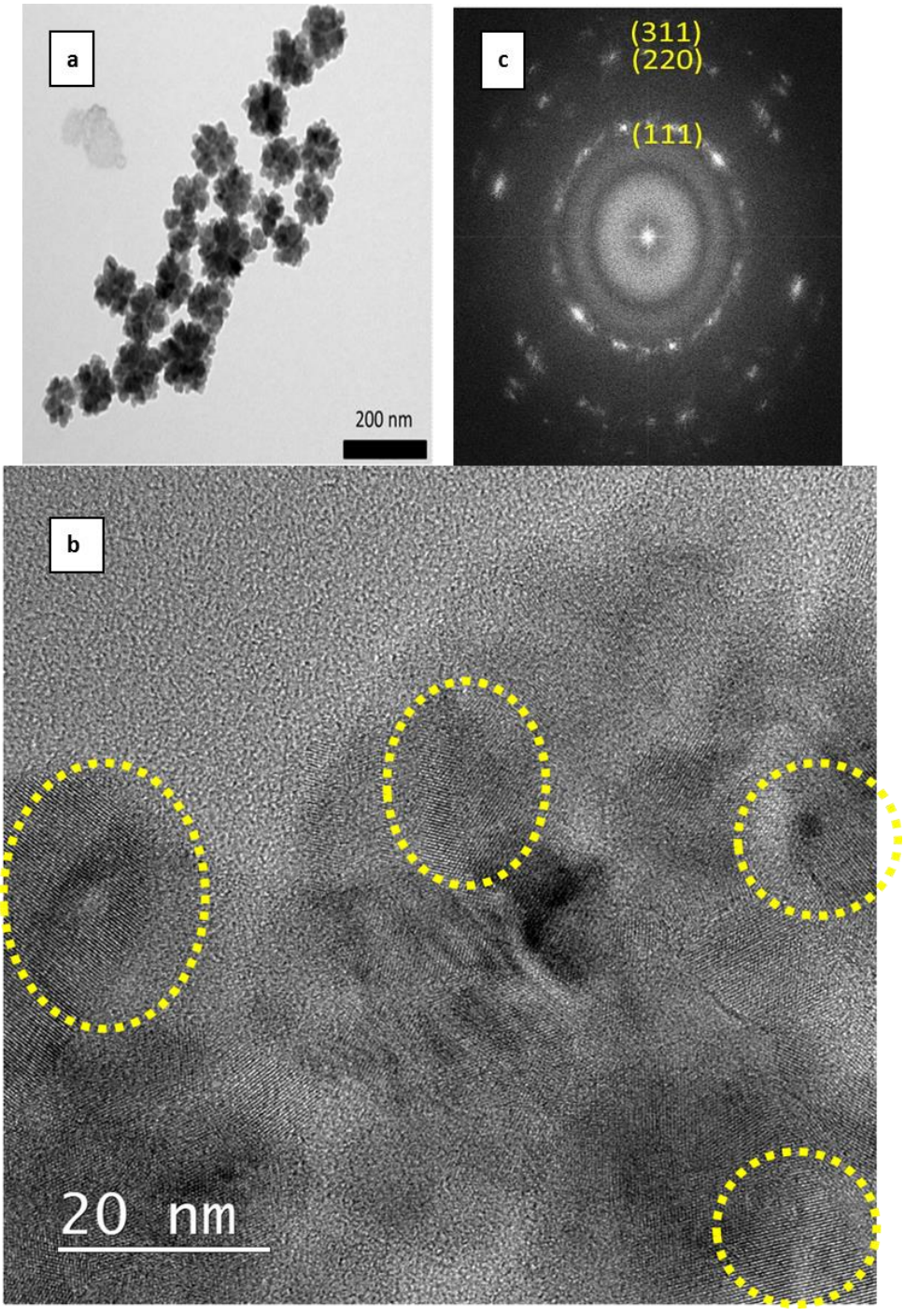

Fig. 4.6: (a) TEM image of particles collected at spot 1 which exhibit a cauliflower structure; (b) HRTEM image of a cauliflower structured nanoparticle which shows crystallites of multiple crystalline orientations and sizes; (c) the corresponding Fast Fourier Transform (FFT) pattern, displaying the characteristic periodicities of crystalline Si, indicated by the corresponding Miller indices.

To further study the nanoparticles morphology, size, and crystalline orientation, TEM and HRTEM studies have been performed. It is found that the crystalline nanoparticles which are collected from spot 1 have a cauliflower conglomerate structure as seen in Fig. 4.6 (a). Parts of these cauliflower structures which have a conglomerate size of 100 nm in our case, are composed of smaller crystalline subsystems, which is revealed by HRTEM fringes (Fig. 4.6 (b)). Detailed microscopic and time evolution studies of the cauliflower like conglomerates are provided in chapter 5. Similar cauliflower-like structures have been studied in capacitively coupled plasmas before and have been found to be composed of "primary" systems of crystalline 2-nm sized nanoparticles [83]. As proposed by Boufendi and Bouchoule, these primary nanocrystals are formed in the first few milliseconds of the plasma, and they coagulate successively to grow into large cauliflower-like nanoparticles. By measuring 25 particles in the HRTEM images we found the average size of primary particles to be 4 nm, which corresponds to a Raman shift of 6 cm^{-1}. Hence we find a good agreement between the size correlated with the Raman shift as obtained by Raman spectra and the direct size determination by HRTEM studies.

However the particles collected from spot 2 consist of two different kinds of particles, the differences being evident in their size and crystallinity. Spot 2 is predominantly dominated by numerous amorphous nanoparticles (Fig. 4.7 (a and b)) in addition to a smaller fraction of crystalline nanoparticles Fig. 4.8 (a). All particles are free standing and particle sets of each type (amorphous, crystalline) are found to be almost monodisperse. The smaller particles are usually found in the vicinity of the larger ones and are overshadowed by the larger ones while imaging. This could be one possible reason why the Raman spectrum of spot 2 displayed amorphous characteristics only. Moreover we would like to point out that despite having crystalline particles less than 5 nm, we could not observe any photoluminescence; this again can be traced to the fact that the larger amorphous nanoparticles greatly outnumber the smaller crystalline ones.

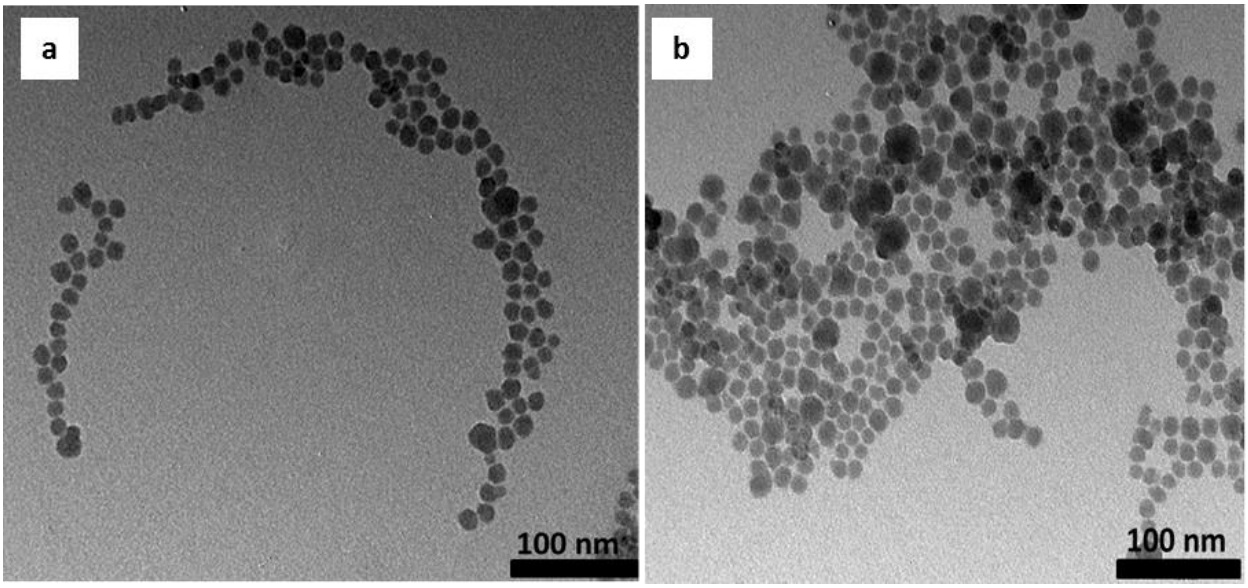

Fig. 4.7: (a) and (b) TEM image of amorphous free-standing nanoparticles found in spot 2

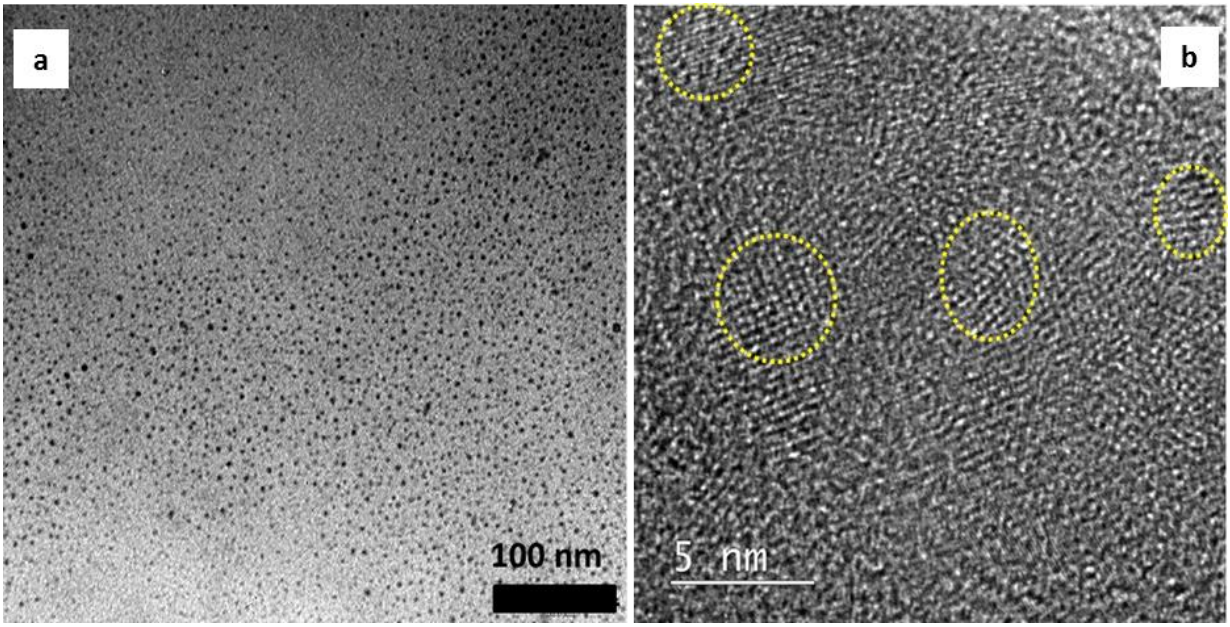

Fig. 4.8: (a) TEM image of crystalline nanoparticles found in spot 2 (b) HRTEM image of the same particles showing lattice fringes.

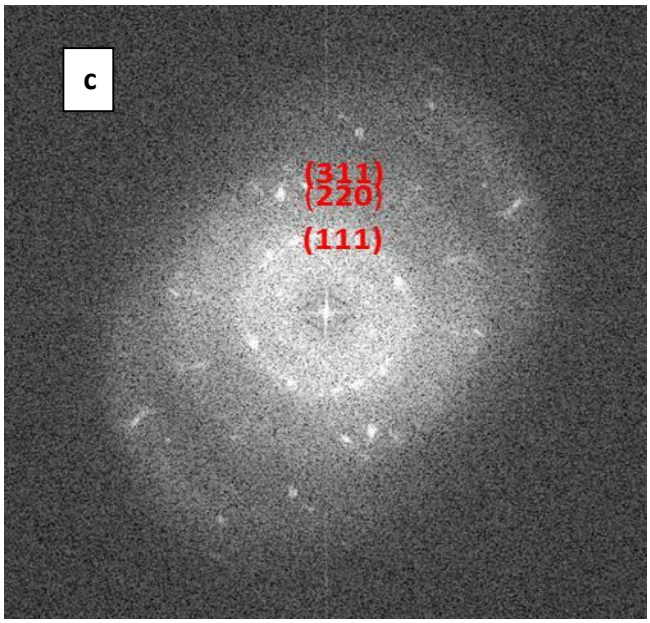

Fig. 4.8 (c) the corresponding FFT pattern of Fig. 4.8 (b) displaying the characteristic periodicities of crystalline Si.

Approximately 200 particles are counted at each spot to make the statistical size distribution, which is given in Fig. 4.9 (a and b). The particles at spot 2 have a bimodal size distribution with one group of smaller particles having a mean size of 2.95 nm (with a standard deviation of 0.85 nm) and the other group of larger particles with a mean size of 15 nm (with a standard deviation of 3.9 nm). The trends of both small and large particles show a

lognormal behavior, which is typical for nanoparticles formed in vapor growth process due to the influences of drift and diffusion forces during nucleation [122]. The drift is caused by the gas flow around the electrode as well as by a convection current in the gas that would be present even if no flow was applied.

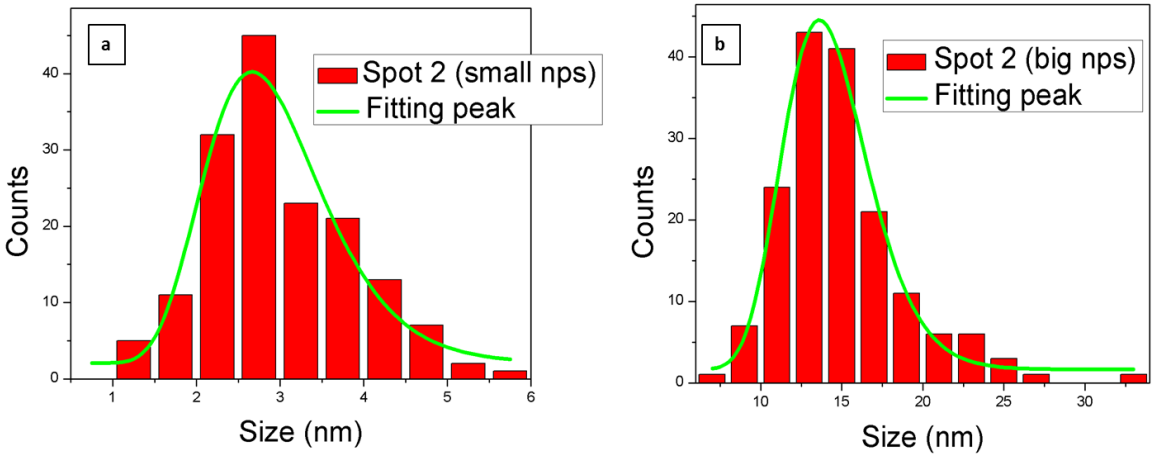

Fig. 4.9: (a) Size distribution of small NPs and (b) large NPs found on spot 2 which exhibit a lognormal size distribution

To further establish the crystallinity and correlate this to the size of the nanoparticles produced in the nanoparticle reactor, GI XRD measurements were performed on the synthesized particles. For the recipe of the particles reported in this chapter, the XRD measurements only yielded an amorphous signal. The lack of crystalline peaks in the XRD spectrum does not imply the absence of crystalline particles as crystallinity was confirmed by HRTEM and Raman spectroscopy for the cauliflower particles. We assume the absence of crystalline peaks could be because the deposited layer of silicon NPs was thin and the NP density was sparse.

To collect more particles and to get a better GI XRD signal, we increased the silane feed gas flow from 2 sccm to 8 sccm keeping all other parameters constant (25 sccm of H_2, reactor pressure of 0.8 mbar, forward power of 70 W and reflected power of 1 W) and synthesized the NPs. Higher flow of silane provides more precursors for growth, hence increase of deposited material on the substrate and higher XRD intensity. We found the same pattern on the substrate with two spots due to the nanoparticles formed in the bulk and those formed in the locally enhanced regions. The GI XRD spectrum was obtained from the crystalline particles in the bulk, (spot 1 mentioned in the sections above). This GI XRD spectrum is given in Fig. 4.10.

Because of the nature of the sample the amorphous signal from the glass substrate could not be suppressed to prevent a high background signal. Therefore only the three strongest silicon diffraction peaks are visible in the diffraction scan. This however provides

sufficient proof for the presence of nanocrystalline silicon in the sample. The diffraction angles of the three peaks are 28.4°, 47.3° and 56.8° corresponding to Si (111), (220), (311).

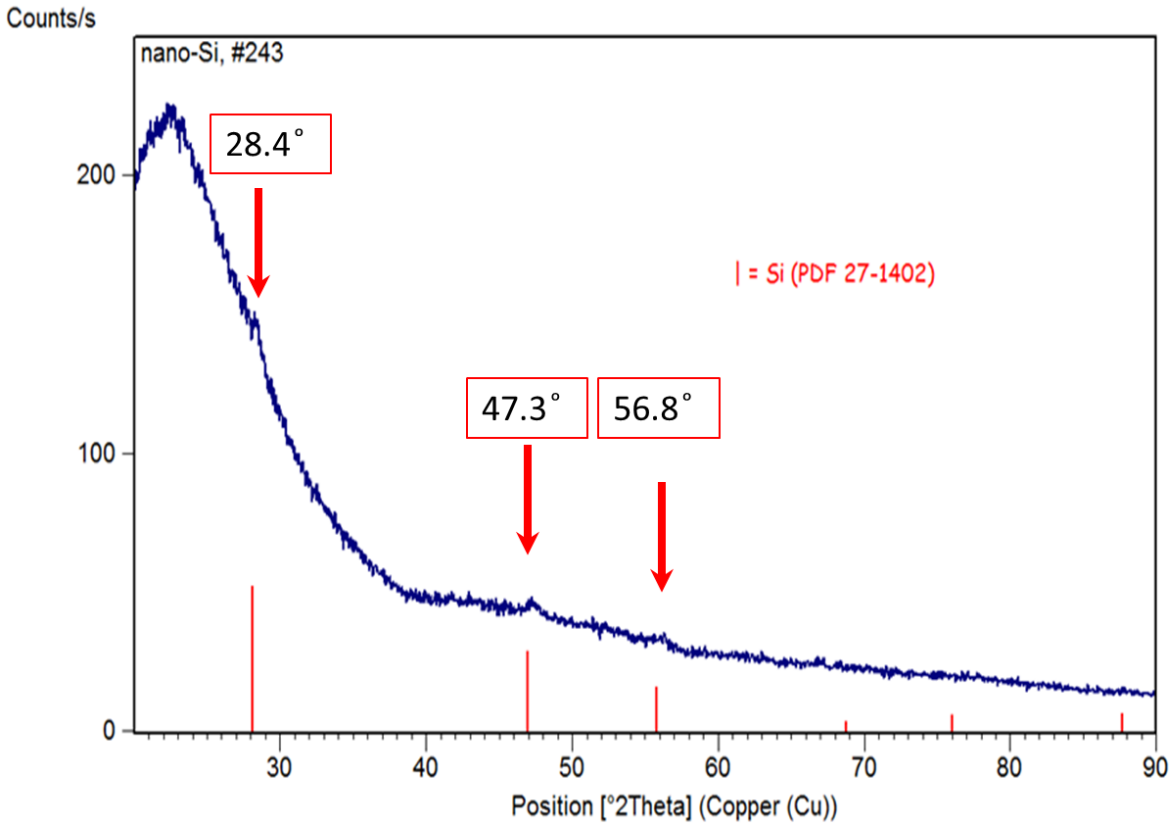

Fig. 4.10: GI XRD pattern of silicon NPs deposited with a flow of SiH_4:H_2 of 8: 25 sccm at a pressure of 0.8 mbar and 70 W forward power. The large peak at 22° is the background signal from the Corning substrate.

Although all the peaks acquired in the diffraction pattern are small compared to the noise, the peak positions are compared with that of reference silicon. Subtracting the amorphous background signal, with the obtained peak width and applying Scherrer equation [75], the mean size of the crystallites is determined. From the peak width (of 28.4°peak) we estimated the crystallite size to be 5 nm. However this method does not take into account the sub-distribution or bimodality of particle size and provides only an estimate average size. Although more sensitive measurements such as TEM and HRTEM give a better gauge of the particle size distribution, GI XRD measurements were done for completeness.

The TEM and HRTEM images of the particles deposited at higher silane flow (8 sccm) are shown below. We see the same trend as with lower silane flow in terms of the shape, size and crystallinity of the particles. Spot 1 (particles formed in the bulk) was dominated by cauliflower shaped agglomerates in addition to spherical particles (Fig. 4.11 (a)). Both the particles are partly crystalline. Particles found at spot 2 were predominantly amorphous spherical particles (Fig. 4.11 (b)), although a few cauliflower agglomerates were found, which could have happened during collection of particles for TEM after deposition. This recipe in

addition to having a much higher deposition rate also showed more clustering of particles. We could however, by TEM not detect any quantum sized particles in this case, which could be because it is difficult to discern the individual small particles in the cluster while imaging.

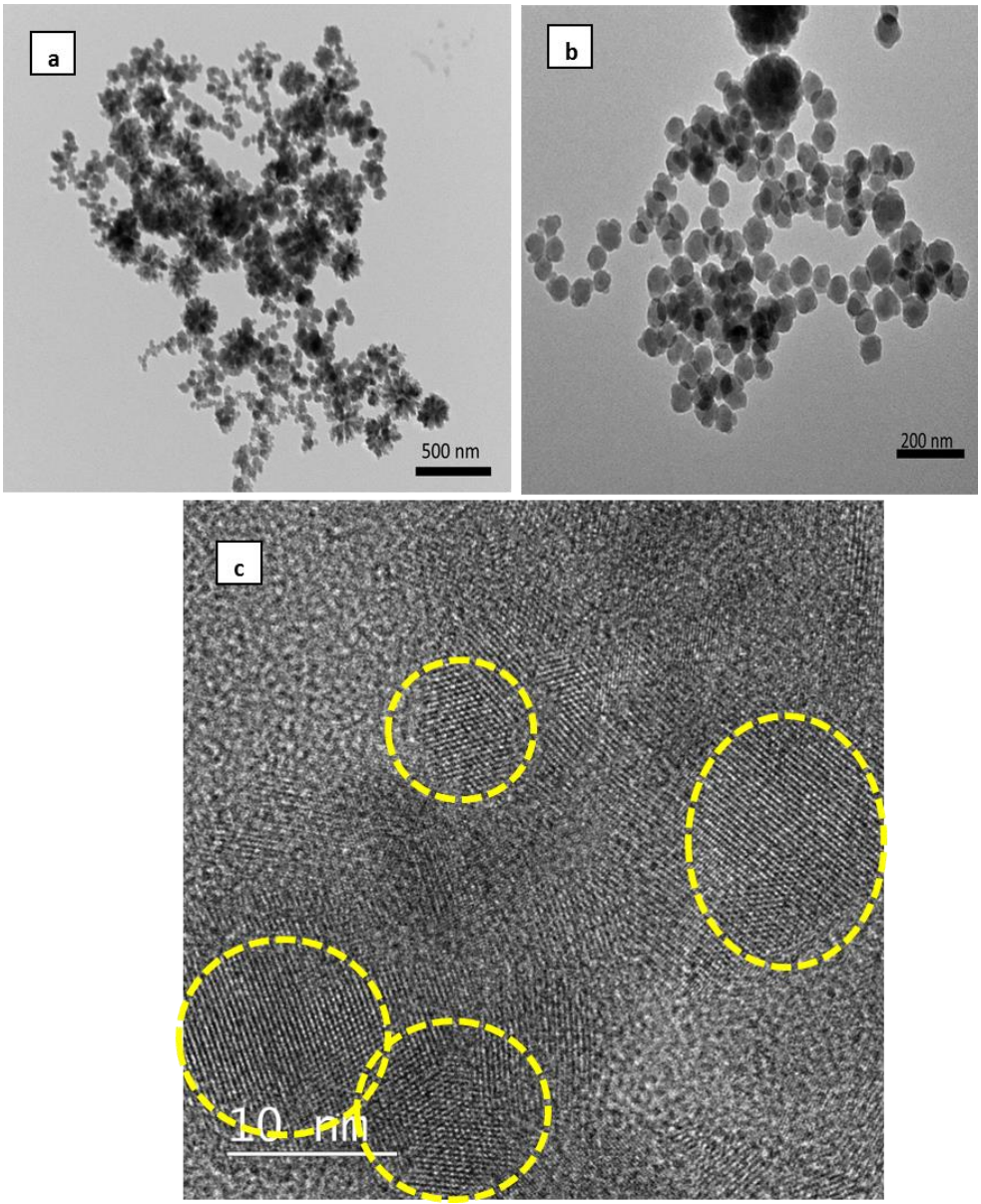

Fig. 4.11 (a): Cauliflower shaped agglomerates with spherical particles found at spot 1 for higher flow recipes (8 sccm of SiH_4) (b) amorphous particles found at spot 2 for higher flow recipes (8 sccm of SiH_4) (c) HRTEM image of a cauliflower structured nanoparticle which shows crystallites of multiple crystalline orientations and sizes.

From the above experiments it is evident that the particles formed due to the locally enhanced discharges (spot 2) have crystalline nanoparticles with more favorable characteristics, such as being monodisperse free standing quantum sized particles, usually at small silane flow conditions. (Although particles in spot 2 has bimodal size distribution, both groups of particles (amorphous and crystalline) are monodisperse.) By optimizing the design of the grid electrode, for instance by changing the dimensions of the holes, optimum

parameters of p, w (pressure, hole width) product can be reached, which can have a profound influence on the particles formed due to the locally enhanced plasma. We expect variation of electron density and ionization, by varying the hole width, w. Additionally, tailoring the bulk plasma parameters is possible by changing the inter-electrode distance, d. More details on change of electrode distance, d and variation of particle size, is reported in chapter 6. As the gas residence time $\tau \propto p.d$, decreasing pressure, inter-electrode distance, or a combination of the two could lead to the suppression of the bigger particles.

It has been shown by plasma simulations in CFD-ACE multiphysics software that locally enhanced discharges occur at electrode holes both in the upper electrode and lower electrode, i.e. grounded as well as powered electrode [123]. For capacitively coupled plasma reactors, locally enhanced discharges are caused by a high density of electrons streaming from the bulk through the electrode holes. Due to the impedance of the grooves to the gas flow, the pressure in the vicinity of the grooves is much higher than the process pressure of the reactor. This high pressure is also essential to sustain a plasma at such small dimensions of the grooves. The higher pressure at the grooves results in an enhancement of ionization rate at the gas-hole openings. Plasmas in the holes at both the electrodes are shown to provide a strong supplemental source of energetic electrons [123]. In our case these locally enhanced discharges were observed visually by the appearance of luminous spots, presumably caused by the electron-neutral impact ionizations by the accelerated electrons. A strong local heating on the particle surface (as explained below) caused by this process may also contribute to the nanocrystal formation in such a plasma. Another possible mechanisms to explain the observed intense plasma behind the perforated grounded electrode is the transport of plasma current through the holes via a plasmoid, concomitant with intense optical emission [119].

The thermodynamics of the creation of crystalline particles in the plasma may be explained by the presence of free electrons and ions that recombine at the particle surface in a highly exothermic reaction. It has been reported that this type of reaction can heat the nanoparticles to temperatures significantly higher than 1400 K, and contributes to providing a suitable environment for the synthesis of nanocrystals with a diameter of less than 10 nm in a few milliseconds [39, 124]. The excess electrons also impart unipolar negative charges to the particles, which suppresses agglomeration [50].

The locally enhanced plasma in the electrode holes thus presents several advantages and provides a beneficial environment for the formation of crystalline free standing nanoparticles, thanks to the presence of excess energetic electrons. The characteristics of particles created here could be highly desirable for optoelectronic devices exploiting the quantum confinement effect. There are of course other types of particles, and tuning the plasma properties (especially pulsing) can aid in their elimination.

4.5 Conclusions

We report the design and operation of a dedicated plasma reactor for the gas phase synthesis of silicon nanoparticles. The proof of concept of the operation of this reactor is provided by demonstrating a fast and simple technique to synthesize non-embedded, non-agglomerated free standing silicon nanoparticles. Two ensembles of particles have been synthesized and the origin of these nanoparticles can be traced to two different places in the plasma, one being created in the bulk and the other due to the locally enhanced plasma in the holes of grounded electrode. They have significantly different characteristics in terms of size, shape, and crystallinity. We highlight that the locally enhanced plasma has a pronounced effect on the particle formation and it contributes to the formation of, among other particles, free standing quantum sized crystalline nanoparticles due to the presence of excess energetic electrons.

Chapter 5: Microscopic studies of polycrystalline nanoparticle growth using pulsed plasmas ‡

Abstract

Pulsed plasmas are used to obtain particles with a narrow size distribution. Using multiple microscopic techniques, we have extensively studied the growth and crystallization of silicon nanoparticles in pulsed SiH_4/Ar plasmas. We observe that the crystallinity of the particles can be tuned from amorphous to crystalline by altering the plasma ON time, t_{ON}. Three phases can be identified as a function of t_{ON}. Microscopic studies reveal that, in the initial gas phase (phase I) single particles of polycrystalline nature are formed, which according to our hypothesis grow out of a single nucleus. The individual crystallites of the polycrystalline particles become bigger crystalline regions, which marks the onset of cauliflower shaped particles (phase II). At longer t_{ON} (phase III) distinct cauliflower particles are formed by the growth of these crystalline regions by local epitaxy.

The role of plasma OFF time, t_{OFF} is studied to tailor the size of the silicon nanoparticles. Various t_{OFF} durations are chosen, both longer and shorter than the residence time of the gases in the discharge. Time resolved optical emission spectroscopy (TROES) studies provide additional information about the growth precursor dynamics during plasma modulation. Transmission electron microscopy (TEM) studies reveal that a t_{OFF} longer than the residence time is favorable for the formation of quantum sized silicon particles.

‡ Published as
A. Mohan, I. Poulios, R.E.I. Schropp and J.K. Rath. "Size control of gas phase grown silicon nanoparticles by varying the plasma OFF time in silane pulsed plasma" *Mater. Res. Soc. Symp. Proc* **1803** (2015) DOI: https://doi.org/10.1557/opl.2015.476
A. Mohan, M. Kaiser, M. A. Verheijen, R.E.I. Schropp and J.K. Rath "Microscopic studies of polycrystalline nanoparticle growth in free space." *J. Cryst. Growth* **467** 137 (2017) DOI: http://doi.org/10.1016/j.jcrysgro.2017.03.044

5.1 Pulsing of plasma to effectively control NP size

The size and size distribution of nanostructures of materials have a strong influence on the optical and electrical properties and thus precise control of the particle size is a prerequisite to exploit their size dependent optoelectronic properties. Precise size control of NPs in a plasma enhanced chemical vapor deposition (PECVD) can be obtained by varying the gas residence time in the discharge region or by altering the plasma ON (t_{ON}) and OFF time (t_{OFF}) by pulsing the radio frequency (RF) power. Longer t_{ON} resembles a continuous plasma condition and leads to the saturation of particle sizes. Pulsed RF discharge is known to be very effective in suppressing powder formation in the discharge volume [125]. Fine tuning the parameter space with this technique, pulsing of a silane plasma made by RF PECVD has shown to help the growth of quantum-sized nanocrystalline silicon (nc-Si) particles with a narrow size distribution [31]. By reducing the duration of t_{ON}, growth times of the particles and hence, the size of the NCs can be reduced. As a consequence the photoluminescence (PL) spectra have been tuned, by changing the t_{ON} [33]. Nanoparticle growth can be interrupted by turning OFF the plasma. Plasma OFF time (t_{OFF}) plays a very important role in disrupting the growth of particles due to the removal of existing particles by refreshing the process gases.

5.2 Multistep growth process of NPs

One of the first experimental evidences of a multistep growth process of NPs in a silane-argon low pressure discharge was given by Bouchoule and Boufendi [114], who interpreted their results by invoking a process that involves nucleation and agglomeration, followed by silicon deposition on growing particles. An analytical model of the particle growth is considered and shown to be a three step phenomenon [80]. According to this model, a first generation of super small (2 nm) particles grows as a chain of negative ion molecular reactions, stimulated by molecular vibrational excitation. As the cluster size increases, their probability to react with vibrationally excited molecules decreases, limiting the size of first generation particles. The negative ions and particles, as well as the neutral particles which have acquired a negative charge are trapped in the discharge. During the agglomeration phase the NPs acquire more negative charge and the Coulomb repulsion becomes stronger. After a certain threshold value, the agglomeration phase stops and the NPs continue to grow by radical deposition on their surface [114]. These trapped particles coagulate and a critical phenomenon of α to γ’ transition takes place when the particle size increases and their concentration in the plasma decreases dramatically, altering the plasma parameters [126]. A detailed explanation of the dust formation in silane plasma and α to γ’ transition is given in sections 3.1 and 3.2. This theoretical approach is in good agreement with effects observed in experiments. In this chapter we show that the nanoparticles *do not*

always grow according to the aforementioned agglomeration mechanism. Experiments done in expanding thermal plasma (ETP) support our hypothesis that particle formation in their system (and possibly in the systems where particle formation is strongly governed by drift and diffusion in finite growth regime) does not follow the commonly believed sequence of nucleation, agglomeration, and coagulation [24].

For long plasma durations (e.g. t_{ON} >10 s), which is equivalent to a continuous plasma, occurrence of several well-defined particle sizes, corresponding to successive (in time) particle generations has been observed. Transmission electron microscopy (TEM) studies of Si NPs grown/formed in various plasma processes in capacitively coupled discharges show cauliflower morphology with smaller crystalline subsystems [83, 127]. The luminescence decay time of cauliflower shaped Si NPs produced in a cluster source by magnetron sputtering has been shown to be enhanced by a thousand times by embedding in vacuum grease [128]. Although the mechanism of formation of these structures is not fully understood, the commonality between them is that they are composed of smaller crystalline subsystems.

5.3 Nanoparticle properties by varying t_{ON}

The aim of the research described in this chapter is to study the NPs growth as a function of time in a silane plasma and propose a mechanism that ultimately leads to the observed cauliflower structured particles. In the following sections of this chapter, we report our observations on the formation and crystallization of the nanoparticles at different t_{ON} time in the gas phase by HRTEM studies.

5.3.1 Experimental details

For the particles mentioned in this section, a SiH_4:Ar flow ratio of 4 sccm:50 sccm was used for the particle synthesis at a pressure of 0.8 mbar. A forward VHF power of 150 W was applied to the showerhead electrode, and the substrate stage was unheated. The forward power was pulsed, and a range of plasma ON time (t_{ON} = 0.05 s to 60 s) was applied to study particle crystallinity using Raman spectroscopy. To study the time evolution of particle sizes and their crystallinity using HRTEM we restrict to particles synthesized with t_{ON} = 0.05 s to 6s. For each plasma ON time (t_{ON}) the discharge was sustained multiple times for a total duration of 45 min. The plasma OFF time (t_{OFF}) was kept constant at 2 s (which is longer than the residence time of gases in the reactor) for all t_{ON} durations. The growth time of the particles is determined by the gas residence time in the discharge. Residence time of the gases in a reactor depends on process pressure of the source gases, total flow of the gases used and the volume of the reactor. For the dimensions of our reactor the residence time (t_{RES}) of the gas was found to be ~1 s.

Structural characterization of deposited particles has been done with a Tecnai 10 and a JEOL ARM 200 transmission electron microscope operated at 200 keV. This accelerating voltage – together with the beam doses used – is sufficient to avoid defect generation in bulk silicon. As nanoparticles may be more sensitive to electron beam irradiation than the bulk, care was taken to minimize the dose used for imaging. Comparison of images taken from the same area at various stages of the TEM study did not show any tendency to particle coalescence. Fast Fourier Transform (FFT) analysis of High Resolution TEM (HRTEM) images was used to detect local crystal orientations within the particles studied. Analysis of the periodicities in each of the FFT patterns yielded lattice constants that were within 1% of the 0.5428 nm lattice parameter of diamond-cubic silicon. The crystalline ratio was calculated [74] from Raman spectra obtained ex situ with an inVia Renishaw microscope equipped with a laser with a wavelength of 514.5 nm.

5.3.2 HRTEM studies of NPs at various t_{ON}

To understand the time evolution of the formation of particles and their progress into cauliflower shaped particles, the properties of the collected particles are studied as a function of t_{ON}. Optical and structural studies are performed on particles with t_{ON} from 0.05 s to 6 s at a constant t_{OFF} time of 2 s which is longer than the estimated residence time of the gases (1 s) in the reactor.

The TEM images of the NPs grown at different t_{ON} indicate that there are various successive phases in the particle formation (Fig. 5.2). Phase I corresponds to NPs grown with $t_{ON} \leq 0.5$ s, phase II corresponds to NPs with $0.5 \text{ s} < t_{ON} \leq 2$ s and phase III contains NPs grown with $t_{ON} > 2$ s. A schematic representation of NPs in the 3 successive phases is given in Fig. 5.1. The size of the particles increases with increasing t_{ON}, as expected [33, 129]. From here on the term ‘‘clustered NPs” refers to unpassivated silicon nanoparticles which tend to aggregate into larger clusters facilitated, among others, by the dangling bonds on their surface [130, 131]. The term ‘‘agglomerated NPs” correspond to the coalescence or merging of polycrystalline NPs of which the single crystalline regions (domains) grow out to become NPs with larger domains.

TEM images of phase I NPs show open 3-dimensional (branched) networks of particles that have a size of a few nm, whose formation may be attributed to polymerization. It is proposed that the polymerization pathway propagates via the negative ions [132]. A theoretical investigation proposes that negative ions are the precursors to large clusters which are nucleation centers for particle formation [133]. This is attributed to the longer average residence time experienced by negatively charged clusters, which allows growth of large clusters to occur. Individual particles have not been observed, which may either be due to their limited contrast on the supporting carbon membrane or because they are not present at all. The crystallinity of the NPs formed in the early stages of phase I could not be determined, most likely because of oxidation during transfer from the growth reactor to the

TEM setup or simply because they are inherently amorphous. For brevity we will refer to particles of phase I as 'amorphous'. However NPs in the later stage of phase I (t_{ON} = 0.5 s), did show crystallinity and detailed HRTEM of these are reported in the following sections. NPs observed in phases II and III have a well-defined morphology and are found both as individual and clustered particles. This distinction in morphology can be understood from the difference in residence times of the particle precursors within the plasma zone. A report from Costa et al. [134] supports this argument and it can be formulated that the initial growth of Si powder starts with the appearance of small particles due to polymerization and as the residence time increases, cross linking between the polymeric chains increases and more compact particles are formed. The first hint of the onset of cauliflower shaped particles occurs at phase II (t_{ON} of 2 s); detailed extensive HRTEM studies on these particles are reported in the following sections. While the NPs found in phase I and II predominantly have single type of particles, in phase III, i.e. for longer t_{ON}, different ensembles of particles are observed. It is beyond the scope of this chapter to discuss all the different ensembles of particles and we focus our attention on the dominant particles obtained in phase III, the cauliflower shaped NPs.

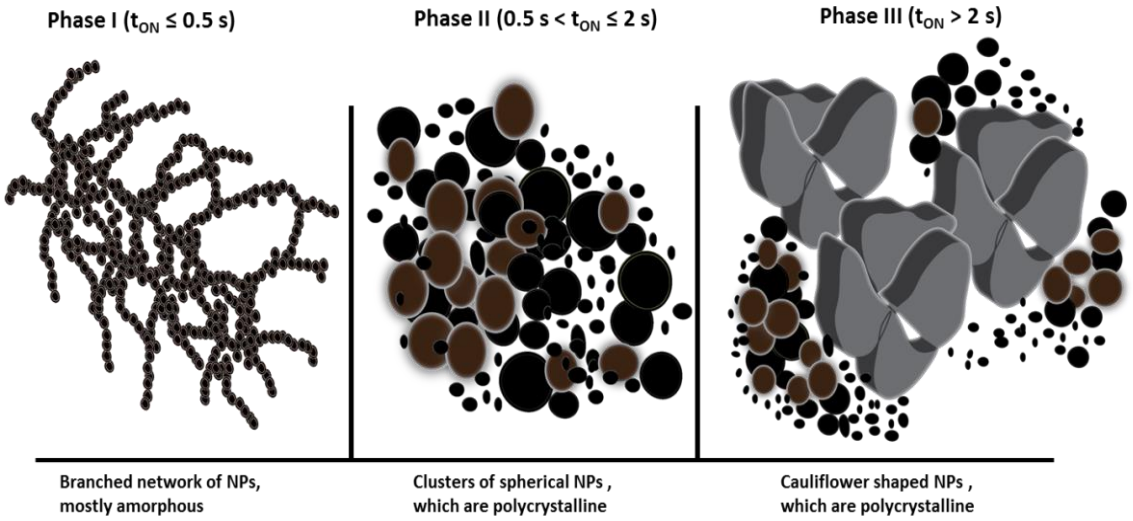

Fig. 5.1 : Schematic representation of three successive phases of particle formation and the characteristics of the NPs formed.

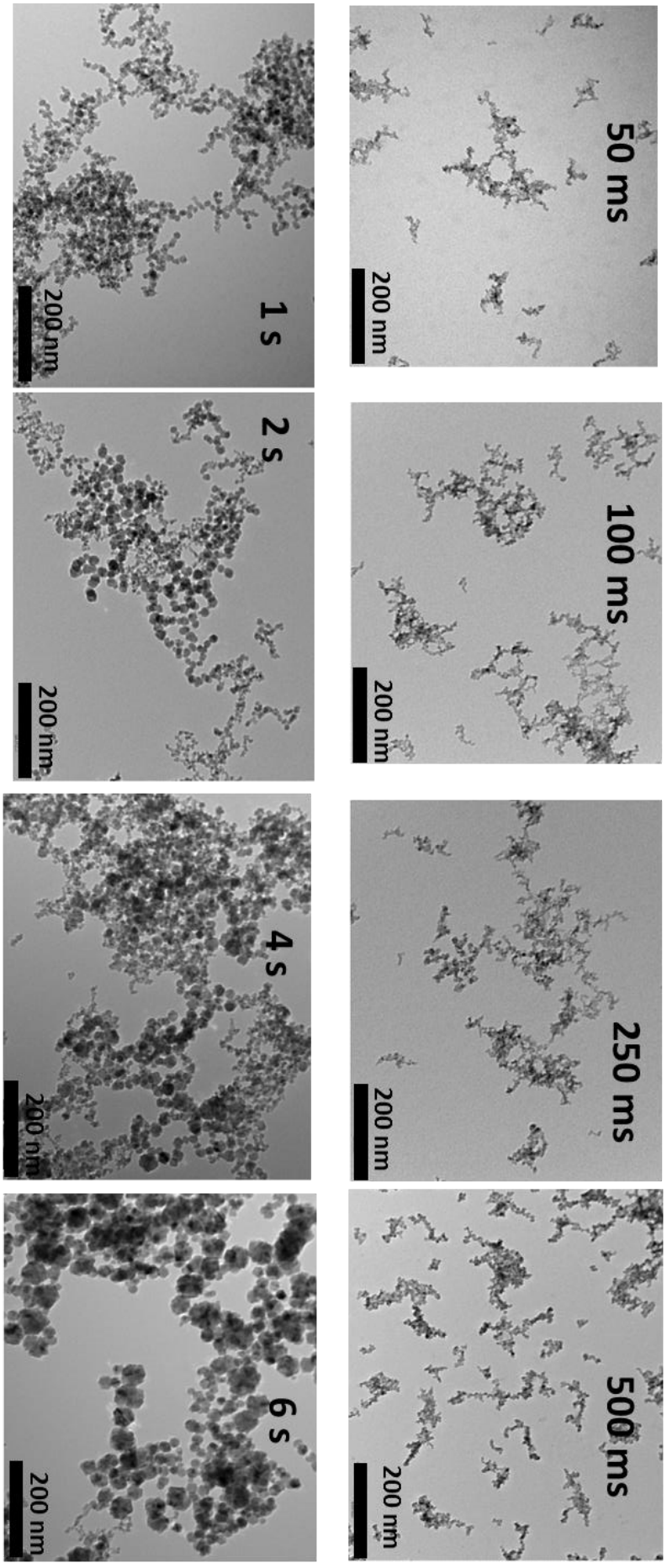

Fig 5.2: Top view TEM images showing the time evolution of NPs at various t_{ON}

It is of interest to note that the crystallinity, estimated from the Raman spectra [74], of the particles depends on t_{ON}, as shown in Fig. 5.3. For short t_{ON} times, i.e. during phase I (from 0.05 s to 0.25 s), only amorphous particles are produced. In our case discernible crystallinity sets in at the end of phase I (at 0.5 s) and gradually increases with t_{ON}. For particles produced at 0.25 s, although in HRTEM a few particles were found to be crystalline, the Raman signal still had only the amorphous peak. At t_{ON} of 0.5 s, a small crystalline peak near 520 cm^{-1} makes an appearance against the background of a broad amorphous spectrum. From then on the crystalline fraction gradually increases with increasing t_{ON}, and saturates for longer times. A pulsed plasma with t_{ON} > 10 s is indeed almost equivalent to a continuous plasma, with respect to the formed particles.

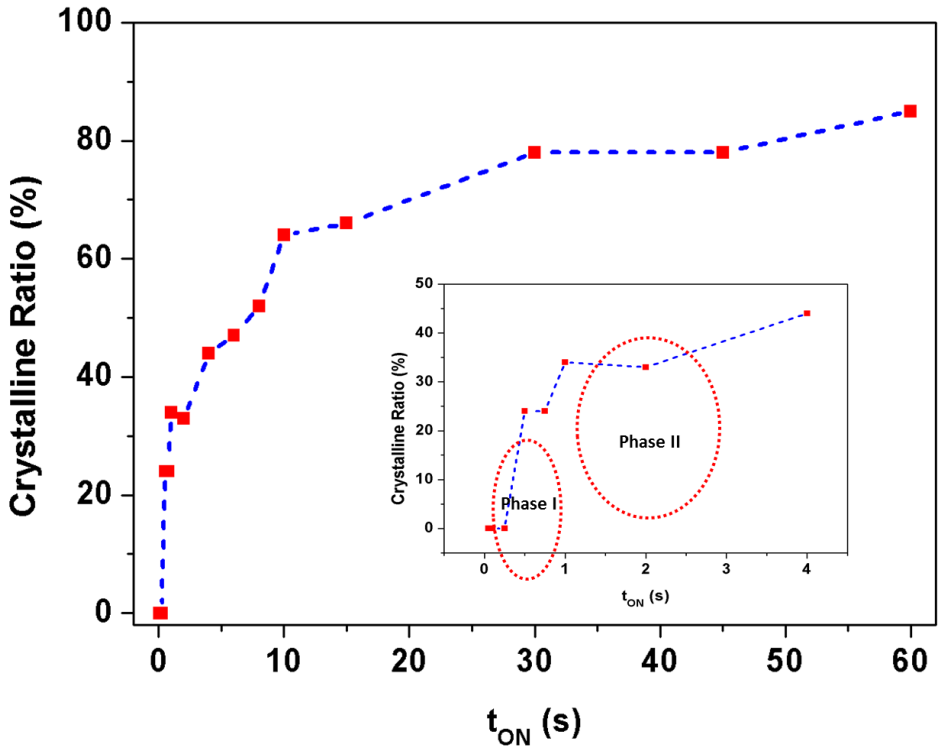

Fig. 5.3: Raman crystalline ratio of the deposited NPs as a function of t_{ON}. The inset gives the zoomed in image at the smaller values of t_{ON}, indicating the early phases I and II by the dotted circle.

Various plasma process parameters such as coupled power, process pressure, gas flow and inter-electrode distance play crucial roles in determining the size and crystallinity of the synthesized Si NPs. We have performed an extensive study on the synthesis of silicon NPs in the gas phase in the capacitively coupled VHF discharge monitoring crystalline ratio as a function of the above parameters and highlighted the interdependence of crystalline ratio and residence time, given in chapter 6 [135]. The crystalline ratio is determined by surface effects driving local epitaxial growth.

5.3.2.1 HRTEM of particles produced at t_{ON} = 0.5 s (Phase I)

As stated above, the first appearance of crystallinity could be detected by Raman spectroscopy for particles made with t_{ON} = 0.5 s. Subsequent HRTEM studies of free-standing particles were performed avoiding overlap between different particles. Fig. 5.4 (a) and (b) give an overview of the NPs detected in the images and we identified particles in these regions. Detailed HRTEM studies (Fig. 5.4 (c) and (d)) show that these particles are polycrystalline. The yellow arrow in Fig. 5.4 (c) indicates the amorphous shell around the particles. Crystalline regions within a seemingly amorphous matrix (region marked in red) can be recognized, as shown in Fig. 5.4 (c). The absence of crystallinity in this matrix can have two causes: either the matrix is indeed amorphous or, alternatively, the matrix consists of (nano)crystals of which the majority is not aligned to any main crystallographic axis that would allow for lattice fringe imaging. In order to investigate further, we acquired HRTEM images for a series of sample orientations w.r.t. the electron beam.

The HRTEM image of the same single particle imaged at a sample tilt angle of a = 5^0 is shown in Fig. 5.4 (d). This image confirms the second hypothesis discussed above: the particle contains crystalline regions with different orientations which cannot be seen in a single HRTEM image. Fringes are only visible when the electron beam is aligned to the crystallographic planes. In Fig. 5.4 (c), the region marked in red seems to be amorphous. However for other orientations of the particle w.r.t. the electron beam, this region appears to be crystalline (Fig. 5.4 (d)). It should be mentioned that, although different grains appear at different positions within the NP while rotating, it cannot be excluded that the particle does contain some amorphous sub-volumes. This is because of the fact that TEM is a projection technique. Comparison of FFT patterns of selected regions within the particle studied did not yield any basic symmetry relations (such as twin-relations) between individual crystalline parts of the particle, suggesting a polycrystalline nature of randomly oriented domains. A part of the particle (region marked in white) in Fig. 5.4 (c) is overlapping with yet another particle in the projection. This area was excluded from FFT studies. On the other hand, the evidence presented here does not exclude that the different crystalline areas are correlated by a more complex system of planar defects that did not show up in the studies we performed.

Very limited papers have reported polycrystalline Si particles formation in the gas phase. According to the literature, two kinds of crystalline structures (single domain and two-domain structures) have been produced by pulsed plasmas in the gas phase [136]. While most clusters (> 99%) have single domain, a very small fraction of particles have two domains unlike our case, where a majority of NPs has more than two domains. Si nanoclusters produced in a magnetron sputtering, inert gas condensation cluster beam source also shows polycrystalline silicon structure [137].

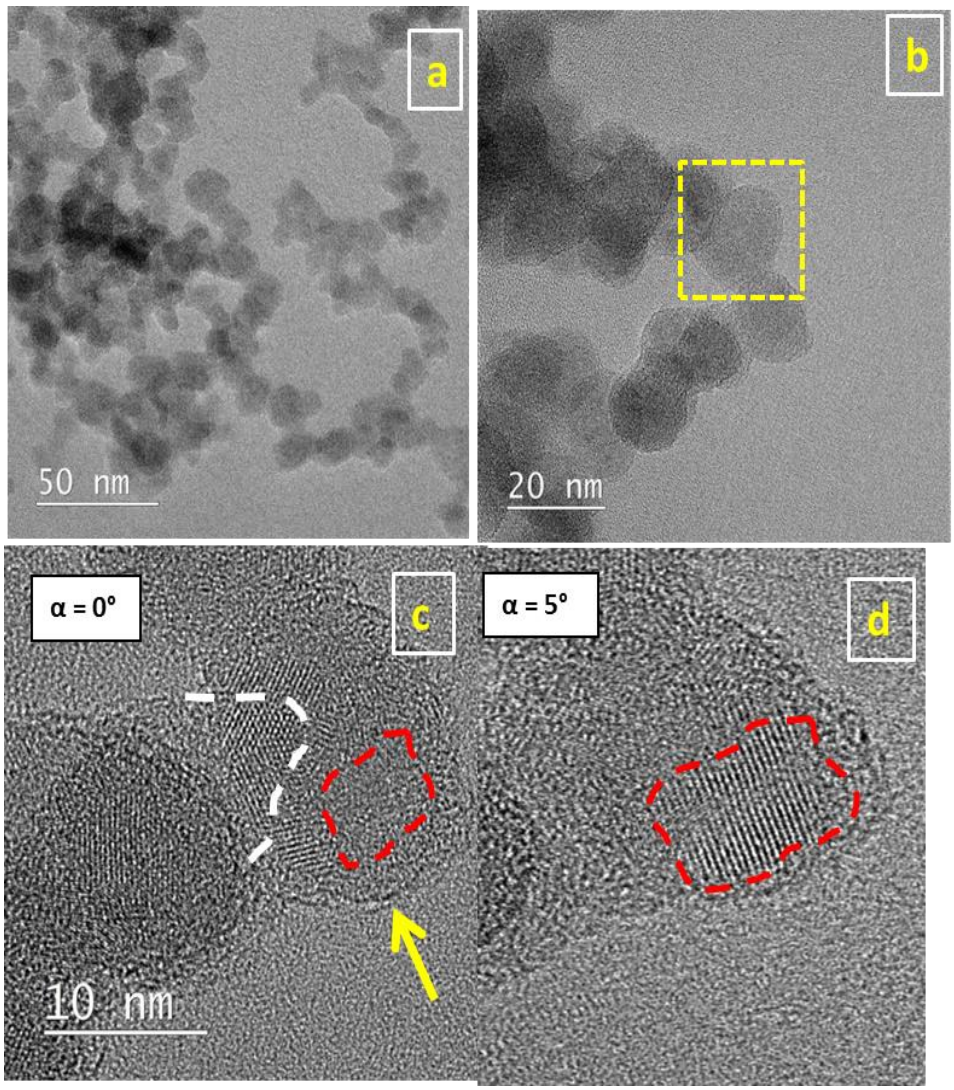

Fig. 5.4: (a) Overview of clustered NPs (b) Inset indicates our selected region of single NP studied at different tilt angles α (0^0 and 5^0) w.r.t. the incoming electron beam as shown in (c) and (d) respectively. The region marked in red indicates amorphous nature (in (c)), however at a different orientation, the same region is found to have crystallites (in (d)).

FFT patterns of NPs shown in Fig. 5.4 (e) are given in Fig. 5.4 (f) and are presented here to indicate the care required to interpret this type of image. The FFT patterns corresponding to the boxed areas are displayed on the right. The center FFT pattern is a superposition of periodicities from two individual crystals that largely overlap in this projected image. In the two encircled areas, parts of the individual crystals can be discerned (the upper FFT pattern represents the symmetry of one of the two crystals). The FFT pattern from the lower green boxed area does not display a simple symmetry relation to those of the other crystals. Thus, this analysis suggests that these areas represent three individual crystals within the same nanoparticle. A few other particles in an adjacent region were also checked using FFT pattern comparisons, and similar results were obtained. It appears that even the small particles display a complex poly-crystalline structure, which could possibly be formed by the presence of many (different) crystal defects.

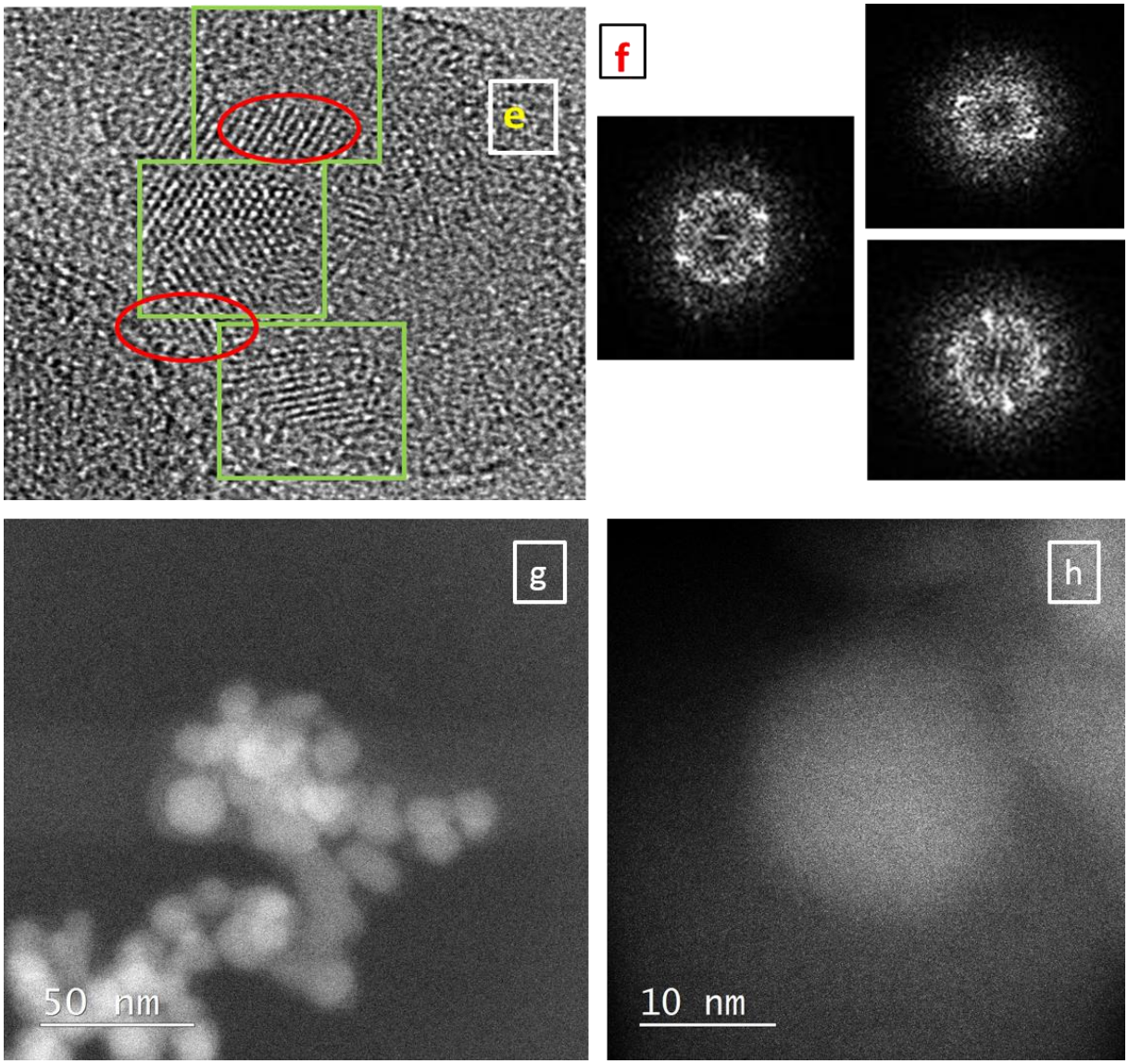

Fig. 5.4 (e) Three selected areas indicated by the squared boxes obtained from the HRTEM image of 5.4 (c). The center FFT pattern is a superposition of 2 FFT patterns, originating from the 2 encircled areas. The corresponding FFT patterns from the boxed areas are displayed in (f) thus giving an indication that these areas could represent 3 individual crystals. HAADF-STEM images (g) and (h) although severely contaminated by oxygen plasma etch confirm that voids or inclusions are not present.

Inclusions of less dense material and/or material of different compositions or voids can be detected using high angular annular dark field – scanning transmission electron microscopy (HAADF-STEM) imaging. The HAADF detector uses the electrons scattered over large angles for imaging. The HAADF detector is therefore mass sensitive, which means that higher brightness in the image corresponds to the presence of (a larger concentration of) heavier atoms and vice versa. Even though the samples are contaminated severely by the

oxygen plasma etch, from the HAADF-STEM images (Fig. 5.4 (g) and (h)) of our polycrystalline particles it was seen that neither voids nor inclusions are present inside a single particle.

5.3.2.2 HRTEM of particles produced at t_{ON} = 2 s (Phase II)

NPs produced at t_{ON} of 2 s are clusters of spherical particles, which show their poly-crystalline nature more clearly. The domain size of the single-crystalline areas within each particle is significantly larger than in phase I (Fig. 5.5).

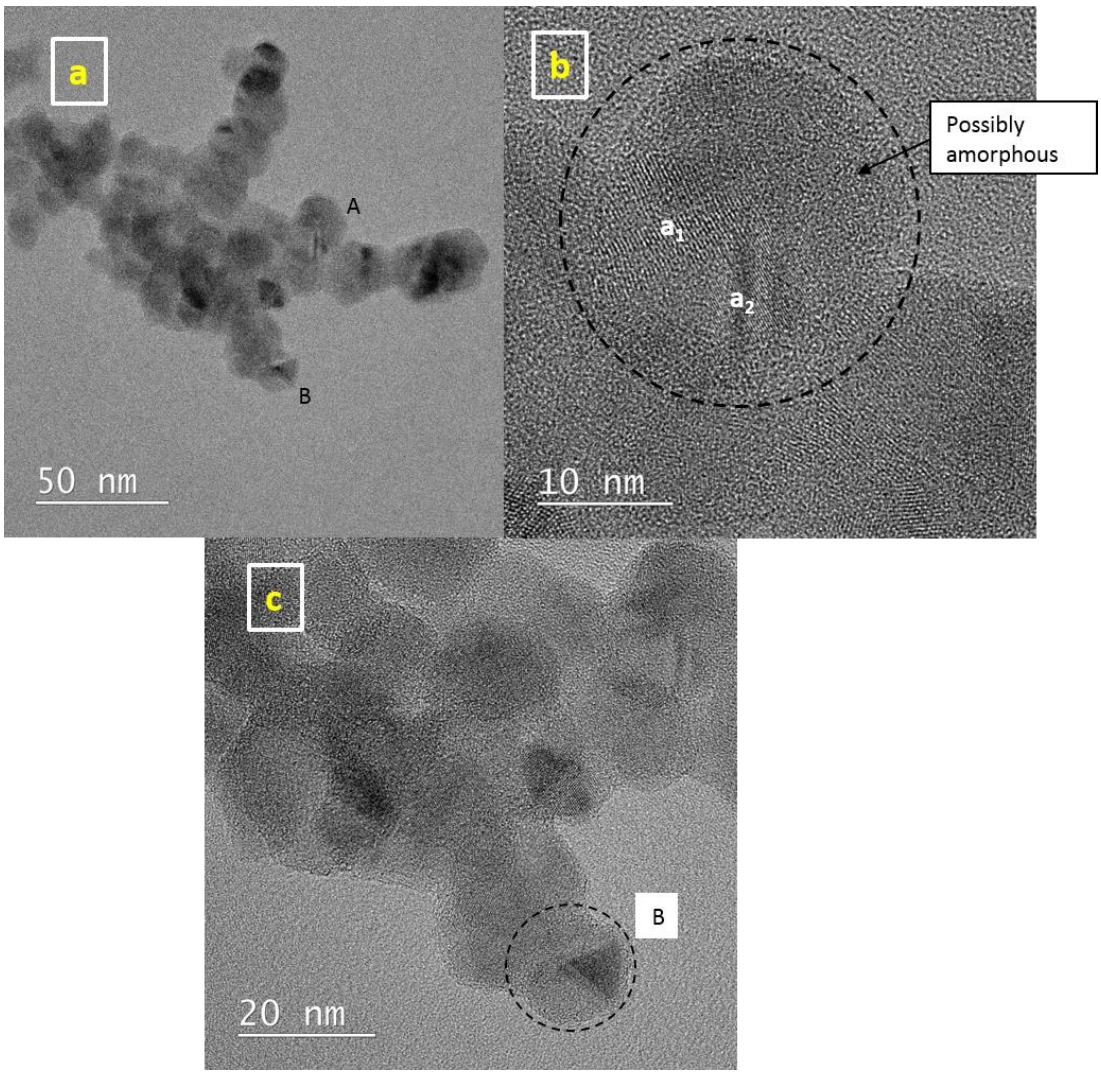

Fig 5.5 (a) Overview of NPs formed in phase II, (b) and (c) HRTEM image of particles in two regions A and B respectively; the particles found at B clearly includes a wedge shaped domain.

An example of this larger domain size is the wedge-shaped domain visible in (Fig. 5.5 (c)). This increase in domain size is the beginning of a transition to cauliflower shaped particles, as will be discussed below. The (at least two) crystalline regions in particle A (marked with a_1 and a_2) have the same crystallographic orientation. This correlation is

slightly masked by the fact that this particle has partial overlap with another particle. The vertical darker and brighter lines at the position of ''a_2" are Moiré interference fringes [138] because of this partial overlap. The Moiré fringes have a larger spacing than the lattice fringes themselves – their interspacing strongly depending on the difference in orientation between the two grains – and thus are already visible at a magnification lower than that used for HRTEM imaging.

5.3.2.2 HRTEM of particles produced at t_{ON} = 4 s (Phase III)

For longer t_{ON}, the dominant particles are the cauliflower shaped ones as shown in Fig. 5.6 (a). From t_{ON} = 4 s to 60 s in a pulsed SiH_4/Ar plasma and in continuous plasmas we observe the appearance of cauliflower-type particles. Further HRTEM studies reveal some of their interesting structural characteristics. Fig. 5.6 (b) and (c) display imaging data of cauliflower particles acquired in HAADF-STEM and HRTEM modes, respectively. The dark lines (in HAADF-STEM) between the 'branches' of the cauliflower confirm that less material (like voids) or less dense material (like SiO_x) is present here. We interpret the dark lines as being 'crevices' which extend inwards from the surface of the cauliflower. In order to interpret this structure according to the agglomeration model, we would have to assume that, in this case, three individual particles have stuck together. However, it will be a large coincidence that they fit together so perfectly with straight interfaces. In addition, the cauliflower particles display a shape with a recognizable core. We thus do not consider this cauliflower particle to be the result of 3 particles having become connected in a later stage of the growth process.

The FFT pattern in Fig. 5.6 (d) corresponding to the HRTEM image of Fig. 5.6 (c) displays the polycrystalline nature of the entire particle. In order to study the orientation relations between the different branches of the particle, selected area FFT patterns were constructed and analyzed. The right half of the particle in Fig. 5.6 (e) seems to consist of roughly two crystalline regions (a_1, a_2). Fig. 5.6 (f), (g) and (h) display the corresponding selected area FFT images of the areas indicated by the green boxes.

All three FFT patterns are [011] zone axis patterns. The dashed lines in the FFT patterns are guides to the eye. In all three FFT images, these lines have the same orientation, indicating the orientation of one set of {111} planes. Patterns a_1 and a_2 are identical, proving that areas a_1 and a_2 are symmetrically equivalent, implying that they will have originated from the same nucleus. The transition area $a_{1\text{-}2}$ shows an FFT pattern characteristic of a twinned region. On both sides of this 'transition region', the crystallographic orientation is the same. The alignment of the dark and brighter stripes in the transition region to the lattice planes in the image implies that these lines are in fact diffraction contrast variations of a series of twin domains in this transition area, similar to e.g. the multiple twinned structures in [139]. On the other hand, area a_3, forming the left part of the cauliflower, is a

polycrystalline area having orientations (not shown here) that could not simply be correlated to the orientation of areas a_1 and a_2.

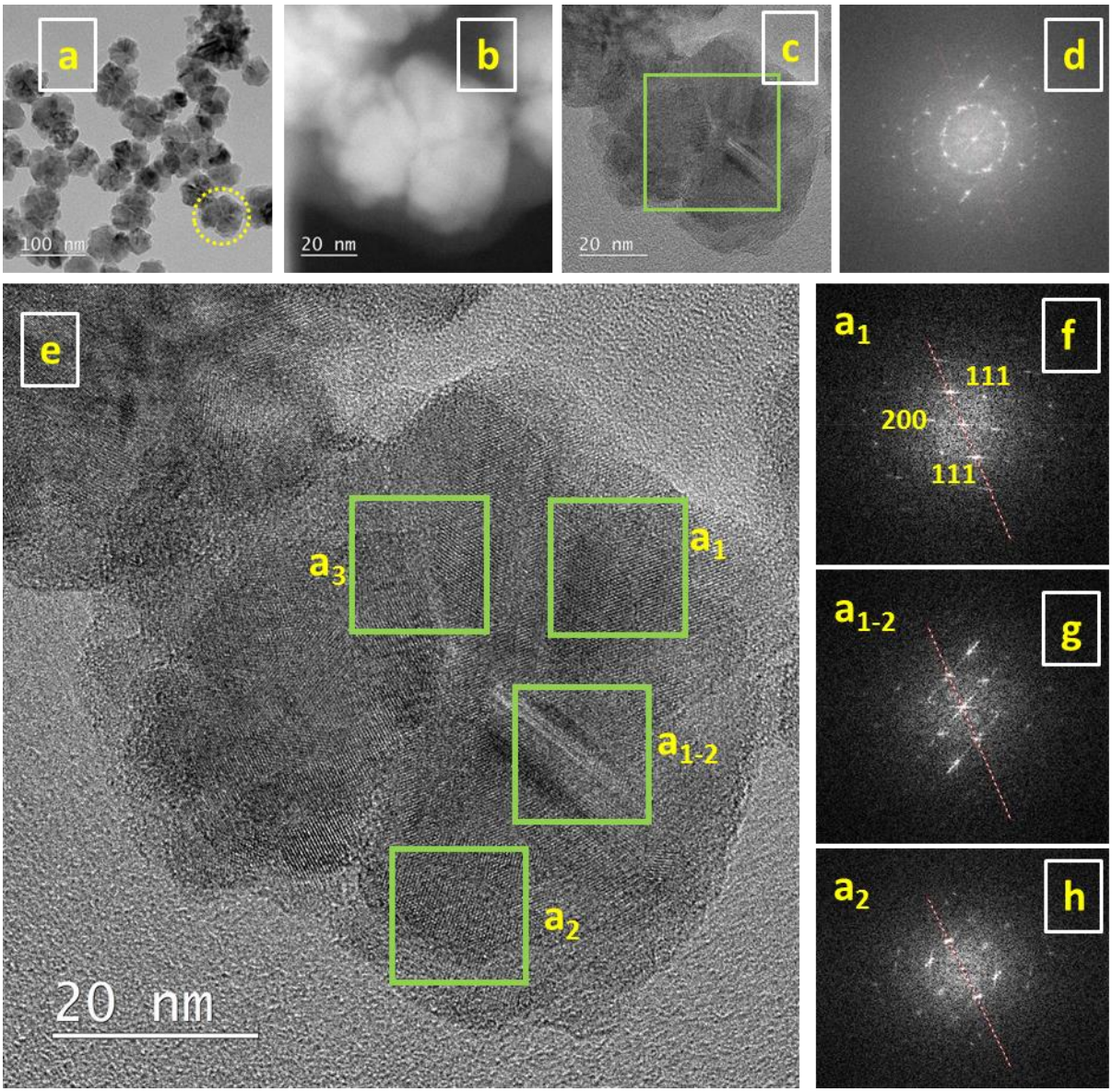

Fig. 5.6 (a) Overview of cauliflower shaped nanoparticles; (b) and (c) HAADF STEM and HRTEM image of highlighted cauliflower particle respectively, (d) FFT patterns of the center of the particle covering area a_1, a_2 and a_3, (e) HRTEM image of the highlighted particle with its 3 crystalline regions a_1, a_2 and a_3, (f), (g) and (h) FFT pattern of regions a_1, a_{1-2} and a_2 respectively.

It is possible that the particles discussed here originate from a single nucleus. As stated above, regions a_1 and a_2 are crystallographically related. What can be noticed from the images is that the twin boundaries in both regions start in the center of the particle and run outwards. It is known (from e.g. silver halide crystal growth) that the direction parallel to a twin boundary can be a fast-growing crystal direction, due to the so-called re-entrant

corner effect [140]. The existence of these boundaries in the primary nucleus might thus introduce fast growing ‘‘branches” on the primary crystal which are shown in Fig 5.7.

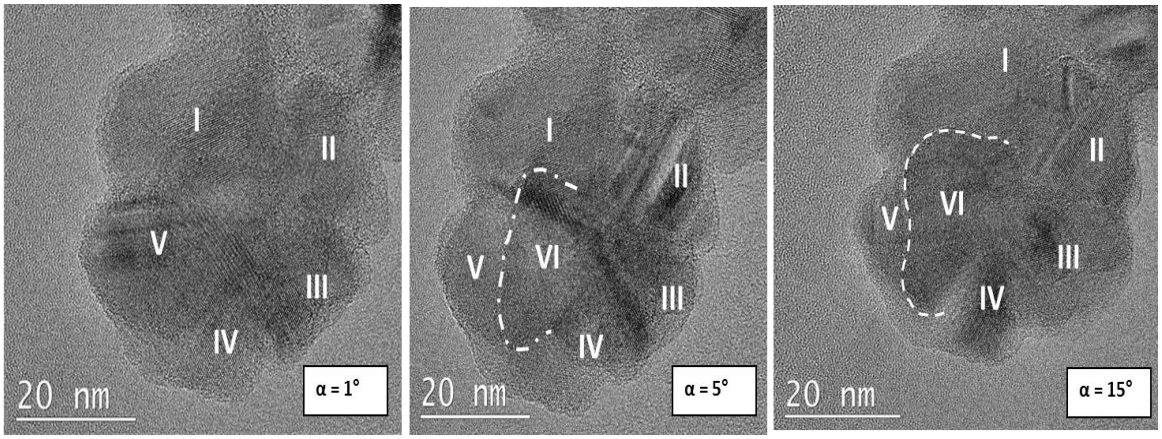

Fig. 5.7: HRTEM image of cauliflower particles obtained at different tilt angles. At lower tilt angles five branches are seen, at larger angles and at under-focus a 3-dimensional structure is revealed with a sixth branch (dashed line) which is not in the same plane as the other branches.

Fig. 5.7 displays a second type of particle that has a more compact morphology. HRTEM images were collected at sample tilts from 1^0 to 15^0 in steps of 2.5^0 as indicated in Fig. 5.7. Although only images of tilting series obtained for one sample are shown here, these studies were performed on four different particles and the same trend was observed for all series. At low tilt angles it appears as if this particle has only four branches. Upon closer inspection five branches can be discerned and after further tilting (at least) six branches were revealed. Upon tilting and adding some defocus showed a 3-D structure and revealed that these six branches are not present in the same plane. Especially the one discovered for a = 15^0 (dashed line) appears to be pointing out of the plane in which the other branches are present. Such a 3-D structure may severely hamper crystallinity studies as branches are overlapping in the projected images for most of the tilt range available to orient the particle w.r.t. the electron beam. FFT-studies of the non-overlapping parts revealed that not all branches have a simple (i.e. identical or single-twinned) crystallographic relation to each other. Therefore it can neither be confirmed nor excluded that this particle originated from a single nucleus.

5.3.3 Discussion

It is known that nanoparticle heating is the mechanism behind nanoparticle crystallization [141], and this can be used to understand our observation of the increase in crystalline fraction with increase in t_{ON}, an effect that can be explained due to better plasma power coupling at longer t_{ON} which leads to higher electron density and more surface reactions.

The effect of higher electron density at higher t_{ON} here is related to the transient nature of the initial rise of power coupled to the plasma, mainly caused by the capacitive response of instruments. The rise time has been observed by time resolved OES signal and plasma current (oscilloscope). Although a pulsed plasma offers intriguing possibilities, it presents significant challenge in controlling power delivery systems such as maintaining pulsed power regulation under rapidly changing impedance conditions. These issues make active impedance matching using traditional matching network almost impossible [142]. In line with these observations, we observe slower power matching for particles grown in phase I. The power coupling remains suboptimal for the most part of short t_{ON} and it only exponentially reaches to its delivered power. This is an inherent limitation of the VHF power source and matching network used. Thus for a short t_{ON} a stable plasma with optimum value of coupled power is not reached unlike the plasma obtained for higher t_{ON}. A higher power thus delivered at longer t_{ON}, leads to higher electron density which aids in particle heating resulting in a higher fraction of crystalline particles [143].

Also there is an increase in surface related reactions at increased $t_{ON,}$ Crystallization of NPs in the plasma occurs through energy released by energetic exothermic reactions on their surface including electron-ion recombination and atomic hydrogen induced reactions. An increase in plasma power density leads to an increase in the density of species involved in these surface reactions including electrons, ions and atomic hydrogen radicals [144]. Thus increasing plasma power results in a significant increase in particle heating, creating particles with higher crystallinity. Detailed explanation can be in found in our earlier reference [135].

The combination of suboptimal power coupling at shorter t_{ON} and a higher power causes higher crystalline fraction of particles, reinforces our observation that a higher power thus delivered at longer t_{ON}, leads to higher electron density which aids in particle heating resulting in a higher crystalline fraction of particles.

The dominant contribution to particle heating as deduced from energy balance has shown to be from recombination processes of free electrons and ions at the particle surface which acts as the heat source for crystallization of the particle. Another contribution to particle heating comes from the recombination of dissociated hydrogen (abstraction reaction) at the surface of the particle [145]. Most particulates are expected to be negatively charged and trapped in the discharge during the entire t_{ON} time, so the longer the t_{ON}, the higher is the probability of the recombination processes (free electron and ions and abstraction reactions) at the particle surface and the higher the crystallinity of the particle. This study shows that t_{ON} not only controls the particle size, but also its crystallinity.

The three phases in the growth of NPs have been discussed using HRTEM images and FFT studies. The particles formed at the beginning of phase I are composed of branched networks of particles with sizes of a few nm that can be attributed to polymerization, which as discussed above are mostly amorphous. The beginning of crystallinity sets in at the end of phase I and these particles display a polycrystalline nature. Comparison of FFT patterns of

selected regions within the particle did not yield any basic symmetry relations between individual crystallites of the particle. We hypothesize that the complex polycrystalline particle originates from a single nucleus and the gas phase species are subsequently added to this growing nucleus. When it becomes energetically more favorable for the formation of a new nucleus or crystal defect on the growing surface, another crystalline domain starts. A new nucleus is formed on the surface of the growing particle and local-epitaxial growth continues, enabling the formation of multiple domains. This could be one possible explanation for the observation of randomly oriented multiple nanostructures.

It is very important to note that most of the single-crystalline domains observed at t_{ON} = 4 s are bigger than the single crystalline regions in the smaller poly-crystalline particles produced at t_{ON} = 500 ms (Fig. 5.4 (c) and 5.6 (e)). For example, in the sample produced at t_{ON} = 500 ms typical crystalline regions of 4-5 nm are found with exceptions of 2 or 9 nm, and in the samples produced at t_{ON} = 4 s such single crystalline regions have dimensions of typically 13-16 nm with exceptions of 11 and 22 nm. The late phase I particles are thought to be the precursors of the phase II particles. This means that if the cauliflowers are formed by local epitaxy from the existing polycrystalline nanostructure, a longer t_{ON} would facilitate more particle heating resulting in epitaxial growth of the domains, hence larger crystalline areas in the NP.

We do not invoke the bulk particle temperature to explain epitaxial growth. According to the proposed nc-Si growth model, epitaxy is local in nature, the whole particle need not be in thermal equilibrium. Analogy is the nc-Si growth on a substrate in a PECVD process, where once nucleation takes place, local epitaxial growth on the crystal surface takes place [146] even though the substrate (bulk film) is kept at ~ 200^0C, which is much too low for epitaxy. Hence, in our hypothesis, the surface heating leads to local epitaxy. The second point is that the radiative cooling is considered negligible compared to conductive cooling for nanoparticles. The conductive cooling depends on the background pressure and it is reported that at low pressures in mbar range (as in our case), particle heating can build up in time [16] due to low conduction loss (net energy gain). The slow conductive cooling at low pressures allows the particle temperature to increase as a cumulative result of successive surface heating events and heat accumulates as time progresses.

Similarly other plasma processes [34] attribute the growth of larger crystalline particles to subsequent surface growth of the particle in an epitaxial manner once a crystalline nucleus of a few nanometers diameter is formed.

Larger particles have higher cross section for various recombination events to occur on their surface. The particles gain energy from the kinetic energy of electrons and ions, from their recombination and from reactive processes like association of atoms at the particle surface. Energy loss occurs via conduction and radiation. This energy balance will determine if there is net heating. According to simulations referred to in Kortshagen's review article [16], even particles in the range of 1 μm show net heating (temperature higher than

gas temperature). Larger crystals have shown to have a lower cooling rate [137]. As crystallization is a stochastic process, slower cooling provides longer times for a phase transition to take place, as the NCs stay longer at the crystallization temperature. Hence for particles in phase III the combination of slower cooling and a larger surface area - facilitating more ion-electron recombination reactions and absorption of kinetic energy of impinging ions on their surface - leads to bigger crystalline particles. For instance for a 50 nm particle in a plasma (at a pressure of 1 Pa, T_e = 3.4 eV) the average energy of the impinging ions on the surface of the particle estimated by PIC/MCC simulations is 7.5 eV [147].

For the polycrystalline growth leading to cauliflower shaped particles an alternative mechanism could be proposed. This initial complex polycrystalline structure could also be interpreted to originate from more than one nucleus instead of being the result of different crystalline areas correlated by a complex system of planar defects that did not show up in the studies we performed. The simultaneous growth of multiple seeds to obtain a final nano-polycrystalline structure has been shown both experimentally and with simulations [137]. Topological analysis reveals the positions of different seeds of crystallinity. In the above mentioned report, for a 9 nm particle, at least 3 individual crystallites are identified that grow separately from several nuclei of random shapes. Although from the evidence provided here, the single nucleus hypothesis seems most likely, we cannot rule out that the cauliflower shaped NPs could be formed by coalescence of more than one nucleus.

At longer t_{ON}, the resultant NPs could also be formed by agglomeration of smaller particles. These smaller particles must have become more crystalline during the process, as the temperature on particle rises with increased t_{ON}. The temperature is high enough for the defects (dislocations, slip planes, twin boundaries, etc.) to anneal out, allowing for an alignment of the domains. It has been demonstrated that the temperature on the surface of 10 nm particles can reach up to 1200 K [124] and this range of temperatures would suffice for subsequent growth of crystalline regions in our case to form the ‘‘branches” of the cauliflower.

The HAADF image showing polycrystalline growth from a single nucleus is one example where the classic growth model of coagulation does not apply. We however cannot claim single-point branching from all the other particles. We are aware of the other possibilities such as coalescence of different ‘‘branches” of the cauliflower particles as indicated by [114] or coagulation between oppositely charged particulates which oscillate in the electric field of the plasma to form larger particles [148]. The leaves of our cauliflower nanoparticles could also have (separately) originated in similar regions of the plasma, which could have coagulated later. Molecular dynamic simulations have found that formation of new chemical bonds during the coalescence of two particles release energy and therefore significantly increase the particle temperature [149]. Simulations have also shown that coalescence consists of two steps, initially adhesion of two particles and relocations of surface atoms near the adhesion region which happens due to the existence of H atoms on

the surface of the coalescing pair. The second step depends on the surface tension and diffusivity of the particle. Interestingly the hydrogen passivation layer was found to remain on the surface of coalescing pair of the particles during the entire coalescence event [131]. As we do not have an exact estimate of the temperature of our particles or their heating rate, we cannot rule out coalescence.

From the above arguments we may state that, if the starting material already shows a complex poly-crystalline structure as a result of many crystalline defects, then the one nucleus theory for the formation of cauliflower structure is possible. If, on the other hand, very small monocrystalline particles form agglomerates, the same structure as observed here is still possible. However, the absence of any voids or less dense regions in phase I between the multiple domains strengthen our one nucleus hypothesis compared with agglomeration. Also in contrast to [131] we do not see the H-passivation boundaries, which strengthens the claim that it is growth, not coalescence or agglomeration. Another experimental observation that strengthens our one nucleus hypothesis is the morphology of the resultant structure. HAADF images clearly indicate a center from which these branches of the cauliflower emerge out.

5.4 Nanoparticle properties by varying t_{OFF}

In this section we vary t_{OFF}, hence change the density of growth precursors, to control NP size and size distribution.

5.4.1 Experimental details

For the particles studied in this section, we have used SiH_4 and H_2 flows of 2 and 25 sccm, respectively, at a process pressure of 0.8 mbar. An input power of 140 W was used to ignite and sustain the plasma in the continuous mode. For consistency, impedance matching of the capacitors and optimization to couple maximum power was done in the continuous mode. The power and matching parameters of t_{ON} were taken from the continuous mode for each gas flow condition. Depositions are done keeping all the parameters constant with a constant t_{ON} of 25 ms and a series of t_{OFF}. We use a square wave modulation (SQWM) of the RF power. The plasma OFF time varying from shorter to longer than the residence time of the gases in the plasma are studied. The plasma OFF time used are 30 ms, 100 ms, 250 ms, 500 ms (< t_{RES}); 1 s (~ t_{RES}); 2 s and 10 s (> t_{RES}).

The particles collected on the Corning (Eagle XG) glass substrate were dispersed in ethanol and drop casted on carbon grids. Top view TEM images were taken by FEI Technai 10 operated at 100 keV. The plasma emission during deposition was monitored through a view port by a Hamamatsu H5783-04 photomultiplier (PMT) tube. Total emission in the range

200-800 nm was recorded to obtain a strong signal. The time resolved optical emission spectrum (TROES) was measured by Tektronix TDS5104B digital oscilloscope.

5.4.2 TEM studies of NPs at various t_{OFF}

The schematic representation of various cases of deposition and the characteristics of the particles are summarized in Fig. 5.8. TEM images of the collected particles are given in Fig. 5.9 (a) to (d). Fig. 5.9 (a) shows multiple sized Si nanoparticles; they comprise of cauliflower-like structures and complex structured aggregates of different sizes. Our hypothesis is that the formation of particles of varied shapes and sizes is because of the fact that the t_{OFF} times are very small and the particles formed in one cycle remain in the volume where the discharge runs and act as growth sites for the next t_{ON}. This process continues for multiple cycles before the particles escape the discharge area due to thermophoretic effect. For t_{OFF} in the range of 250 to 500 ms, multiple sized particles are formed but the majority of the particles has two distinct sizes: large spherical particles (50 nm) and aggregates of smaller particles (10-15 nm) (Fig. 5.9 (b)).

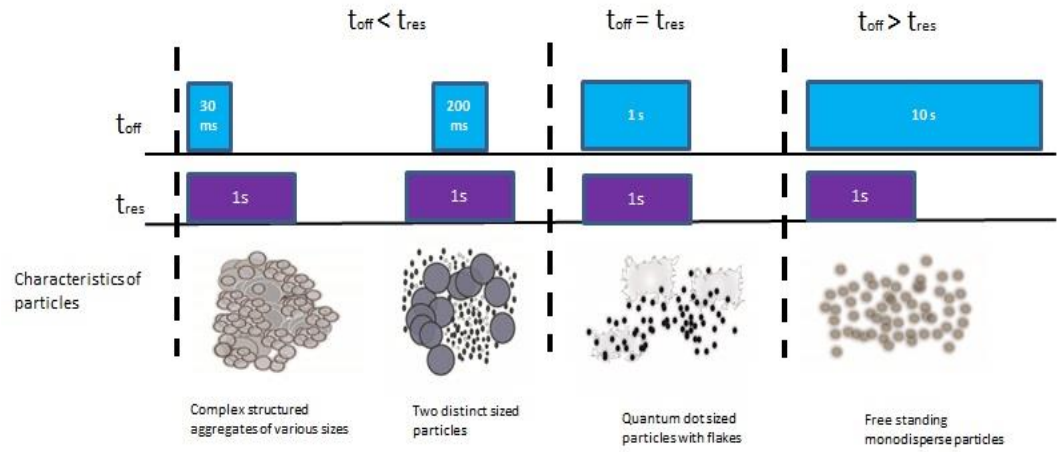

Fig. 5.8: Schematic representation of the characteristics of particles produced for different t_{OFF}.

Interestingly, for t_{OFF} in the order of t_{RES}, only free standing monodisperse particles with sizes 2-4 nm are produced (Fig. 5.9 (c)). Most of these NPs created in the gas phase are found in the vicinity or embedded in flakes of amorphous silicon due to the layer growth on the substrate. For comparison, also a longer t_{OFF} of 10 s was tried, but then only flakes were obtained. For completeness, a longer t_{ON} of 50 ms was tried with the t_{OFF} of 10 s. In this case, free standing monodisperse particles with a mean size of 11 nm were obtained with some silicon flakes (Fig. 5.9 (d)).

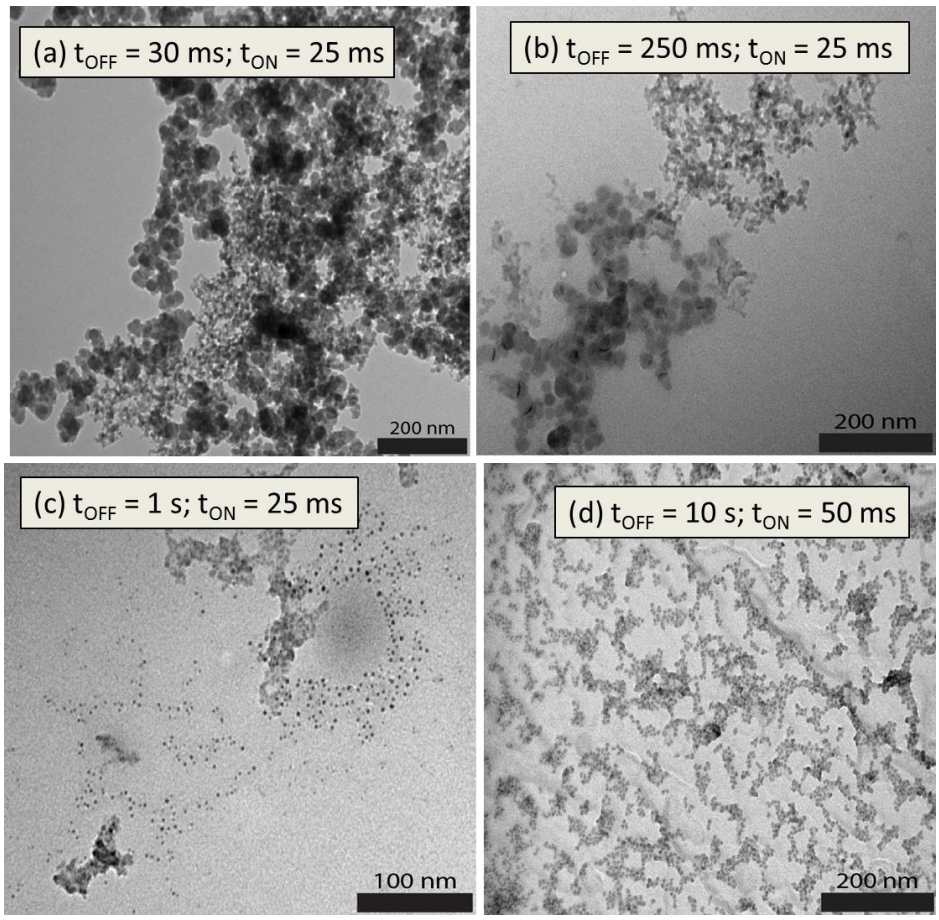

Fig. 5.9: TEM images of Si nanoparticles and flakes with different t_{OFF} time mentioned, keeping a constant plasma t_{ON}.

Nanocrystalline silicon QDs have been prepared by S. Oda et al [150] with a narrow size distribution of 1 nm by separating nucleation and growth processes by a H_2 gas pulse in a SiH_4 plasma. The residence time is a critical parameter in determining whether the NPs will grow as amorphous or crystalline particles; a longer residence time is favorable for the formation of crystalline particles and a shorter residence time leads to a large fraction of particles becoming amorphous [34]. Using SiH_4 + H_2 discharges in the pulsed mode, nanocrystals embedded in amorphous silicon thin films with photo- and dark conductivity characteristics ranging from a-Si:H to µc-Si films have been obtained [32]. Moreover, with the H_2 gas pulsing technique [32], Si nano-crystallites with a mean size of 1.7 nm and 0.4 nm standard deviation were fabricated. Size control of silicon nanocrystals has been demonstrated by varying t_{ON}. As a consequence the photoluminescence spectrum of the nanocrystals is tuned from 712 to 556 nm by varying t_{ON} from 50 to 25 ms [33].

The new information from this study is that t_{OFF} is an equally important parameter that determines the type of particles produced if no H_2 gas pulse is used to separate the growth cycles. This study infers that when t_{OFF} is small, some particles which are not pumped out of the reactor stay between the electrodes and their growth continues for several pulses. This situation is overcome for longer t_{OFF} periods, which allow the source gas to be

refreshed and the precursors of one growth cycle to be pumped away. Although the deposition times are longer, this presents a clear advantage with regard to particle size and homogeneity.

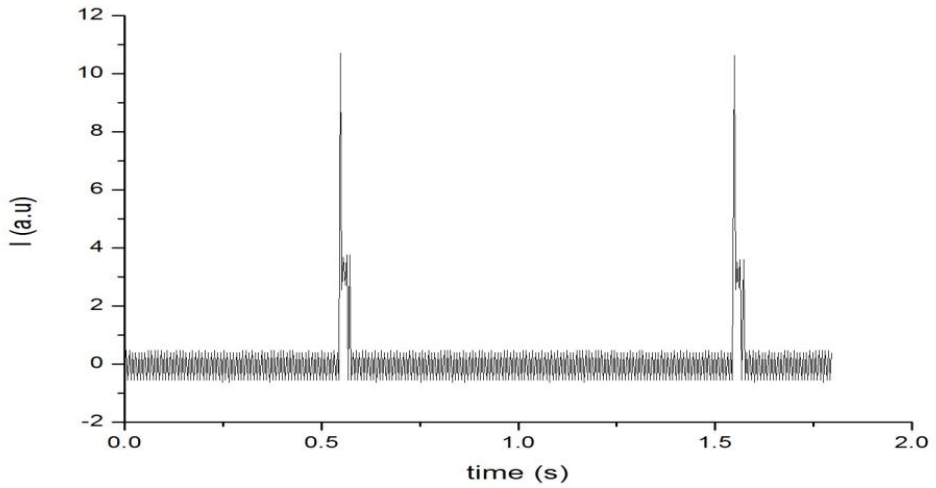

Fig 5.10 (a): OES showing a sharp peak in intensity at the start of each pulse.

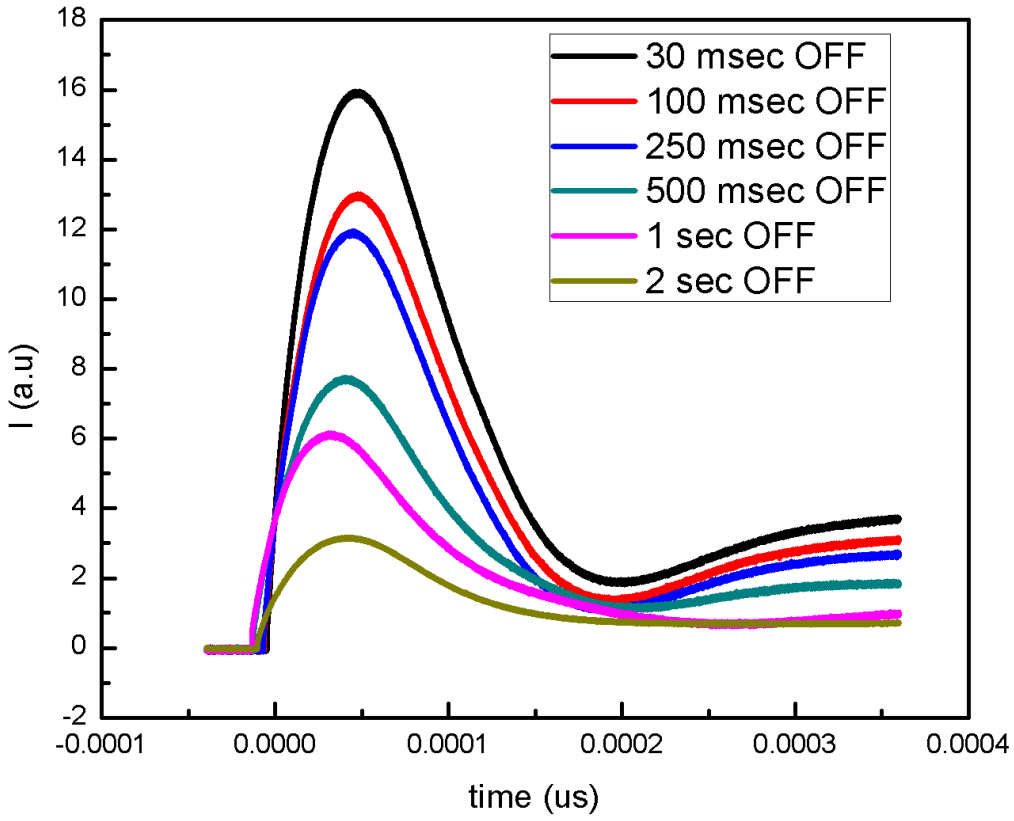

Fig. 5.10 (b): TROES at different t_{OFF} for plasma ON time of 25 ms.

Another advantage of having longer t_{OFF} is that during the OFF time, the plasma sheath disappears and the negatively formed nanoparticles during the plasma ON which are electrostatically trapped in the reactor can escape [129].

TROES studies show that, at the start of each modulation pulse (Fig. 5.10 (a)), a sharp peak in light intensity is observed, caused by heating of electrons at the onset of the pulse [132]. Fig. 5.10 (b) shows that for shorter t_{OFF}, this OES intensity peak is higher and broader than for longer t_{OFF} times. The higher light intensity can be attributed to a larger number of hot electrons resulting in higher number of radicals, leading to larger particle sizes and higher deposition rate, complying with our TEM studies.

5.5 Conclusion

Three phases of particle growth have been identified as a function of t_{ON}. By changing t_{ON} both the size and crystallinity of the particles can be controlled. After gas phase reactions, we obtain nano-polycrystalline structures which we hypothesize originate from one nucleus in phase I. These poly-crystalline structures act as seeds for the growth of spherical particles in phase II. Cauliflower shaped particles appear at longer t_{ON}, in phase III. Some ‘‘branches” of the cauliflower are crystallographically related to each other and we propose that they are formed from polycrystalline NPs in phase I. Although agglomeration of ‘‘branches” to the cauliflower structure cannot be ruled out, due to the absence of voids, it is more likely that they originate from the single nucleus of the particle formed in phase I.

Different t_{OFF} times are used to study pulsed plasmas and the growth of silicon NPs in them. It is demonstrated that when t_{OFF} is less than the gas residence time it leads to the growth of complex multi-sized nanostructures. The use of $t_{OFF} \geq t_{RES}$ is highly beneficial and leads to quantum dot sized monodisperse particles. TROES studies confirmed that the number of hot electrons and the resulting radicals at the onset of plasma are strongly dependent on the t_{OFF}.

Chapter 6: Optimizing the parameter space for increased crystallinity of Si nanoparticles§

Abstract

Various plasma process parameters such as coupled power (P), process pressure (p), gas flow and source gas ratios (SiH_4:H_2) play crucial roles in determining the size and crystallinity of the synthesized Si nanoparticles (NPs). One of the less studied parameters for NP growth in PECVD processes is the inter-electrode distance (d). This chapter focuses on the effect of d and demonstrates how a plasma reactor with larger d (refers to d = 30 mm) is a simple method to enhance the crystalline ratio of NPs produced in them compared with a standard d (refers to d = 10 mm). Increasing d or p is not strictly equivalent, and we show that for our reactor it is most effective to use pressure above 0.8 mbar at d = 30 mm to obtain purely crystalline NPs. We also establish how the larger d opens up a wider parameter space for the synthesis of crystalline Si NPs.

§ Published as
A. Mohan, R. E. I. Schropp, I. Poulios, W. J.Goedheer and J. K Rath."Optimizing the parameter space for increased crystallinity of silicon nanoparticles grown in the gas phase" *Physica Status Solidi (A)* **213** 1-5 (2016) http://doi.org/10.1016/j.cplett.2016.08.066

6.1 Parameters affecting size and crystallinity of Si nanoparticles

Silicon nanocrystals (NC) produced by PECVD (plasma enhanced chemical vapor deposition) have demonstrated very promising properties for optoelectronics devices. Most of the conventional semiconductor technology is based on crystalline Si which is not the best material for optical devices, due to the indirect nature of its band gap. However, modification of the material has made it possible for instance as porous Si based light emitting devices integrated into microelectronics devices [109]. Light emitting diodes (LED) have also been fabricated with Si NCs produced in different techniques and visible electroluminescence (EL) have been observed from these LEDs at room temperature [151] [152].

It is known that when nanoparticles (NPs) are amorphous they possess unacceptably high defect density and charge carrier trap states in the bulk which are detrimental for their utilization in optical and electronic devices, making the fabrication of crystalline particles indispensable [141]. Amorphous nanoparticles (a-NPs) usually exhibit no luminescence while for crystalline nanoparticles (c-NPs), the photoluminescence quantum yield increases with increasing crystallinity [143]. Some PL in amorphous silicon nanoclusters in silicon oxide and silicon nitride matrices is observed due to quantum confinement, but the presence of higher non-radiative recombination centers lowers emission intensity and efficiency than those for nanocrystalline particles [153]. Recently, using microplasma at a low gas temperature it has been possible though to incorporate hydrogen in the core of amorphous NPs, i.e. a-Si:H QDs, that resulted in enhanced PL with peak positions tuned by particle size [154]. In the present study, we confine our depositions to conventional parallel plate reactors.

The quality and size of Si NPs as produced in gas phase PECVD can be tuned by varying the parameters such as gas flow and process pressure *p*, thus, varying the residence time (τ) or by pulsing the plasma. A longer τ is favorable for obtaining crystalline particles and a short τ leads to an increasing fraction of amorphous particles [34]. The same reference highlights the importance of shorter τ which leads to smaller particle size with lower standard deviation, thus, achieving uniform NP size. In their experiment τ is adjusted by varying the total gas flow (Ar + SiH_4).

In an inductively coupled plasma (ICP), only the precursor gas flow (SiH_4) was found to be the most critical factor affecting the size and crystallinity of the Si NPs [155]. NP size decreased and the crystallinity increased with increasing SiH_4 flows. Increased SiH_4 flow increases, the number of dissociated Si ions, increasing the plasma density. The enhancement in crystallinity is attributed to the increased plasma density which provides sufficient energy to form a more crystalline phase. Similar trends of increased crystallinity and reduced NP size (analyzed with XRD (X-Ray diffraction)) with increasing SiH_4 flow was also found in expanding thermal plasma [24].

Similarly increasing the applied power is also shown to increase the crystallinity as confirmed by XRD and Raman spectroscopy [143]. As the NPs become larger, the plasma power required for their crystallization increases [141]. Same trend of increased crystallinity with power was observed for Si NPs synthesized in the gas phase by ICP [155]. This is because increase in power leads to significant increase in particle heating causing a transition from amorphous to crystalline NPs. However, it was also observed that too much power resulted in reduction of crystallinity, the reason for which is unknown. Similar observation of increased crystallinity for increased power for nc-Si thin films synthesize by RF-PECVD [156] and VHF PECVD [157] has been made, however, the mechanism could be very different compared to gas phase NCs.

The discharge geometry is a very important parameter as it influences the other process parameters both directly and indirectly because of their inter-dependence [158]. When the geometry of the reactor is changed by changing the electrode shapes, electrode diameter or inter-electrode distance, the sheath and the plasma potential are changed [159]. The variation of geometric characteristics of silane discharges (such as electrode shape, diameter) influences all primary (processes which occur by electron molecule collision) and secondary processes (processes involving radical-neutral and neutral-neutral reactions). Thus, the resulting modification of the gas phase composition by primary and secondary processes affects the deposition mechanism and quality of the film.

For the deposition of nc-Si films in VHF PECVD for solar cells, it is observed that, deposition rates are enhanced at larger values of inter-electrode distance (*d*) or pressure (*p*), as the electron temperature rises [160]. Moreover, when *p* or *d* is large, the collision probability between atomic hydrogen and silane molecule is large which favors abstraction reaction, enhancing radical formation and consequently the deposition rate. Systematic variation of *d* along with other parameters such as excitation power, substrate temperature, total pressure to achieve high deposition rate and silane utilization are investigated with the aim to find the optimum conditions for the deposition of p-i-n solar cells [161, 162]. The onset of powder formation in SiH_4:H_2 discharges was found to mainly depend on the *p.d* product (pressure × inter-electrode distance). Using analytical plasma chemistry model, the powder formation has shown to be reduced by using a narrow *d* [163]. All the studies reported above on the effect of *d* on other plasma parameters are limited to nc-Si thin films. Despite its obvious importance, discharge geometry and its correlation with gas phase processes have not received its due attention for the fabrication of silicon NPs in the gas phase.

The effect of *p* on the synthesis of crystalline Si NPs in plasma is not straightforward. Different trends of NP crystallinity with gas pressure are recorded in literature. Let's consider three cases. First case: In a capacitively coupled plasma, low pressure is found to be favorable for high crystalline fraction NP synthesis and both the crystal size and crystalline fraction are found to decrease with increasing pressures [164] (Fig. 6.1 (a)). In the same

reference, it is shown that the electron temperature (T_e) decreases while ion flux (T_i) remains unchanged for increasing *p*. The second case: in a non-thermal plasma, it was observed that the crystalline fraction (instead) increases with increasing pressure [165] (Fig. 6.1 (b)). This increase in crystalline fraction was due to a higher residence time, as was shown both experimentally and with computational fluid dynamics model simulations. Third case: In an ICP on the other hand, the process pressure, did not influence the particle size or crystallinity (Fig. 6.1 (c)). However, the NP production rate increased with increasing pressure [155].

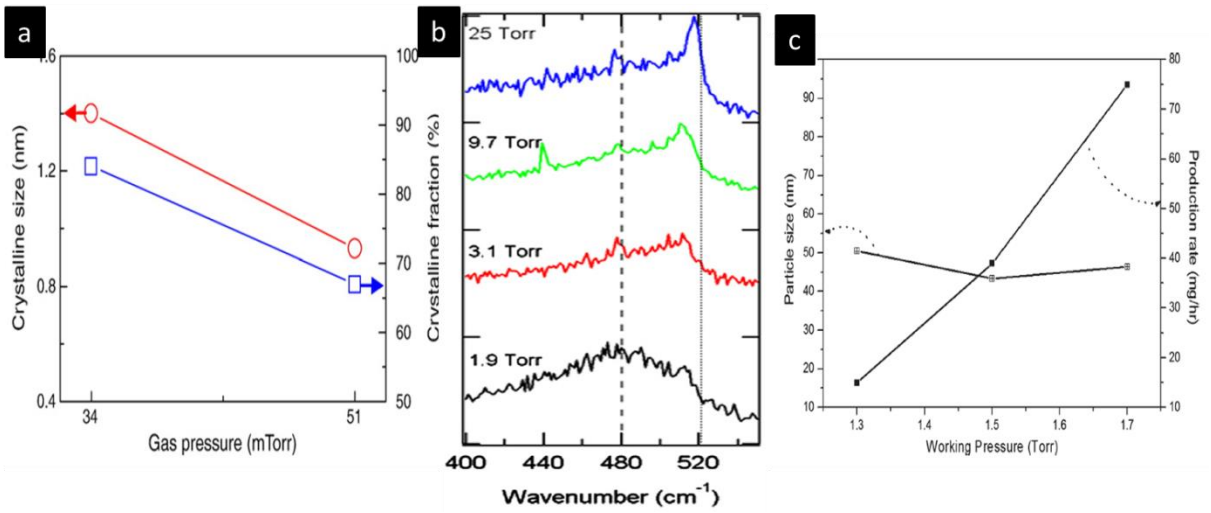

Fig. 6.1: Various trends of NP size and crystallinity with varying process pressure taken from literature. (a) taken from [164] *, (b) taken from* [165] *and (c) taken from* [155].

Although a lot of similarity in trends exists between gas phase Si NP crystallization and growth surface nc-Si thin film crystallization, for instance the increase in crystalline fraction with power for both the cases follows the same trend. However, it is noteworthy that the mechanism of NP crystallization differs (NP crystallization mechanism is highlighted in Chapter 5) and also different contributions for crystallization differ depending on the kind of plasma and the reactor geometry. It also depends on whether *d* was kept constant or *p.d* product was kept constant while changing *p*. Moreover, the absence of any consistent trends reinforces the inter-dependence of various plasma parameters on each other.

In this chapter we investigate the relationship between the various plasma parameters such as power density, pressure and inter-electrode distance on the crystallinity of the Si NPs obtained in the gas phase. One of the less studied parameters for NP growth in PECVD reactors is the inter-electrode distance. Here we discuss the optimization of parameter space to obtain an increased crystalline fraction of particles by varying *p* and *d*. We then highlight the importance of inter-electrode distance.

6.2 Geometry of the plasma reactor with varying inter-electrode distance

The NPs described in this chapter are grown in a dedicated plasma reactor (Fig. 6.2), more details of which has been described in Chapter 4. The NPs formed in the gas phase are collected at a Corning Eagle XG glass substrate mounted at the top of the reactor, behind the perforated grounded grid. Raman studies are done on as-deposited particles on the Corning substrate and some of the NPs collected are dispersed in ethanol for TEM studies.

For the particles mentioned in this chapter, a SiH_4:Ar flow ratio of 4:50 sccm was used for the growth at a series of *p* controlled by the VAT throttle value between the plasma reactor and the turbo pump. A series of forward VHF powers was applied to the bottom electrode, keeping the substrate unheated. The distance between the powered bottom electrode and the grounded grid top electrode is 10 mm which is the volume of the plasma region. This distance has been varied with additional spacers (as shown in Fig. 6.2) of 10 mm and 20 mm, effectively changing the inter-electrode distance, *d* and the volume of the plasma region. When the spacers are inserted, the bottom showerhead electrode is consequently moved further down to accommodate the spacers.

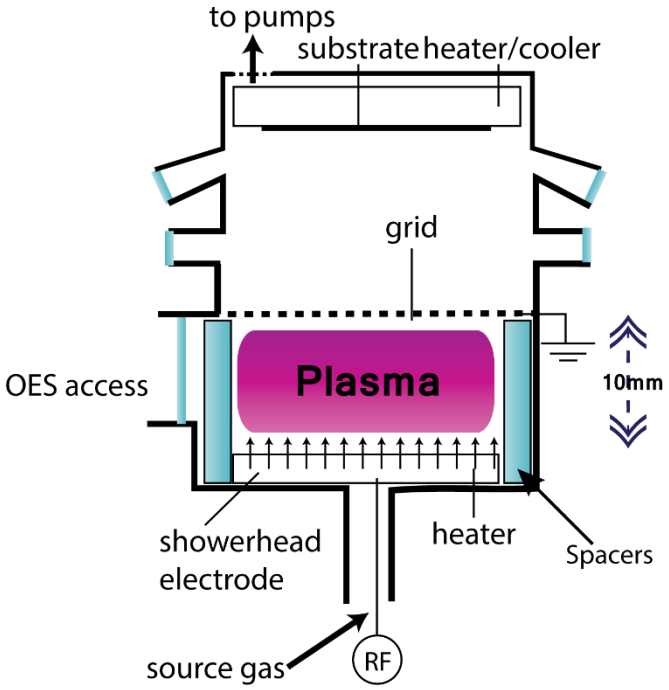

Fig. 6.2: Schematic diagram of plasma reactor with adjustable spacers to effectively change the volume of the plasma zone (x and y dimensions are not to scale).

Structural characterization of particles has been done by Tecnai 10 Transmission electron microscope (TEM). The crystalline ratio of the NPs was calculated from the Si-Si transverse optic (TO) vibrational modes in Raman spectra [74] obtained with an inVia Renishaw microscope equipped with a laser with a wavelength of 514.5 nm (More details of

the Renishaw Raman spectroscopy found in chapter 2). The laser power is fixed at a low 0.3 W mm^{-2} to ensure we do not crystallize the sample. The Raman crystalline ratio is calculated using

$$R_c = \frac{I_c + I_{gb}}{I_a + I_c + I_{gb}} \qquad \text{Eq (6.1)}$$

where I_a, I_c and I_{gb} are the intensities Si-Si TO vibration peaks corresponding to crystalline, amorphous and grain-boundary phases. The inaccuracies of R_c, depend on the value of crystallinity and an error of up to 5 % is estimated for samples with crystalline fraction greater than 85 %, however for samples with lower crystalline fraction an error of 20 % is not uncommon. The samples obtained on the Corning glass from the reactor are quite inhomogeneous and for each samples, R_c is measured at 5 spots in the Renishaw spectrometer. The average values of R_c are reported in this chapter.

6.3 Effect of applied power density, *P*

The applied power is an important parameter which determines if the resultant NPs are amorphous or crystalline. Keeping all the other parameters constant, at p = 700 µbar and d = 10 mm, we studied the change in crystallinity of the NPs for a series of power density P (*applied power/plasma volume*). The applied power is recorded at the power meter, however the actual power coupled to the plasma could be much less because of losses in the cables and matching network. For the calculation of the plasma volume, only the plasma zone between the two electrodes is considered, the radius of the cylindrical reactor being 10 cm, and height is determined by the respective spacer used.

Fig. 6.3 (a), (b) and (c) show the TEM images of the NPs produced at various P. NPs produced at 480 mW/cm^3 have the most striking features with both cauliflower shaped nanoparticles (multiple crystalline orientations) and circular particles (single crystalline orientation). However, particles produced at 160 mW/cm^3 have aggregates of amorphous particles which are dominant. The crystalline fraction found in this case is from the cauliflower shaped NPs which are present in a smaller fraction. Fig. 6.3(d) gives the Raman crystalline ratio for these NPs which increases with increasing power density. The same trend as in Fig. 6.3 (d) is observed for all studied d, at constant p.

The importance of the input power in various plasma reactors for non-thermal plasmas, inductively coupled plasmas and RF PECVD has been highlighted by several authors [143, 155, 156]. We have found the existence of a threshold power density only above which the particles are crystalline and a trend of increased crystallinity with increasing power density. This finding is in line with the observations in the above mentioned articles.

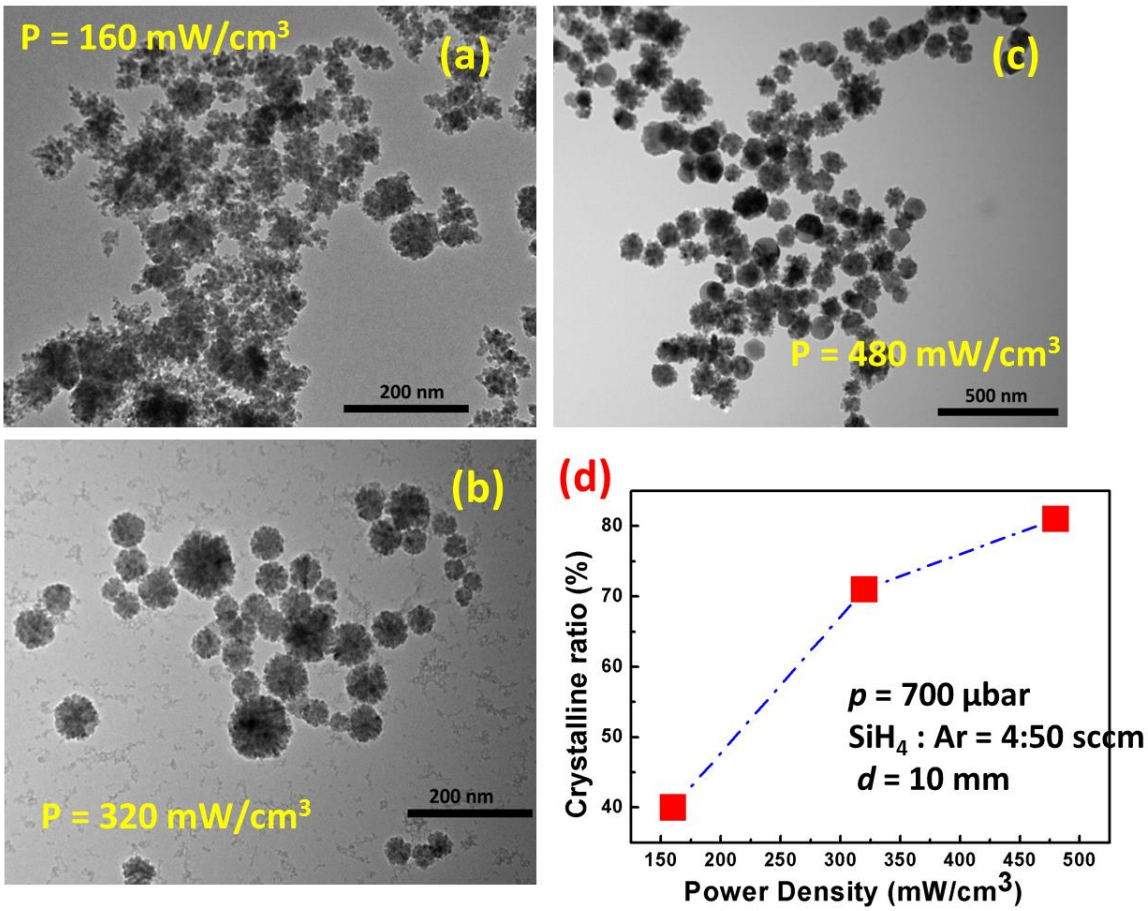

Fig. 6.3: TEM image of Si NPs produced in Ar+SiH_4 plasma at (a) P = 160 mW/cm^3 (b) P = 320 mW/cm^3 (c) P = 480 mW/cm^3 (d) Crystalline ratio of NPs at various P for a d of 10 mm.

Crystallization of NPs immersed in the plasma occurs through energy released by energetic exothermic reactions on their surface including electron-ion recombination and atomic hydrogen induced abstraction reactions. An increase in plasma power density leads to an increase in the density of species involved in these surface reactions including electrons, ions, and atomic hydrogen radicals [144]. Thus increasing plasma power results in a significant increase in particle heating, creating particles with higher crystallinity. Evidence of particle heating [166] with increasing plasma power has been reported, the effect of which is an increase of the fraction of SiH species on the particle surface, and virtually no trace of SiH_2 and SiH_3 (which are normally present in amorphous NPs) due to desorption from hot particle. The a-NPs containing higher hydrides lead to less dense particle ensembles, as can be seen for low power density NPs synthesized in our experiments, which have less dense structure compared to the compact NPs synthesized at high power density (Fig. 6.3 (a) and (c)).

6.4 Effect of inter-electrode distance, *d*

Although significant studies have been done on the effect of inter-electrode distance on the quality of nc-Si films, its effect on the formation of Si NPs in the gas phase by PECVD has received very meagre attention.

For the same power density and process pressure, the crystalline ratio increases dramatically for higher electrode distance. As seen in Fig. 6.4 (d), the crystalline ratio almost doubles when the *d* increases from 10 mm (referred to as standard *d*) to 30 mm (referred to as larger *d*). The morphology of the NPs are also significantly improved, low density polymeric chains and clustered NPs at *d* = 10 mm are replaced by compact single crystalline NPs at *d* = 30 mm as seen in Fig. 6.4 (a) to (c). The transition from amorphous aggregates to completely crystalline single particles at higher electrode distance can be attributed to higher collision probability of plasma species due to higher residence times in the plasma volume at larger *d*. This enables a higher number of ion-electron recombination events at each particle, increasing the energy available for crystallization per NP. A substantial portion of particle heating also comes from the hydrogen abstraction reaction. The likely occurrence of abstraction reactions is higher at higher *d*. An example of abstraction reaction is $SiH_4 + H \rightarrow SiH_3 + H_2$.

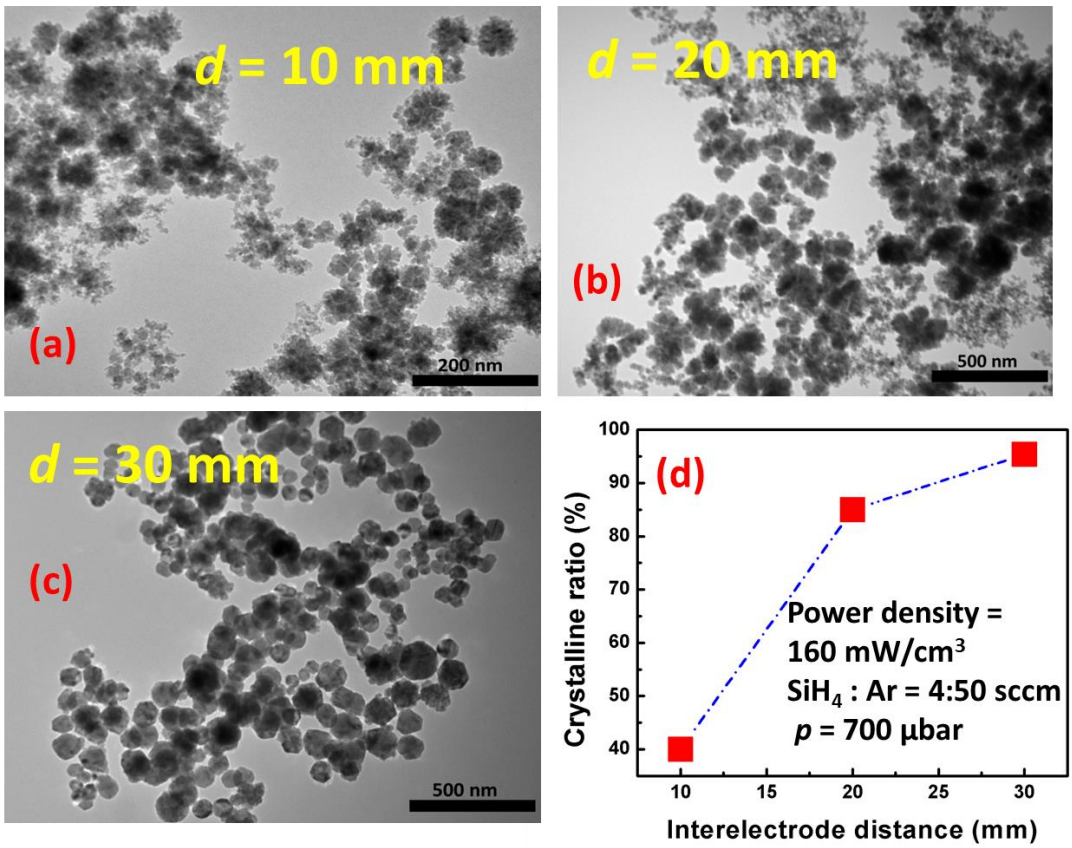

Fig. 6.4: TEM image of Si NPs produced at (a) d = 10 mm (b) d = 20 mm and (c) d = 30 mm (d) Crystalline ratio of NPs at various d.

Optical emission spectroscopy (OES) data obtained during the growth of nanocrystalline Si particles indicate lower electron temperatures at smaller *d* [155]. Greater loss of positive ions occur at smaller *d* resulting in an increased flux of electrons diffusing to the walls of the reactor, leading to a decrease in electron density [167, 168]. The inferior quality of NPs produced at lower *d*, can also be attributed to this lower electron density and electron temperature.

6.5 Effect of process pressure, *p*

The process pressure in the reactor plays a crucial role in determining if the resultant NPs are amorphous or crystalline. For smaller *d* (10 mm), the particles are predominantly amorphous, except at high pressures. Thus, we report the variation of crystalline ratio at larger *d* (30 mm) (Fig. 6.5). The particles produced at 50 µbar consist of both circular amorphous particles and cauliflower shaped particles with a small crystalline ratio (Fig. 6.6 (a)). It is interesting to note that as the pressure gets higher, the number of cauliflower particles reduces and the single crystalline circular particles increase in number, and hence also the crystallinity of the whole sample (Fig. 6.6 (d)).

Similar to *d*, a higher process pressure leads to a higher residence time in the plasma volume if the gas flow in sccm is kept constant, which results in more frequency/events of collisions with electrons/ions and hydrogen, leading to particle heating.

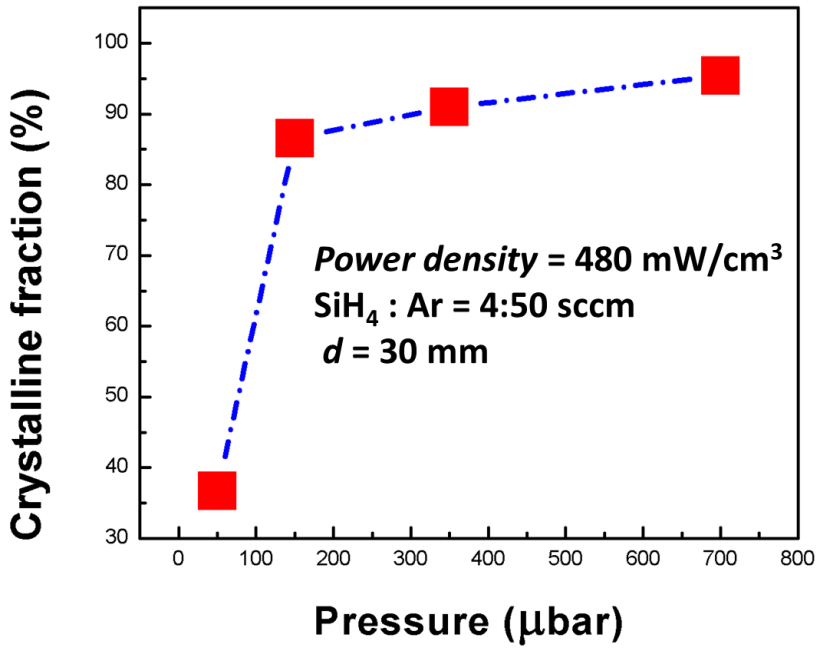

Fig 6.5: Crystalline ratio of NPs at various pressure, p.

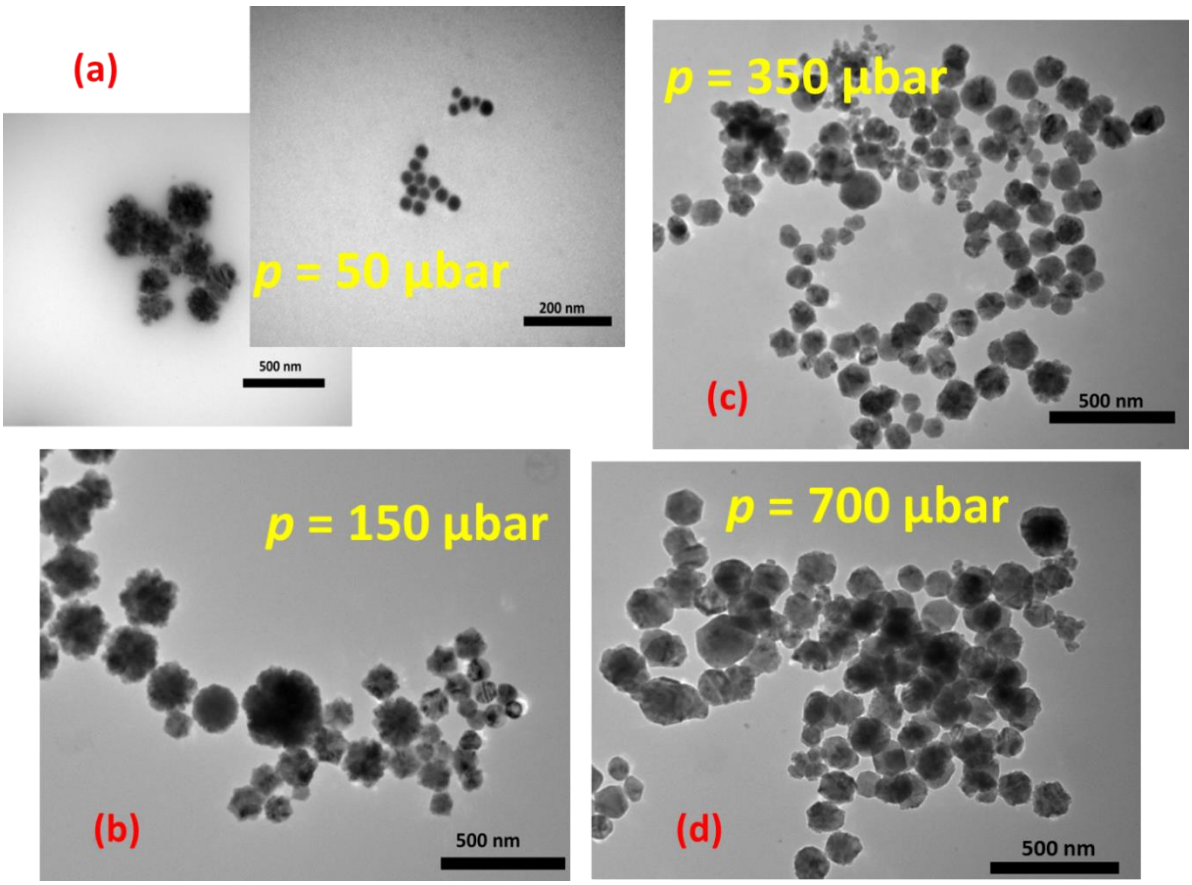

Fig. 6.6: TEM image of Si NPs produced at (a) p = 50 µbar (b) p = 150 µbar (c) p = 350 µbar (d) p = 700 µbar (d is kept at 30 mm).

6.6 Residence time and crystallinity

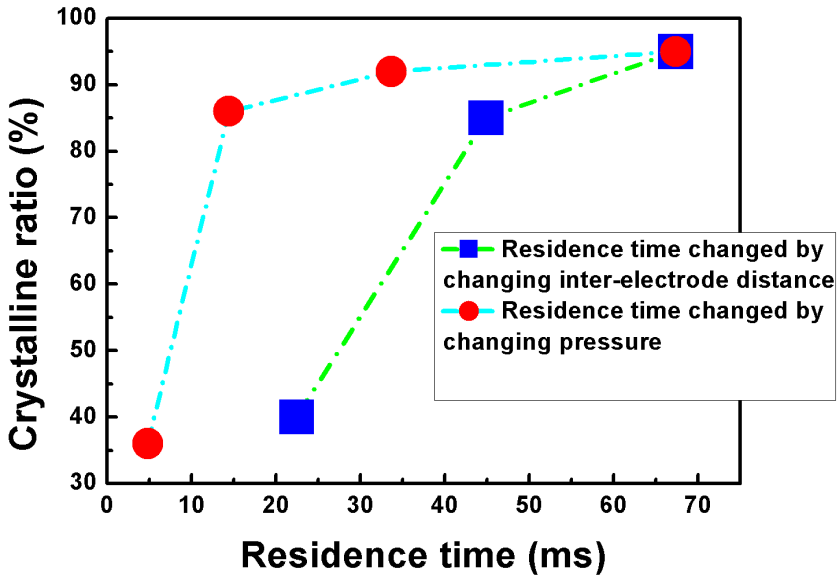

Fig. 6.7: Crystalline ratio of NPs obtained at various residence times. Residence times varied by changing p in one case and changing d in the other.

Residence time of the gases in the reactor have been varied in two ways: by changing the process pressure (for a fixed electrode distance and power density) and by changing the inter electrode distance (for a fixed pressure and power density). Comparison of both the cases clearly shows that increasing residence time is a key to increase crystallinity in the materials, irrespective of the methods (Fig. 6.7). However, a high electrode distance has a beneficial effect, because in that case the crystallinity is relatively less sensitive to decrease in residence time caused by another parameter, i.e., “lower pressure”.

6.7 Overview of parametric study on crystalline fraction

We studied the entire process parameter space possible for our reactor with special focus on inter-electrode distance, *d*. This is given in Fig. 6.8. We observed that it is easier to sustain a plasma at higher *p* and *d* concurrent with observations mentioned earlier.

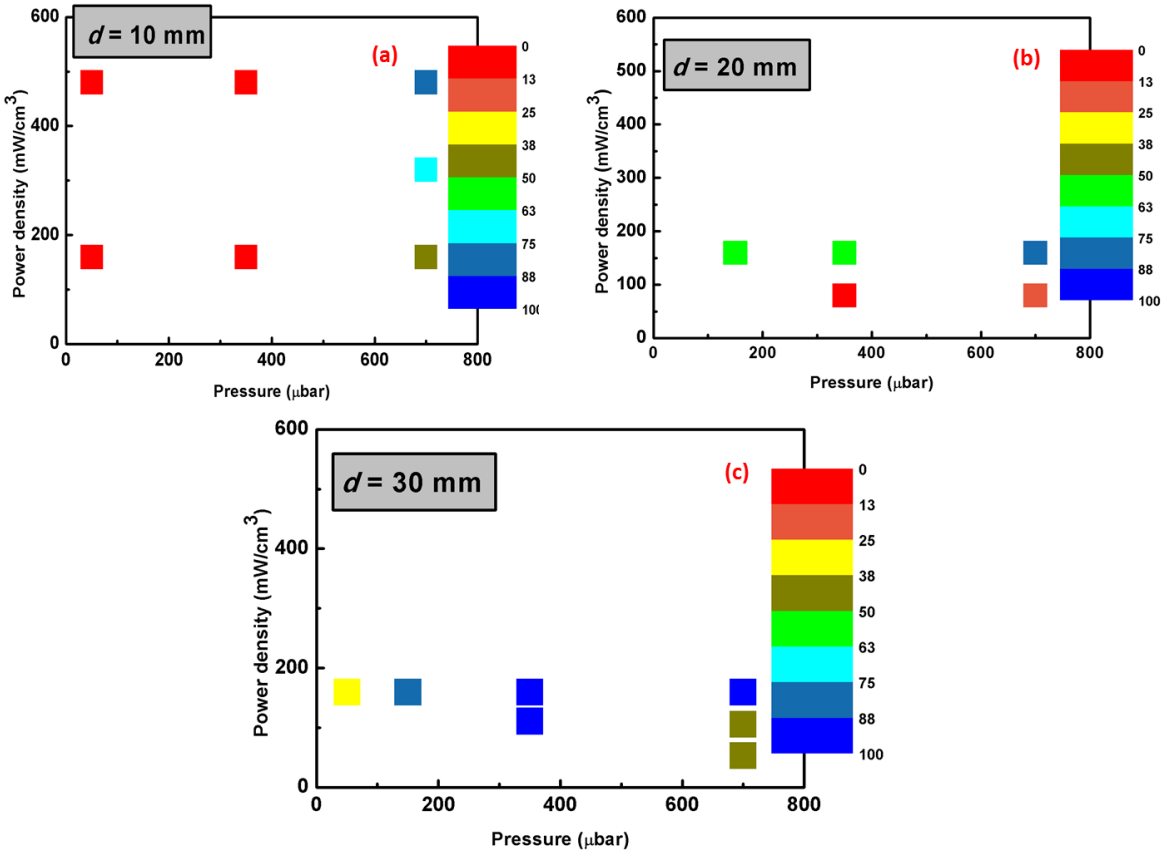

Fig. 6.8: Parametric study of crystalline ratio of NPs as a function of pressure and power density at various d. The color maps indicate the percentage (%) of crystallinity.

Fig. 6.8 clearly shows that synthesizing particles at higher *d* and/or higher *p*, presents a clear advantage in terms of higher crystalline ratio. Increasing *d* or *p* is not strictly equivalent, as higher *d* opens up a wider parameter space for the growth of crystalline NPs. For instance as seen in the Fig. 6.8, crystalline NPs can be obtained even at lower pressures

and lower power density for a higher *d* (30 mm) whereas for similar conditions only amorphous particles were produced for lower *d* (10 mm).

6.8 Conclusions

We have performed a parametric study on the synthesis of silicon nanoparticles in the gas phase in a capacitively coupled VHF discharge in terms of crystalline ratio**.** The optimum parameter space for the growth of nanoparticles with improved morphology and crystallinity is the regime of higher pressure and larger inter-electrode distance. We show here how larger electrode distance expands the parameter space for obtaining single crystalline particles even at low process pressures and powers.

Chapter 7: Gas phase grown silicon germanium nanocrystals**

Abstract

Gas phase synthesis of highly crystalline and homogeneously alloyed $Si_{1-x}Ge_x$ nanocrystals in continuous and pulsed plasmas is reported in this chapter. Nanocrystals have been produced with remarkable control over their composition by altering the precursor GeH_4 gas flow in a continuous plasma. We specially highlight that in the pulsed plasma mode, we obtain quantum-sized free standing alloy nanoparticles with a mean size of 7.3 nm. The presence of $Si_{1-x}Ge_x$ ($0 \leq x \leq 1$) alloy particles is confirmed with multiple techniques, i.e. Raman spectroscopy, XRD (X Ray diffraction) and HRTEM (high resolution transmission electron microscopy) studies, with each of these methods consistently yielding the same composition. The nanocrystals synthesized in this study have potential applications in band-gap engineering for multijunction solar cells.

** Published as
A. Mohan, F. D. Tichelaar, M. Kaiser, M. A. Verheijen, R. E. I. Schropp, J. K. Rath. Gas phase grown silicon germanium nanocrystals. *Chem. Phys. Lett.* **661** 185–190 (2016)
http://doi.org/10.1016/j.cplett.2016.08.066

7.1 Alloying of Si and Ge nanocrystals in gas phase

In order to effectively harness the desirable properties of nanocrystals (NCs) strong efforts have been made to precisely control the NC size and size distribution during particle synthesis. Currently, size control is fairly well achieved in state-of the art NC syntheses [169]. Lately, additional research activity has been devoted to NC compositional modification by either doping or alloying, which offers an additional degree of freedom to broaden the nanocrystal properties [170, 171]. Some applications require multiple characteristics in a single nanoparticle (NP) system; alloy NPs can be used to meet multiple requirements of nanoparticle size and properties. Because the optical and other properties of the alloy nanoparticles vary with composition, these properties can be tuned by modifying composition while maintaining a small size [29]. To obtain homogeneous alloys, the growth rates of the two or more constituent materials must be comparable, and the conditions necessary for the growth of one constituent material must not impede the growth of the other constituent material [172, 173].

To date, the most studied modes of SiGe alloy NCs synthesis have largely been via solid-phase nucleation and growth at high temperatures in silicon oxide [174, 175]. The process involves co-sputtering of Si, Ge and silicon dioxide targets on a silicon substrate and subsequent annealing at ~1100^0C. SiGe alloy nanoparticles have been synthesized by thermal evaporation of powders of Si and Ge on glass substrates at temperatures greater than 1400^0C [176]. Although the surrounding matrix passivates the nanoparticle surface well, it notably reduces the spectrum of potential applications and limits the possible surface treatment for the embedded particle. For instance, the poor electrical conductivity of the silicon oxide matrix seriously hinders the incorporation of this material into NC based devices [177].

Although liquid phase synthesis of SiGe alloy NCs are convenient for subsequent functionalization reactions, these techniques are usually time consuming and have very low yields and produce a wide range of sizes and shapes [178].

Gas phase processes showing convincing ability to produce SiGe alloy NCs have been performed in continuously operated two-stage hot-wall aerosol reactor setups [30]. The first hot wall reactor (HWR I) stage is used to produce Si seed particles from SiH_4 pyrolysis in Ar. The resulting seeding aerosol is fed into the second stage reactor (HWR II) and a mixture of SiH_4 and GeH_4 is added. The ratio of the precursors, their partial pressures, the synthesis temperature in the hot wall reactor, and the overall pressure are varied depending on the desired morphology and composition. Both alloy particles and faceted Ge-Si core-shell structures are obtained. The limitation of this technique is the high synthesis temperatures of 1000^0C for (HWR II), which yields only 0.5 gh^{-1}. SiGe alloy NCs are also produced by laser pyrolysis of SiH_4 and GeH_4 and subsequent colloidal dispersion in solvents upon extended

sonication without ligands, thereby providing the possibility of using them as ink to make patterned films, free of organic surfactants, compatible with device fabrication [29].

Although Si and Ge are environmentally safe, Ge is rarer and considerably more expensive than silicon, and its use is not considered viable for large scale, low cost applications. However, Si and Ge alloys are used for several specialized applications, for instance they have been used in Radioisotope Thermoelectric generators, powering NASA space crafts since 1976 [179]. Addition of germanium to a silicon lattice reduces the thermal conductivity of the material and increases the value of the dimensionless thermoelectric figure of merit (*ZT*)

$$ZT = S^2\kappa^{-1}\rho^{-1}T \qquad \text{Eq (7.1)}$$

where, *S* is the Seebeck coefficient , ρ the electrical resistivity and κ the thermal conductivity at temperature *T*.

Another approach for improving the efficiency of thermoelectric devices is the reduction of grain size [180], since phonon scattering at the grain boundaries of nanostructured materials reduces the material's thermal conductivity. Nanostructuring silicon-germanium based devices is expected to reduce the amount of Ge in the alloy [181], paving the way for large scale commercial utilization.

Reports on nanocrystal alloying are sparse, especially on alloying of Si and Ge in the gas phase to form NCs. Due to the smaller electron and hole effective masses of Ge compared to Si, the effective Bohr radius of Ge (24.3 nm) is larger than that of Si (4.9 nm) [13, 182], making quantum confinement effects more pronounced in Ge [183]. This provides an additional advantage allowing larger SiGe nanoparticles to still satisfy the quantum confinement effect, making them possible candidates for components of nanoscale functional optical devices [184]. The possibility of combining the electronic properties of Si and structural properties of Ge makes SiGe heterostructures strong candidates for optoelectronic devices that could have large impact on the future of silicon based microelectronics [10, 185]. The advantage of alloy NCs to tune the band gap by varying the composition could be exploited in quantum dot Si based tandem solar cells, in which SiGe quantum dots (QDs) can be applied as absorber layers of the bottom cell. However, the difficulty in fabricating $Si_{1-x}Ge_x$ alloy QD lies in the segregation of the two elemental phases. According to molecular dynamic studies Ge segregates to the shell leaving a Si rich core behind [185]. There are limited reports on the formation of $Si_{1-x}Ge_x$ nanocrystals with uniform composition by gas phase plasma approach [27, 28]. Here, we studied this phenomenon and achieved good control over the composition of SiGe alloy NCs.

7.2 SiGe nanoparticle synthesis and characterization

After having achieved Si QDs in very high frequency – plasma enhanced chemical vapor deposition (VHF PECVD) (Chapter 4) it is our endeavor to fabricate SiGe QDs in a similar configuration. In this chapter, we discuss the synthesis of $Si_{1-x}Ge_x$ alloy NCs in the gas phase, in the 60 MHz VHF PECVD dedicated plasma reactor using the showerhead electrode assembly, same as that used for Si QD fabrication (Chapter 4). The NCs are pulled to the substrate through a multi-hole grounded upper electrode, by a combination of the thermophoresis effect and directional gas flow facilitated by gas drag due to pumping.

In the continuous mode the NCs were synthesized at a pressure of 0.8 mbar and a VHF forward power of 150 W applied to the showerhead bottom electrode. For all parameters, the amount of reflected power was minimized to less than 5% of the input power. The substrate stage, placed behind the top multihole grounded electrode, was unheated. SiH_4+GeH_4+ Ar is used as a precursor gas mixture. The Ar flow was fixed at 50 sccm, the GeH_4 flow was varied (as given in Table 7.1) and the particle characteristics were studied. R is defined as the gas flow ratio $GeH_4/(SiH_4 + GeH_4)$.

Table 7.1: Gas flow composition used for NC synthesis in the continuous mode.

Sample ID	GeH_4 flow (sccm)	SiH_4 flow (sccm)	R (%) = $GeH_4/(SiH_4 + GeH_4)$
1	0.5	4	11.11
2	1	4	20.00
3	2	4	33.33
5	4	4	50
6	2	0	100.00

For the pulsed mode, a gas flow ratio of SiH_4:GeH_4:Ar of 4 sccm:4 sccm:50 sccm (R = 50) was used at a pressure of 0.8 mbar, and pure Ge NPs were obtained at GeH_4:Ar of 4 sccm: 50 sccm. The NPs in the pulsed mode were synthesized by modulating the applied power at t_{ON} = 100 ms and t_{OFF} = 1 s.

We characterize the synthesized samples optically and structurally with the following techniques: Raman spectroscopy (inVia Renishaw microscope equipped with a laser with a wavelength of 514.5 nm), Transmission Electron Microscopy (TEM): high angle annular dark field - scanning transmission electron microscopy (HAADF-STEM) (JEM200 ARM TEM), and energy dispersive X-ray spectrometry mapping (EDS; windowless 100 mm^2 SDD EDS

detector), and imaging using a FEI Tecnai TF20ST/STEM with a liquid nitrogen cooled EDAX EDS detector. Grazing incidence X-ray diffraction (GI XRD) (Panalytical X'Pert diffractometer) was also used. The Ge content in the NCs was calculated from Raman spectroscopy, XRD, and estimated directly by compositional analysis using TEM-EDS. The compositions obtained from these three techniques are presented.

7.3 Results and Discussion

7.3.1 Continuous plasma

In the continuous mode different fractions of agglomerated spherical and cauliflower shaped NCs are obtained with sizes ranging from 50 nm to 300 nm as revealed by TEM (Fig. 7.1 (a) and (b)). Interestingly, the domain sizes of the NCs are less than 12 nm in all cases when measured with XRD. XRD data provides line broadening at half maximum intensity (FWHM) as a function of Bragg angle after subtracting the instrumental line broadening. The mean particle size d_g can be estimated using this XRD data from the FWHM of the interference peaks $w\ (2\theta)$ at an angle $(2\theta)$with the Scherrer equation [75].

$$d_g = \frac{0.9\lambda}{w(2\theta)cos\theta} \qquad \text{Eq (7.2)}$$

A large fraction of the NCs is multicrystalline as evidenced by the HRTEM image (Fig 7.2)

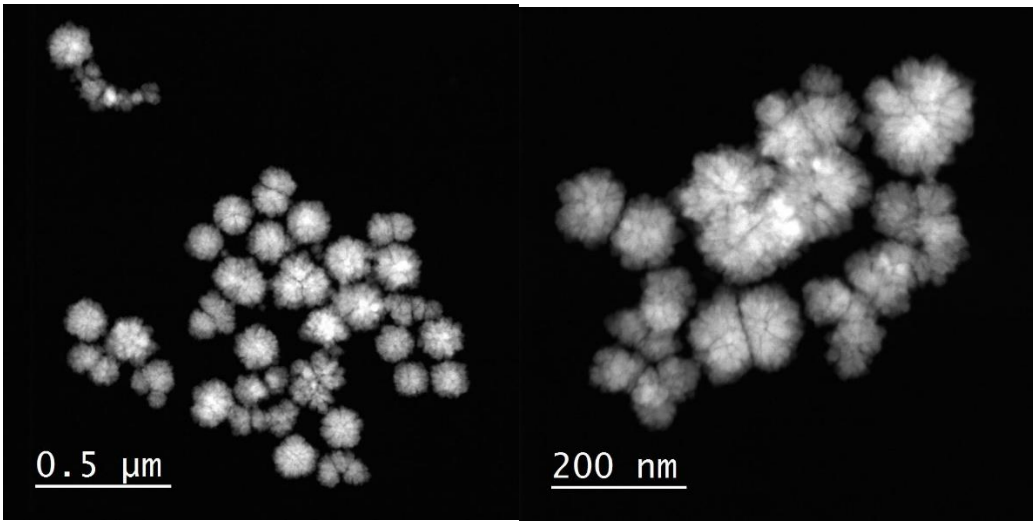

Fig.7.1 (a): Two fractions of cauliflower NPs (45 – 80 nm) and (135 – 190 nm) and twin butterfly structured NPs found in the continuous plasma (R = 11.11)

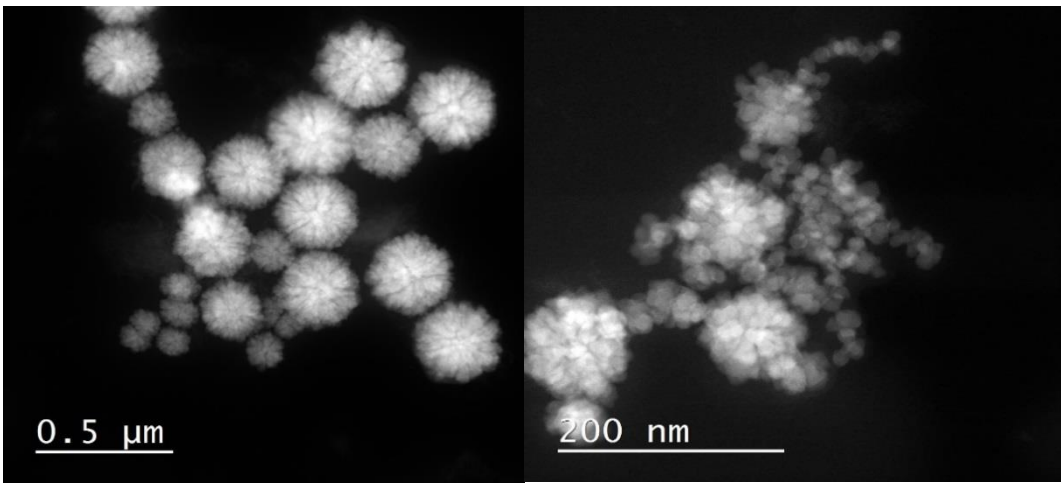

Fig. 7.1 (b): Two fractions of cauliflower NPs (100 nm) and (300 nm) and spherical NPs (10 nm) found in the continuous plasma (R = 33.33)

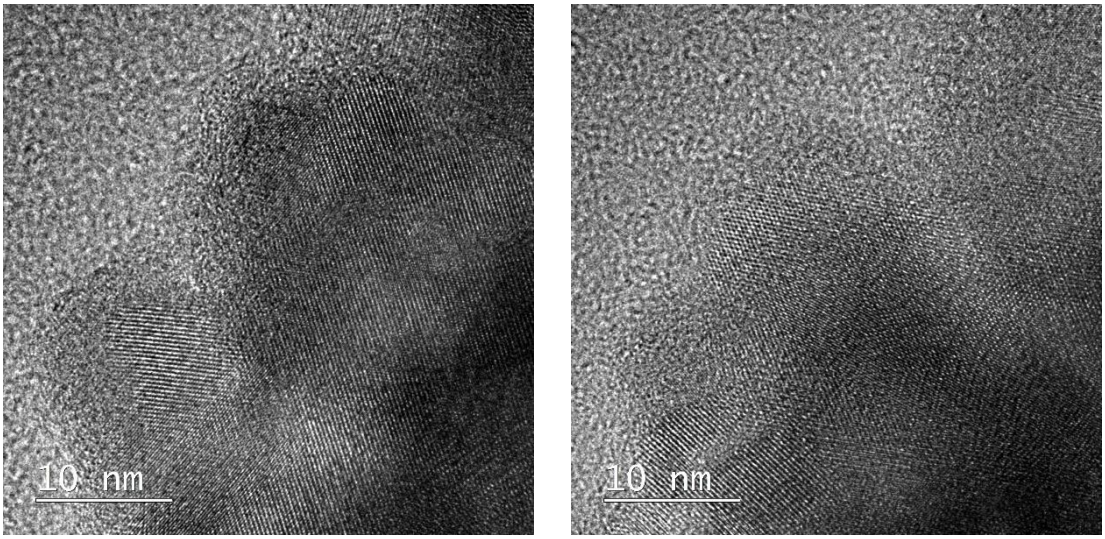

Fig. 7.2: The poly-crystalline nature of the cauliflower NPs is demonstrated by the lattice fringes in these HRTEM images.

It can be seen in Fig. 7.3 that the Ge content of the samples and hence the alloy composition can be controlled by varying the flow of GeH_4. It is also interesting to note that the different techniques consistently yield the same Ge content within the accuracy of the techniques. Details of how the values of Ge content are estimated from each technique are given in the subsequent section.

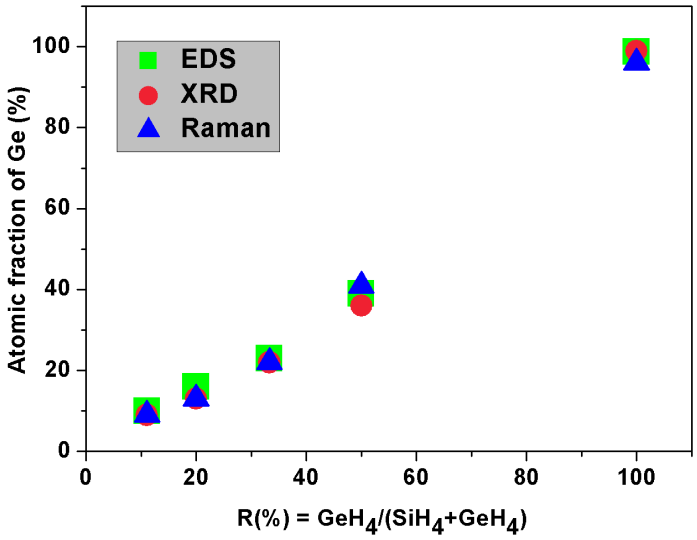

Fig. 7.3: Atomic fraction of Ge in $Si_{1-x}Ge_x$ alloy NCs estimated from TEM-EDS, XRD and Raman spectroscopy as a function of gas flow ratio R = $GeH_4/(SiH_4 + GeH_4)$.

7.3.1.1 Energy dispersive X-Ray Spectroscopy (EDS)

` Elemental analysis was performed using EDS to reveal the chemical composition of individual particles of each sample. The simultaneous acquisition of HAADF-STEM images – the contrast being sensitive to atomic number and sample thickness – allowed for revealing particle morphology as well as possible local compositional variations.

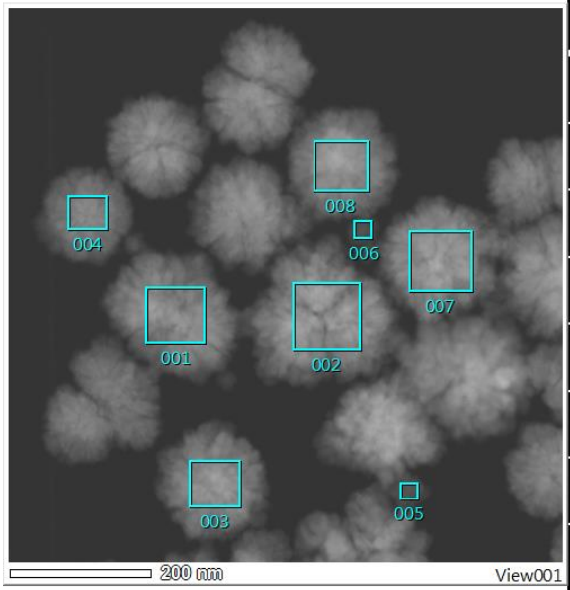

Area	Si (at%)	Ge (at%)
001	90	10
002	91	9
003	90	10
004	91	9
005	90	10
006	90	10
007	90	10
008	90	10

Fig. 7.4: HAADF image displaying a set of $Si_{1-x}Ge_x$ alloy NCs of a sample deposited with R = 11.11. EDS compositional studies were performed on 8 different particles. Table 7.2: Quantified amounts of various areas of Fig 7.4 in atomic fraction (%). It can be seen that all regions display the approximately same Si:Ge composition with a spread in composition less than 2%.

An example of how the composition was determined by TEM EDS for sample with R = 11.11 is given in Fig. 7.4 and Table 7.2. An area containing multiple NCs is selected and EDS area scans are performed on different NCs as indicated with the square boxes. It can be seen that for this sample, all regions in the particles display the same Si:Ge composition. The values that are plotted in Fig. 7.3 are obtained in a similar way for all the samples and the average value of each region is considered. The line profiles extracted from the 2-D (Fig 7.5) maps yield a flat O-signal. If the entire particle had been oxidized, the signal is expected to rise in the center of the particle (similar to Si and Ge), which is not the case, so we assume that the particles surface are oxidized post deposition.

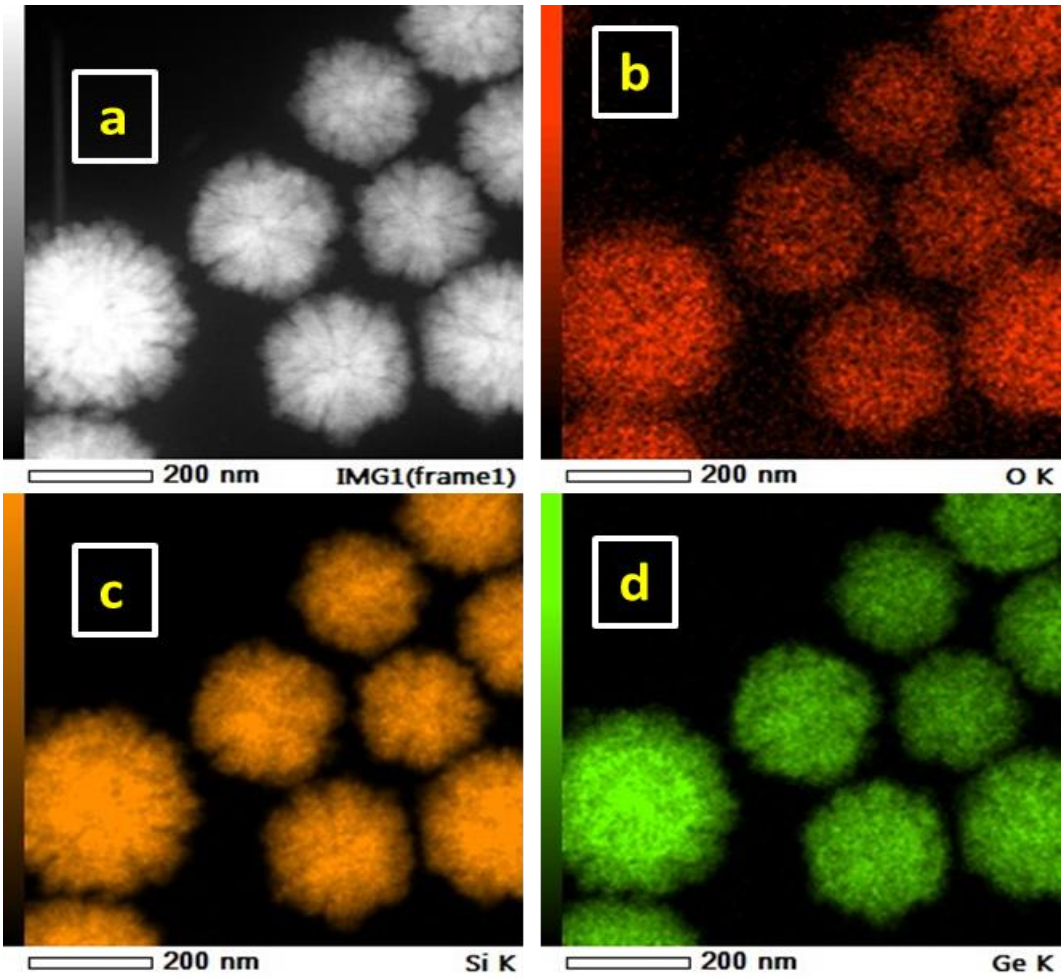

Fig. 7.5: (a) Raw EDS counts mapping of NCs with R = 20, (b) O map suggesting that the outer shells of the NC are oxidized, (c) Si mapping, (d) Ge mapping

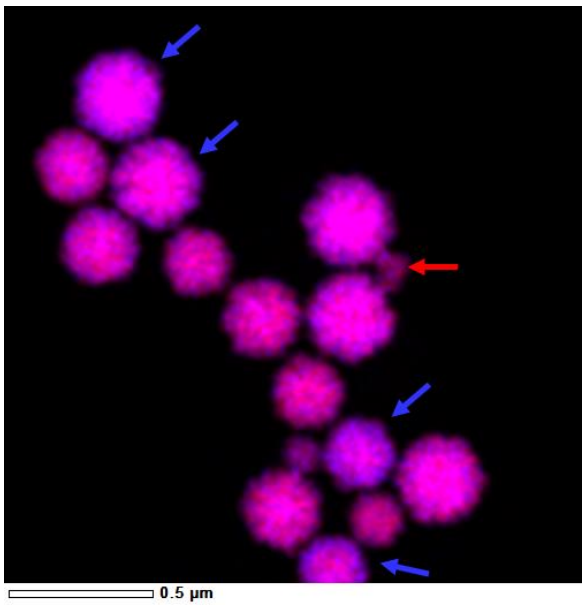

7.5 (e) overlay image; Si rich particles are given in red arrows, Ge rich particles in blue arrows and pink represents Si and Ge.

Phase segregation in $Si_{1-x}Ge_x$ alloy nanoparticles when subjected to high temperature (>1100^oC) and even formation of Ge nanoparticles from $Si_{1-x}Ge_x$ alloy matrix has been observed in literature [186]. This is explained by the existence of a driving force (due to the larger size, Ge atoms would induce local strains inside the structure), thus it would be energetically more favorable for Ge atoms to segregate on the surface of the nanocrystal. Ge segregation has also been predicted by molecular dynamics simulations [187]. Germanium diffusion to the shell in order to minimize the dangling bonds has been observed in simulation in the case of hydrogen free nanoclusters [185]. The phase separation is attributed to differences in atomic size, surface energy, and surface diffusion disparity between Si and Ge, leading to inhomogeneous structures, which are more stable and energetically more favorable than homogeneous structures. *However, our EDS studies clearly show that most of the NCs found with various flow ratios of SiH_4 and GeH_4 contain a homogenous alloy of Si and Ge throughout the NCs which have a cauliflower morphology. This is a significant new finding.* Between different NCs no Si:Ge concentration variations are observed in a run as evidenced in Fig. 7.4, Table 7.2 and Fig. 7.5.

There are also some compositional variations (<10%) for each R. The figures of the spread in composition are given in Fig. 7.6 and table 7.3. However, the majority as mentioned above has a homogeneous distribution of Si and Ge across each NC.

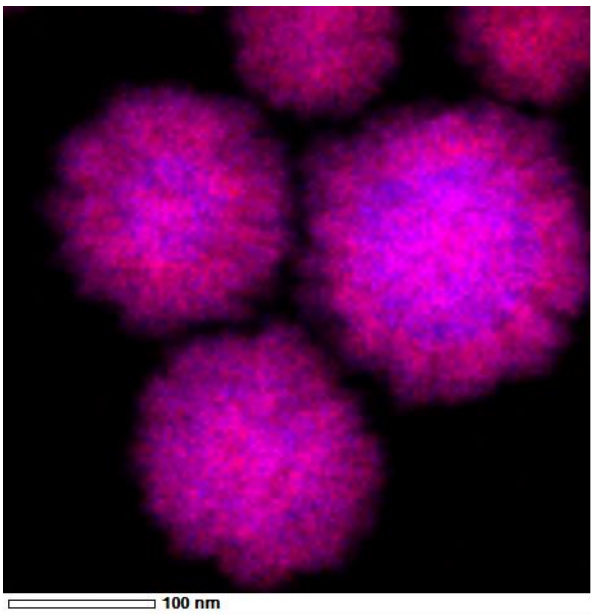

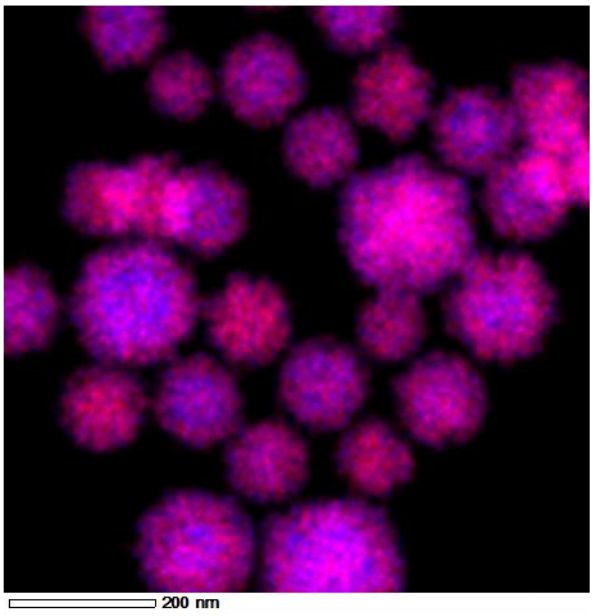

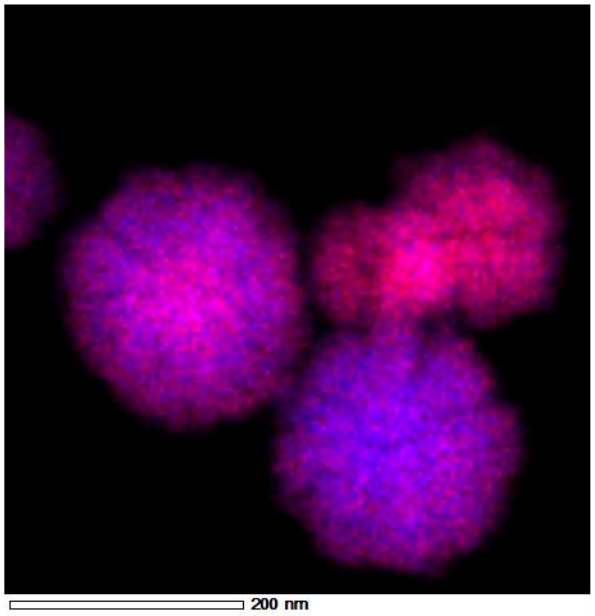

Area	Si (at%)	Ge (at%)
001	62	38
002	67	33
003	60	40
004	55	45
005	57	43
006	61	39
007	55	45
008	51	49
009	62	38
010	57	43
011	61	39

Fig. 7.6: The variation in composition between and within the NPs synthesized in the continuous plasma at R = 50 is visualized by these overlay images, where Si and Ge are indicated in red and blue, respectively. Table 7.3: Quantified amounts of various areas in Fig 7.6 in atomic fraction (%). The spread in composition is less than 10%.

We also studied NCs made from pure GeH_4 (R = 100). In this case, as seen in Fig. 7.7, we see NCs with star shaped morphology and the majority of them consist of pure Ge, as expected. We also see a small fraction of SiGe NCs, which could be due to the Si residues deposited on the reactor wall which are etched off (chemically sputtered [188]) to form SiGe NCs. The SiGe NPs observed here could also be released from the walls of previously deposited SiGe nanoparticles.

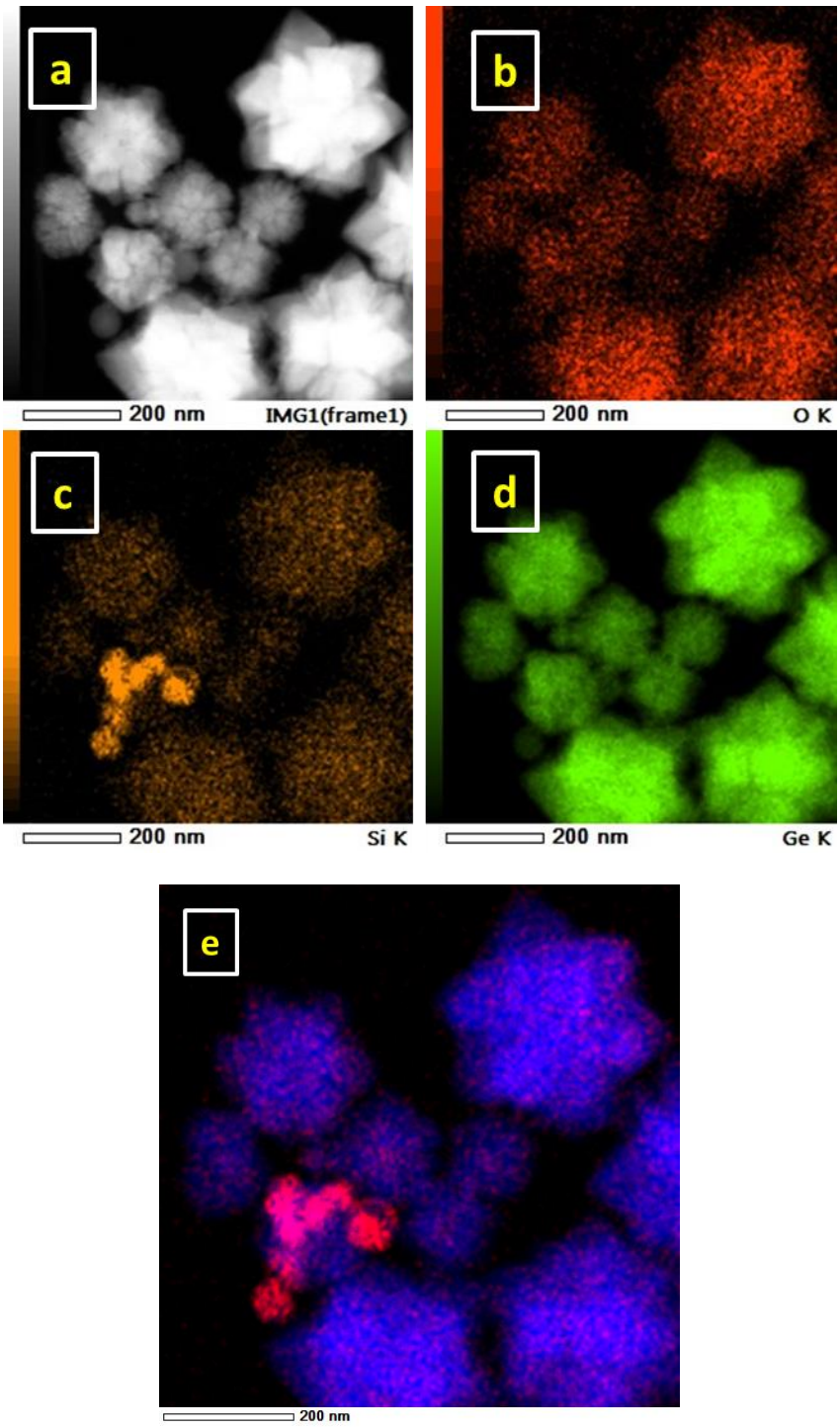

Fig. 7.7: (a) Raw EDS counts mapping of NCs with R = 100 (undiluted GeH_4 flow), (b) O map suggesting that the outer shells of the NC are oxidized, (c) Si mapping, (d) Ge mapping and (e) overlay image, almost no Si NCs present (given in red), majority are Ge (given in blue) NCs and a fraction of SiGe NCs (given in pink).

7.3.1.2 X Ray Diffraction (XRD)

We performed XRD measurements on all $Si_{1-x}Ge_X$ samples and observed a shift of the peak positions as a function of the gas phase ratio R (Fig 7.8 (a)). For the sample produced

with both Si and Ge, the peak positions are intermediate between those of pure Si and pure Ge. This result alone does not prove that alloyed NCs are produced, as the similar intermediate peak positions could be produced by a mixture of Si and Ge NCs. Additionally we notice that the FWHM (full width-half maximum) of the {111} peaks is very similar for all the three diffraction patterns. This is an affirmation that that the nanocrytal sizes are similar and the SiGe sample is composed of an alloyed material, since a mixture of Si and Ge NCs would result in a much broader XRD peak [28].

From the XRD patterns we calculated the lattice constant for each sample. We see that the lattice constant of the $Si_{1-x}Ge_x$ NCs increases with increasing Ge atomic fraction, as expected [189]. According to Vegard's law, the relationship between the lattice constant *a* (in Å) and Ge content of $Si_{1-x}Ge_x$ at 300 K is

$$a = 5.431 + 0.227x \qquad \text{Eq. (7.3)}$$

From the lattice constant (obtained from XRD measurements) and assuming the applicability of Vegard's law [190], we estimated the Ge content as given in Fig. 7.3. Vegard's law assumes that both components forming the alloy are in their pure form (i.e. before mixing), have the same crystal structure and that they form a solid solution upon mixing. For the calculations of *x*, the effect of stress is neglected. This is appropriate in our case because of unstrained nature of Si NCs produced in gas phase most probably related with the absence of a solid host matrix which can induce strain as a result of lattice mismatch.

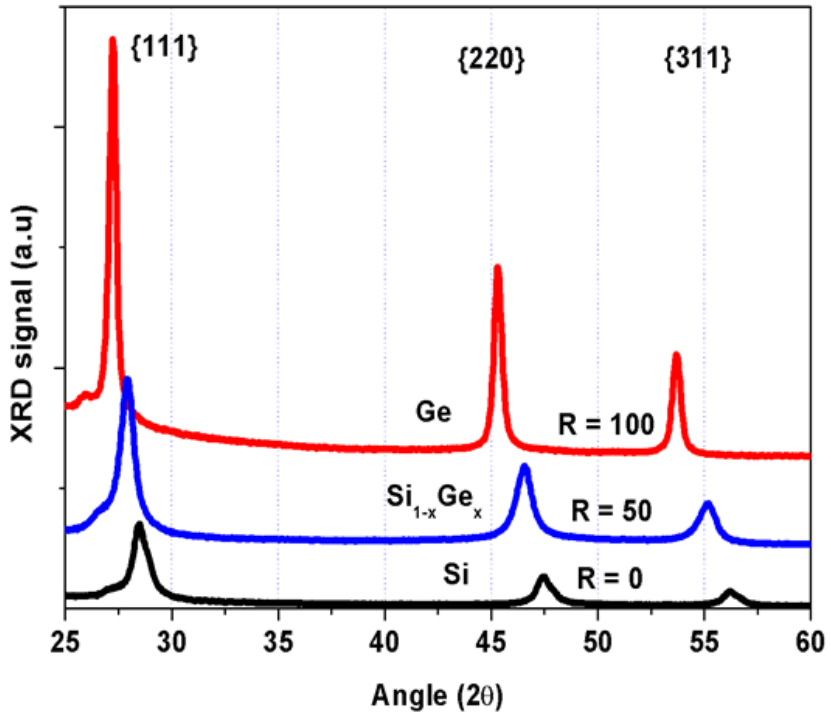

Fig. 7.8 (a): XRD patterns from Si, $Si_{1-x}Ge_x$ and Ge NCs.

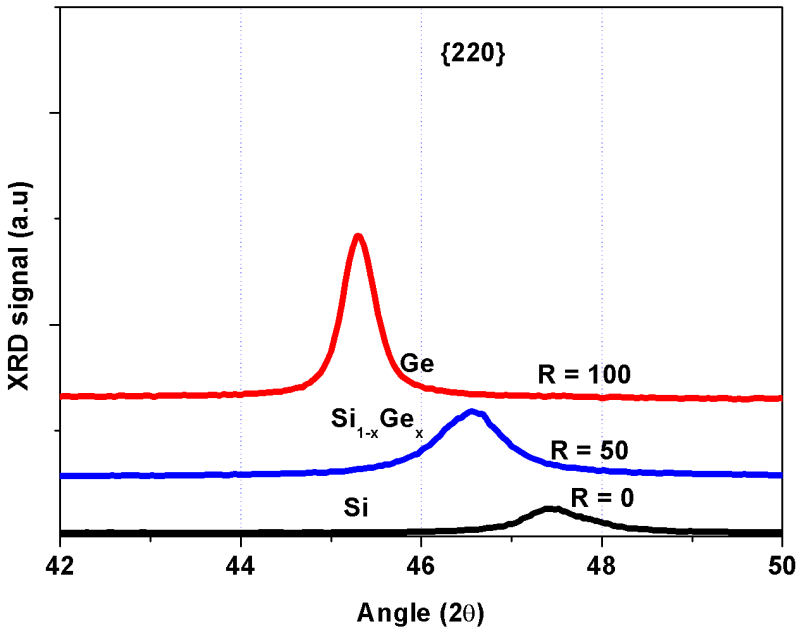

Fig. 7.8 (b): Close up of the {220} peak for XRD pattern at Fig. 7.8 (a) highlighting the shift.

As mentioned before, the NCs synthesized in continuous plasmas are agglomerated cauliflower shaped and spherical shaped particles. Although TEM measurements estimate the overall particle size to range from 50 to 300 nm, the nanocrystal size calculated with XRD (from the peak width using the Scherrer equation [75]) for all compositions is found to be less than 12 nm. This difference is explained by the fact that in TEM the entire particle size is measured, whereas XRD estimates the size of the individual crystalline domains within each particle.

7.3.1.3 Raman Spectroscopy

The crystallinity and the Ge atomic fraction were also calculated from Raman spectra, which are plotted in Fig. 7.9. There are three main factors that affect the Raman scattering frequencies of the $Si_{1-x}Ge_x$ alloy, namely (i) the relative Ge content (ii) stress and (iii) phonon confinement. We have ruled out stress in our case while calculating *x* in XRD measurements (as mentioned above) and in Raman measurements, due to the strain free nature of our particles formed in free space. According to reports of theoretical studies the shift of the peak due to the size effect can be neglected when the sizes of the nanocrystal domains size are larger than 10 nm [120]. Note that here, the size of the entire particle could be much larger, and the NC is usually composed of many polycrystalline particles. The presence of alloy NCs is confirmed by the presence of the SiGe transverse optic (TO) peak at 400 cm^{-1}. With changing Ge atomic fraction, the alloying-induced peak is associated with a red shift of the Si-Ge bonds. Additionally, the presence of Ge in the lattice lowers the Si-Si TO peak frequency because of the larger mass of the neighboring Ge atoms. The variation of the Si-Si

peak position is larger than that of the Si-Ge peak position and is thus used to estimate the Ge composition.

Using an analytical approach based on the phonon confinement model, it has been observed for Si nanocrystals that the Si-Si peak position is already sensitive to particle sizes even below 20 nm [191], however as the study described in [191] clearly shows the shift is not more than 0.5 cm^{-1} from the bulk value for 10 nm, confirming the size effects mentioned in [120]. This crystallite-size induced shift (which could be due to phonon confinement effect) is much smaller than the shift that we observe for the Si-Si TO peak in our Raman spectrum and thus can be neglected to a first approximation while estimating the Ge content. Alonso and Winer [192] have studied the correlation between the Si-Si Raman frequency and Ge content in the $Si_{1-x}Ge_x$ bulk which can be written as

$$y = 520.7 - 68\,x \qquad \text{Eq. (7.4)}$$

where *y* is the peak position of the Si-Si TO vibration and x is the fraction of Ge in the bulk [193]. Based on this equation, the Ge fraction in the sample is calculated and the spectra are labeled in Fig. 7.3. *The compositions estimated using all the three measurement techniques (EDS, XRD and Raman) are in excellent agreement, as is shown in Figure 7.3.*

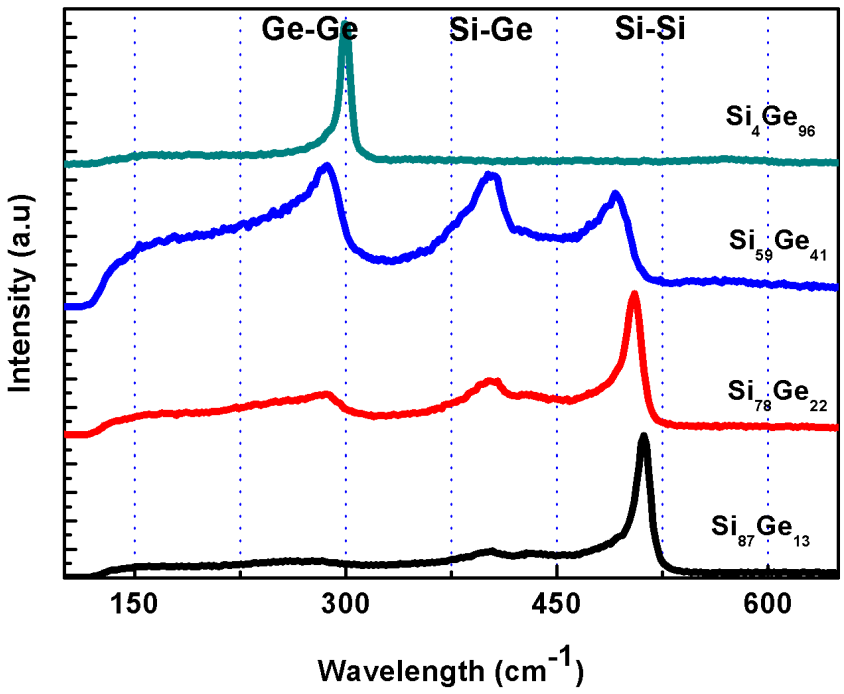

Fig. 7.9: Raman spectra from $Si_{1-x}Ge_x$ NCs with varying x.

7.3.2 Pulsed Plasma

In order to obtain smaller (quantum-sized), better size controlled $Si_{1-x}Ge_x$ NCs we used pulsed plasma conditions as described in section 7.2. The applied power was pulsed using t_{ON} = 100 ms and t_{OFF} = 1 s. Pulsing of the plasma during NC growth resulted in preventing the formation of cauliflower-structured NCs normally present in continuous plasmas.

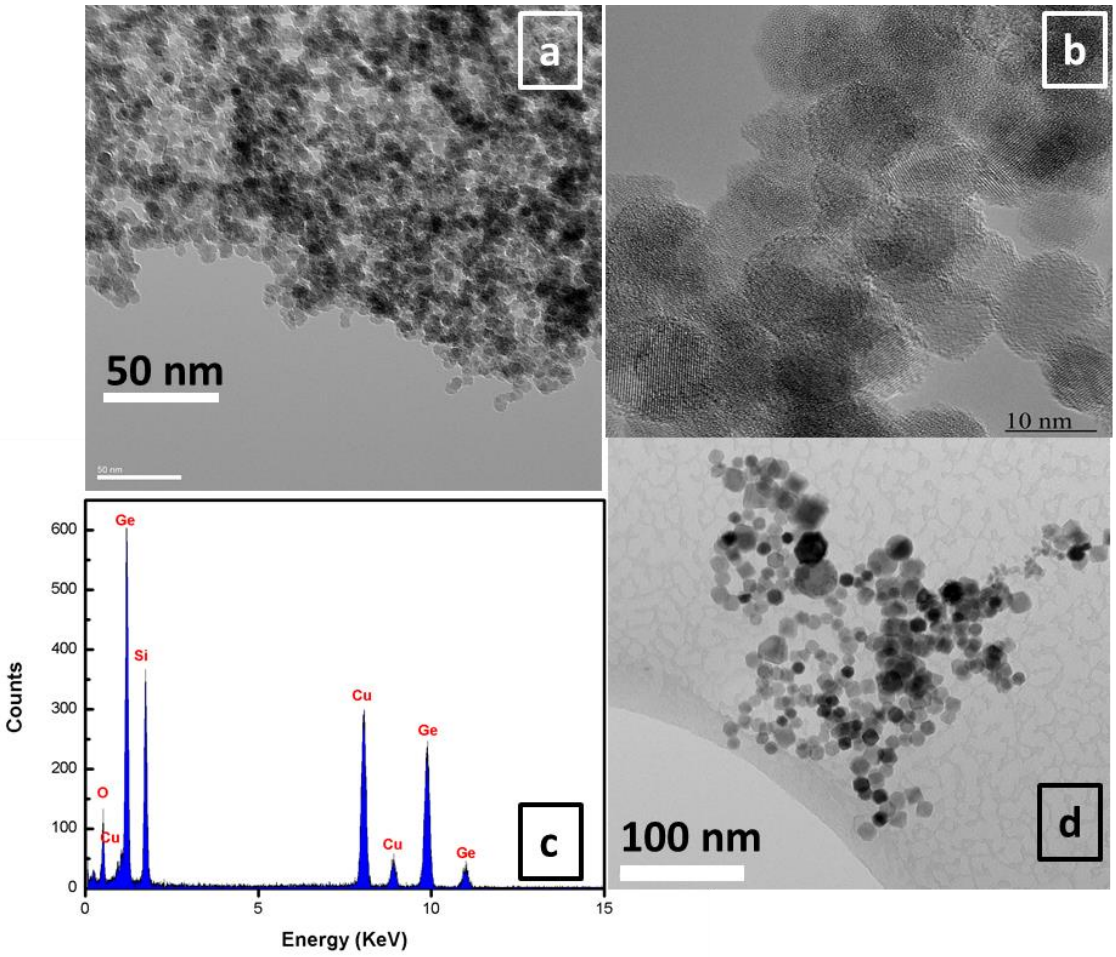

Fig. 7.10: (a) Overview of $Si_{1-x}Ge_x$ NCs obtained in the pulsed plasma; (b) HRTEM image of $Si_{1-x}Ge_x$ NCs showing a mixture of crystalline and amorphous particles, (c) EDS spectrum showing the presence of Si and Ge in the NCs produced in the pulsed mode and (d) spherical and faceted Ge NCs produced in the pulsed mode.

We found spherical NCs with a mean size of 7.8 ± 1.3 nm for particles (Fig. 7.10 (a)). The samples contain a mixture of amorphous particles and crystalline particles (Fig. 7.10 (b) and Fig. 7.11). The presence of amorphous particles is attributed to the shorter pulsing time leading to suboptimal coupling and lower power leading to lower crystalline fraction (Details in chapter 5). Further, EDS studies did show a constant distribution of Si and Ge material in majority of the particles studies (Fig. 7.10 (c)), in this case with an average ratio of Si:Ge =

54:46. This result clearly demosntrates that pulsing is an effective method to obtain quantum-sized homogeneous-alloy $Si_{1-x}Ge_x$ NCs without changing any other parameters. Thus far, we have not found any other reports on SiGe NCs produced in pulsed plasma. The removal of SiH_4 precursor gas and pulsing the power with the same parameters led to almost free standing crystalline Ge NCs with spherical and faceted morphology (Fig. 7.10 (d)). There are only a limited number of publications presenting a faceted morphology similar to ours, for instance the publication by Gresback et al [194].

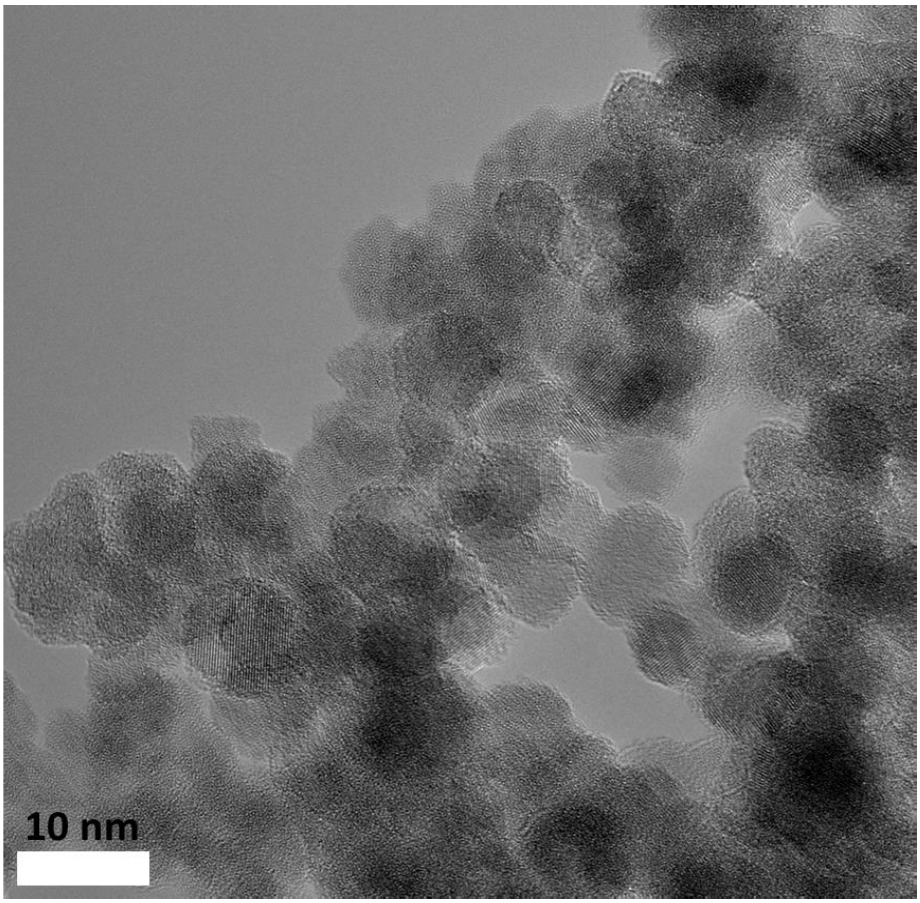

Fig. 7.11: HRTEM image of the mixture of amorphous and crystalline NPs produced in the pulsed plasma.

7.4 Conclusion

We have successfully demonstrated the formation of alloy $Si_{1-x}Ge_x$ NCs in the gas phase where x can be tuned from 0.1 to 1 by varying the precursor GeH_4 flow. Particles with a homogeneous alloy composition can be obtained in a single step process in a continuous plasma without any post processing required. The homogeneous alloy composition has been verified by XRD, EDS, and Raman spectroscopy, yielding excellent consistency. Pulsing has shown to be an effective method to obtain quantum-sized homogeneous $Si_{1-x}Ge_x$ alloy NPs.

References

[1] K. Dohnalová, A. Fuciková, C. P. Umesh, J. Humpolícková , J. M. J. Paulusse, J. Valenta, H. Zuilhof, M. Hof and T. Gregorkiewicz, "Microscopic Origin of the Fast Blue-Green Luminescence of Chemically Synthesized Non-oxidized Silicon Quantum Dots," *Small,* vol. 8, p. 3185, 2012.

[2] A. Saar, "Photoluminescence from silicon nanostructures: The mutual role of quantum confinement and surface chemistry," *J. Nanophoton. ,* vol. 3, p. 032501 , 2009.

[3] C. Delerue, G. Allan, and M. Lannoo, "Theoretical aspects of the luminescence of porous silicon," *Phys. Rev. B. ,* vol. 48, p. 11024, 1993.

[4] G. Ledoux, J. Gong, F. Huisken, O. Guillois and C. Reynaud, "Photoluminescence of size-separated silicon nanocrystals: Confirmation of quantum confinement," *Appl. Phys. Lett. ,* vol. 80, p. 4834 , 2002.

[5] D. Timmerman, J. Valenta, K. Dohnalová, W. D. A. M. de Boer and T. Gregorkiewicz, "Step-like enhancement of luminescence quantum yield of silicon nanocrystals," *Nat. Nanotechnol.,* vol. 6, p. 710, 2011.

[6] K. Dohnalová, A. N. Poddubny, A. A. Prokofiev, W. D. de Boer, C. P. Umesh, J. M. J. Paulusse, H. Zuilhof and T. Gregorkiewicz, "Surface brightens up Si quantum dots: direct bandgap-like size-tunable emission," *Light Sci Appl.,* vol. 2, p. e47, 2013.

[7] S. Schuppler, S. L. Friedman, M. A. Marcus, D. L. Adler, Y.-H. Xie, F. M. Ross, Y. J. Chabal, T. D. Harris, L. E. Brus, W. L. Brown, E. E. Chaban, P. F. Szajowski, S. B. Christman, and P. H. Citrin, "Size, shape, and composition of luminescent species in oxidized Si nanocrystals and H-passivated porous Si," *Phys. Rev. B ,* vol. 52, p. 4910, 1995.

[8] B. Delley and E. F. Steigmeier , "Quantum confinement in Si nanocrystals," *Phys. Rev. B,* vol. 47, p. 1397, 1993.

[9] R. J. Walters , Silicon Nanocrystals for Silicon Photonics. PhD thesis,, California: California Institute of Technology, 2007.

[10] T. E. Whall and E. H. C. Parker, "Silicon-germanium heterostructures - advanced materials and devices for silicon technology," *J. Mater. Sci. Mater. Electron.,* vol. 6, p. 249, 1995.

[11] J. Bardeen and W. H. Brattain, "The Transistor, A Semi-Conductor Triode," *Phys. Rev. ,* vol. 74, p. 230, 1948.

[12] M. Morse, "Germanium on silicon approaches III-V semiconductors in performance," *Laser Focus World,* vol. 43, p. 111, 2007.

[13] Y. Wu and P. Yang, "Germanium Nanowire Growth via Simple Vapor Transport," *Chem. Mater.,* vol. 12, p. 605, 2000.

[14] A. Bapat, C. Anderson, C. R. Perrey, Barry Carter, S. A. Campbell and U. Kortshagen, "Plasma synthesis of single-crystal silicon nanoparticles for novel electronic device applications," *Plasma Phys. Controlled Fusion,* vol. 46, p. B97, 2004.

[15] I. Dogan and M. C. M. van de Sanden, "Gas-Phase Plasma Synthesis of Free-Standing Silicon Nanoparticles for Future Energy Applications," *Plasma Process. Polym.,* vol. 13, p. 19, 2016.

[16] U. R. Kortshagen, R. M. Sankaran, R. N. Pereira, S. L. Girshick, J. J. Wu and E. S. Aydil, "Nonthermal plasma synthesis of nanocrystals: fundamental principles, materials, and applications," *Chem. Rev.,* vol. 116, p. 11061, 2016.

[17] C van der Wel, Optical diagnosis on dusty plasmas for nanocrystalline thin film silicon solar cells, Utrecht University: Masters thesis, 2012.

[18] M. Zacharias, J. Heitmann, R. Scholz, U. Kahler, M. Schmidt and J. Bläsing, "Size-controlled highly luminescent silicon nanocrystals: A SiO/SiO_2 superlattice approach," *Appl. Phys. Lett. ,* vol. 80, p. 661, 2002.

[19] R. Gago, L. Vázquez, R. Cuerno, M. Varela, C. Ballesteros and J. M. Albella, "Production of ordered silicon nanocrystals by low-energy ion sputtering," *Appl. Phys. Lett. ,* vol. 78, p. 3316 , 2001.

[20] T. S. Iwayama, N. Kurumado, D. E. Hole and P. D. Townsend, "Optical properties of silicon nanoclusters fabricated by ion implantation," *J. Appl. Phys.,* vol. 83, p. 6018, 1998.

[21] P. Mutti, G. Ghislotti, S. Bertoni, L. Bonoldi, G. F. Cerofolini, L. Meda, E. Grilli and M. Guzzi, "Room-temperature visible luminescence from silicon nanocrystals in silicon implanted SiO_2 layers," *Appl. Phys. Lett. ,* vol. 66, p. 851 , 1995.

[22] J. P. Wilcoxon, G. A. Samara, and P. N. Provencio, "Optical and electronic properties of Si nanoclusters synthesized in inverse micelles," *Phys. Rev. B ,* vol. 60, p. 2704, 1999.

[23] R. K. Baldwin , K. A. Pettigrew , J. C. Garno , P. P. Power, G. Liu and S. M. Kauzlarich, "Room Temperature Solution Synthesis of Alkyl-Capped Tetrahedral Shaped Silicon Nanocrystals," *J. Am. Chem. Soc.,* vol. 124, p. 1150, 2002.

[24] I. Dogan, N. J. Kramer, R. H. J. Westermann, K. Dohnalov, A. H. M. Smets, M. A. Verheijen, T. Gregorkiewicz, and M. C. M. van de Sanden., "Ultrahigh throughput plasma processing of free standing silicon nanocrystals with lognormal size distribution," *J. Appl. Phys.,* vol. 113, p. 134306, 2013.

[25] E. Borsella, M. Falconieri, S. Botti, S. Martelli, F. Bignoli, L. Costa, S. Grandi, L. Sangaletti, B. Allieri and L. Depero, "Optical and morphological characterization of Si nanocrystals/silica composites prepared by sol-gel processing," *Materials Science and Engineering B,* vol. 79, p. 55, 2001.

[26] L. Mangolini and U. Kortshagen, "Nonthermal Plasma Synthesis of Silicon Nanocrystals (Chapter 13)," in *Silicon Nanocrystals: Fundamentals, Synthesis and Applications*, Wiley-VCH, 2010, p. 309–348.

[27] X. D. Pi and U. Kortshagen, "Nonthermal plasma synthesized freestanding silicon-germanium alloy nanocrystals.," *Nanotechnology.,* vol. 20, p. 295602, 2009.

[28] O. Y. Inceoglu and L. Mangolini, "Characterization of Si-Ge alloy nanocrystals produced in a non-thermal plasma reactor," *Materials Letters ,* vol. 101, p. 76, 2013.

[29] F. Erogbogbo, T. Liu, N. Ramadurai, P. Tuccarione, L. Lai, M. T. Swihart and P. N. Prasad, "Creating Ligand-Free Silicon Germanium Alloy Nanocrystal Inks," *ACS Nano,* vol. 5, p. 7950, 2011.

[30] C. Mehringer, C. Kloner, B. Butz, B. Winter, E. Spiecker and W. Peukert, "Germanium-silicon alloy and core–shell nanocrystals by gas phase synthesis," *Nanoscale,* vol. 7, p. 5186, 2015.

[31] K. Nishiguchi, S. Hara, T. Amano, S. Hatatani and S. Oda, "Preparation of Nanocrystalline Silicon Quantum Dots by Pulsed Plasma Processes with High Deposition Rates," *MRS Proceedings ,* vol. 571, 1999.

[32] M. Shiratani, K. Koga, S. Ando, T. Inoue, Y. Watanabe, S. Nunomura, M. Kondo, "Single step method to deposit Si quantum dot films using H_2 + SiH_4 VHF discharges and electron mobility in a Si quantum dot solar cell," *Surf. Coat. Technol. ,* vol. 201, p. 5468, 2007.

[33] T. N. Tran, P.R. i Cabarrocas and G. Patriarche, "Study of radial growth rate and size control of silicon nanocrystals in square-wave-modulated silane plasmas," *Appl. Phys. Lett.,* vol. 91, p. 111501, 2007.

[34] L. Mangolini, E. Thimsen and U. Kortshagen , "High-Yield Plasma Synthesis of Luminescent Silicon Nanocrystals," *Nano Lett.,* vol. 5, p. 655, 2005.

[35] X. Li, Y. He, S. S. Talukdar and M. T. Swihart, "Process for Preparing Macroscopic Quantities of Brightly Photoluminescent Silicon Nanoparticles with Emission Spanning the Visible Spectrum," *Langmuir ,* vol. 19, p. 8490, 2003.

[36] F. Hua , M. T. Swihart and E. Ruckenstein, "Efficient Surface Grafting of Luminescent Silicon Quantum Dots by Photoinitiated Hydrosilylation," *Langmuir,* vol. 21, p. 6054, 2005.

[37] X. Li ,Y. He and M. T. Swihart , "Surface Functionalization of Silicon Nanoparticles Produced by Laser-Driven Pyrolysis of Silane followed by HF−HNO3 Etching," *Langmuir,* vol. 20, p. 4720, 2004.

[38] D. Jurbergs, E. Rogojina, L. Mangolini and U. Kortshagen, "Silicon nanocrystals with ensemble quantum yields exceeding 60%," *Appl. Phys. Lett. ,* vol. 88, p. 233116 , 2006.

[39] L. Mangolini, D. Jurbergs, E. Rogojina and U. Kortshagen, , "Plasma synthesis and liquid-phase surface passivation of brightly luminescent Si nanocrystals," *J. Luminescence,* vol. 121, no. 2, p. 327, 2006.

[40] S. Godefroo, M. Hayne, M. Jivanescu, A. Stesmans, M. Zacharias, O. I. Lebedev, G. Van Tendeloo and V. V. Moshchalkov, "Classification and control of the origin of photoluminescence from Si nanocrystals," *Nature Nanotechnology,* vol. 3, p. 174, 2008.

[41] L. Mangolini and U. Kortshagen, "Plasma-Assisted Synthesis of Silicon Nanocrystal Inks," *Adv. Mater.,* vol. 19, p. 2513, 2007.

[42] X. D. Pi, R. W. Liptak, S. A. Campbell and U. Kortshagen, "In-flight dry etching of plasma-synthesized silicon nanocrystals," *Appl. Phys. Lett. ,* vol. 91, p. 083112 , 2007.

[43] X. D. Pi, R. W. Liptak, J. D. Nowak ,N.P. Wells , C. B. Carter, S. A. Campbell, U. Kortshagen , "Air-stable full-visible-spectrum emission from silicon nanocrystals synthesized by an all-gas-phase plasma approach," *Nanotechnology. ,* vol. 19, p. 245603, 2008.

[44] P. Preecha and J. Jettanasen, "Investigation of functionalized silicon nanoparticles by size exclusion chromatography," *Mater. Res. Express ,* vol. 4 , p. 045007, 2017.

[45] K. Nishiguchi and S. Oda, "Electron transport in a single silicon quantum structure using a vertical silicon probe," *J. Appl. Phys,* vol. 88, p. 4186, 2000.

[46] Y. Fu, M. Willander, A. Dutta and S. Oda, "Carrier conduction in a Si-nanocrystal-based single-electron transistor-I. Effect of gate bias," *Superlatt Microstuct,* vol. 28, p. 177, 2000.

[47] K. Nishiguchi, X. Zhao and S. Oda, "Nanocrystalline silicon electron emitter with a high efficiency enhanced by a planarization technique," *J. Appl. Phys.,* vol. 92, p. 2748, 2002.

[48] Y. Ding, Y. Dong, A. Bapat, J. D. Nowak, C.B. Carter, U. R. Kortshagen, S. A. Campbell, "Single nanoparticle semiconductor devices," *IEEE Trans. Electron Devices ,* vol. 53, p. 2525, 2006.

[49] T. Matsoukas, "The Coagulation Rate of Charged Aerosols in Ionized Gases," *J. Colloid Interface Sci.,* vol. 187, p. 474, 1997.

[50] U. Kortshagen and U. Bhandarkar, "Modeling of particulate coagulation in low pressure plasmas," *Phys Rev E,* vol. 60, p. 887, 1999.

[51] T. V. Torchynska, A. V. Hernandez, M. Dybiec, Yu. Emirov, I. Tarasov, S. Ostapenko and Y. Matsumoto, "Optical characterization of crystalline silicon embedded in a-Si matrix," *Phys Status Solidi C,* vol. 2, p. 1832, 2005.

[52] J. Graetz, C. C. Ahn, R. Yazami and B. Fultz, , "Highly Reversible Lithium Storage in Nanostructured Silicon," *Electrochem. Solid-State Lett.,* vol. 6, no. 9, pp. A194-A197, 2003.

[53] Y. Kwon , G-Su. Park and J. Cho, "Synthesis and electrochemical properties of lithium-electroactive surface-stabilized silicon quantum dots," *Electrochimica Acta,* vol. 52, p. 4663, 2007.

[54] G. Conibeer, M. Green, R Corkish, Y. Cho, E. Cho, C. Jiang, T. Fangsuwannarak, E. Pink, Y. Huang, T. Puzzer, T. Trupke, B. Richards, A. Shalav and K. Lin, "Silicon nanostructures for third generation photovoltaic solar cells," *Thin Solid Films,* Vols. 511-512, p. 654, 2006.

[55] G. Conibeer, M. Green, E-C. Cho, D. König, Y-H. Cho, T. Fangsuwannarak, G. Scardera, E. Pink, Y. Huang, T. Puzzer, S. Huang, D. Song, C. Flynn, S. Park, X. Hao, D. Mansfield, "Silicon quantum dot nanostructures for tandem photovoltaic cells," *Thin Solid Films,* vol. 516, p. 6748, 2008.

[56] R. L. Delgado, H. J. H. Valenzuela, A. Z. Raynaud, A. Ramos, J. E. Pelayo, D. Berman, M. E. A. Ramos and A. Ayon, "Enhancing the power conversion efficiency of solar cells employing down-shifting silicon quantum dots," *J. Phys.: Conf. Ser,* vol. 773, p. 012087, 2016.

[57] X. Cheng, Stuart B. Lowe, P. J. Reece and J. J. Gooding, "Colloidal silicon quantum dots: from preparation to the modification of self-assembled monolayers (SAMs) for bio-applications," *Chem. Soc. Rev.,* vol. 43, p. 2680, 2014.

[58] Z. F. Li and E. Ruckenstein, "Water-Soluble Poly (acrylic acid) Grafted Luminescent Silicon Nanoparticles and Their Use as Fluorescent Biological Staining Labels," *Nano Lett.,* vol. 4, p. 1463, 2004.

[59] F. Erogbogbo, K. Yong, I. Roy, G. Xu, P. N. Prasad and M. T. Swihart, "Biocompatible Luminescent Silicon Quantum Dots for Imaging of Cancer Cells," *ASC Nano,* vol. 2, p. 873, 2008.

[60] M. S. Dresselhaus,G. Chen, M. Y. Tang, R. Yang, H. Lee, D. Wang, Z. Ren, J. Fleurial and P. Gogna, "New Directions for Low-Dimensional Thermoelectric Materials," *Adv. Mater. ,* vol. 19, p. 1043, 2007.

[61] G. H. Zhu, H. Lee, Y. C. Lan, X. W. Wang, G. Joshi, D. Z. Wang, J. Yang, D. Vashaee, H. Guilbert, A. Pillitteri, M. S. Dresselhaus, G. Chen and Z. F. Ren, "Increased Phonon Scattering by Nanograins and Point Defects in Nanostructured Silicon with a Low Concentration of Germanium," *Phys. Rev. Lett. ,* vol. 102, p. 196803, 2009.

[62] N. Petermann, N. Stein, G. Schierning, R. Theissmann, B. Stoib, M. S. Brandt, C. Hecht, C. Schulz and H. Wiggers , "Plasma Synthesis of Nanostructures for Improved Thermoelectric Properties," *J. Phys. D: Appl. Phys.,* vol. 44, p. 174034, 2011.

[63] R. Basu, S. Bhattacharya, R. Bhatt, M. Roy, S. Ahmad, A. Singh, M. Navaneethan, Y. Hayakawa, D. K. Aswal and S. K. Gupta, "Improved thermoelectric performance of hot pressed nanostructured n-type SiGe bulk

alloys," *J. Mater. Chem. A,* vol. 2, p. 6922, 2014.

[64] M. A. Lieberman, A. J. Lichtenberg, Principles of Plasma Discharges and Materials Processing, John Wiley & Sons, Inc., 2005.

[65] W. G. J. H. M. van Sark, Methods of Deposition of Hydrogenated Amorphous Silicon for Device Applications, San Diego, USA: Academic Press, 2002.

[66] B. Chapman, Glow Discharge Processes - Sputtering and Plasma Etching, New York: Wiley , 1980.

[67] A. Mohan, R.E.I. Schropp and J.K. Rath, "Gas phase growth of Si and SiGe nanoparticles," *Nevac Blad,* vol. 54, no. 3, p. 22, 2016.

[68] J. K. Rath, "Thin-Film Deposition Processes," in *Advanced Silicon Materials for Photovoltaic Applications*, Weinheim, John Wiley & Sons, Ltd, 2012, p. 235.

[69] A. Grill, Cold Plasma in Materials Fabrication - From Fundamentals to Applications, Piscataway, NJ: IEEE Press, 1994.

[70] M. Takai, T. Nishimoto, M. Kondo, and A. Matsuda, "Effect of higher-silane formation on electron temperature in a silane glow-discharge plasma," *Appl. Phys. Lett. ,* vol. 77, p. 2828 , 2000.

[71] A. Verkerk, Plasma deposition of thin film silicon at low substrate temperature and at high growth rate, Utrecht : PhD Thesis, Utrecht University, 2009.

[72] A. Bouchoule, A. Plain, L. Boufendi, J. Ph. Blondeau, and C. Laure, "Particle generation and behavior in a silane-argon low-pressure discharge under continuous or pulsed radio-frequency excitation," *J. Appl. Phys. ,* vol. 70, p. 1991, 1991.

[73] I. Dogan, Remote plasma synthesis of silicon nanocrystals: plasma processes, nanocrystal growth, and diagnosis, Eindhoven: PhD Thesis, TU/e, 2014.

[74] E. Bustarret, M.A. Hachicha and M. Brunel, "Experimental determination of the nanocrystalline volume fraction in silicon thin films from Raman spectroscopy," *Appl. Phys. Lett.,* vol. 52, p. 1675, 1988.

[75] P. Scherrer, *Göttinger Nachrichten Gesell.,* vol. 2, p. 98, 1918.

[76] G. S. Selwyn, J. Singh and R. S. Bennett., "Insitu laser diagnostic studies of plasma-generated particulate contamination.," *J. Vac. Sci. Technol. A,* vol. 7, no. 2759, p. 2758, 1989.

[77] G. S. Selwyn , "Optical characterization of particle traps," *Plasma Sources Sci. Technol.,* vol. 3, p. 340, 1994.

[78] P. Roca. i Cabarrocas, N. Chaâbane, A. V. Kharchenko, and S. Tchakarov, "Polymorphous silicon thin films produced in dusty plasmas: application to solar cells.," *Plasma Phys. Controlled Fusion,* vol. 46, p. B235, 2004.

[79] W. Shockley and H. J. Queisser, "Detailed Balance Limit of Efficiency of p-n Junction Solar Cells.," *J. Appl. Phys.,* vol. 32, p. 510, 1961.

[80] A. A. Fridman, L. Boufendi, T. Hbid, B. V. Potapkin and A. Bouchoule, "Dusty plasma formation: physics and critical phenomena. Theoretical approach," *J. Appl. Phys. ,* vol. 79 , p. 1303, 1996.

[81] A. Bouchoule., Dusty plasmas: physics, chemistry and technological impacts in plasma processing., John Wiley & Sons Ltd., 1999.

[82] A. A. Howling, C. Courteille, J. L. Dorier, L. Sansonnens, and Ch. Hollenstein., "From molecules to particles in silane plasmas," *Pure Appl. Chem.,* vol. 68, no. 5, p. 1017, 1996.

[83] L. Boufendi and A. Bouchoule , "Particle nucleation and growth in a low-pressure argon-silane discharge," *Plasma Sources Sci. Technol.,* vol. 3, p. 262, 1994.

[84] J. de Koning., "Observations on the transition from αlpha to gamma' plasma regime by the use of optical emission spectroscopy at different substrate temperatures.," Masters thesis, Utrecht University., 2009.

[85] H. Aguas, L. Raniero, L. Pereira, E. Fortunato and R. Martins, "Effect of the discharge frequency and impedance on the structural properties of polymorphous silicon," *Thin Solid Films ,* vol. 451 , p. 264, 2004.

[86] M. N. van den Donker, E. A. G. Hamers, and G. M. W. Kroesen., "Measurements and semi-empirical model describing the onset of powder formation as a function of process parameters in an RF silane–hydrogen discharge," *J. Phys. D: Appl. Phys,* vol. 38, no. 14, p. 2382, 2005.

[87] J. L. Andujar, E. Bertran, A. Canillas, C. Roch, and J.L. Morenza., "Influence of pressure and radio

frequency power on deposition rate and structural properties of hydrogenated amorphous silicon thin films prepared by plasma deposition," *J. Vac. Sci. Technol. A,* vol. 9, p. 2216, 1991.

[88] C. Bohm and J. Perrin., "Spatially resolved optical emission and electrical properties of SiH_4 RF discharges at 13.56 MHz in a symmetric parallel-plate configuration," *J. Phys. D: Appl. Phys.,* vol. 24, p. 865, 1991.

[89] G. Oversluizen and W. H. M. Lodders., "Optimization of plasma-enhanced chemical vapor deposition of hydrogenated amorphous silicon," *J. Appl. Phys,* vol. 83, p. 8002, 1998.

[90] K. B. Chai, W. Choe, C. R. Seon, and C. W. Chung., "Role of hydrogen in evolution of plasma parameters and dust growth in capacitively coupled dusty plasmas," *Appl. Phys. Lett.,* vol. 97, no. 20, p. 201503, 2010.

[91] J. Perrin, C. Bohm, R. Etemadi, and A. Lloret., "Possible routes for cluster growth and particle formation in RF silane discharges," *Plasma Sources Sci. Technol,* vol. 3, p. 252, 1994.

[92] L. Boufendi, A. Plain, J.Ph. Blondeau, A. Bouchoule, C. Laure, and M. Toogood., "Measurements of particle size kinetics from nanometer to micrometer scale in a low-pressure argon-silane radio-frequency discharge," *Appl. Phys. Lett.,* vol. 60, p. 169, 1992.

[93] T. Ifuku, M. Otobe, A. Itoh, and S. Oda., "Fabrication of Nanocrystalline Silicon with Small Spread of Particle Size by Pulsed Gas Plasma," *Jpn. J. Appl. Phys.,* vol. 36, p. 4031, 1997.

[94] A. D. Yoffe, "Low-dimensional systems: Quantum size effects and electronic properties of semiconductor microcrystallites (zero-dimensional systems) and some quasi-two-dimensional systems," *Adv. Phys.,* vol. 51, p. 799, 2002.

[95] M. M. de Jong, J. De Koning, J.K. Rath, and R.E.I. Schropp., "An optical analysis tool for avoiding dust formation in very-high frequency hydrogen diluted silane plasmas at low substrate temperatures," *Phys. Plasmas,* vol. 19, p. 020703, 2012.

[96] J. K. Rath, R. H. J. Franken, A. Gordijn, R. E. I. Schropp, and W. J. Goedheer., "Growth mechanism of microcrystalline silicon at high pressure conditions," *Journal of Non-Crystalline Solids,* vol. 338, p. 56, 2004.

[97] M. M. de Jong, On the Influence of Substrate Temperature on Plasma Characteristics, PhD Thesis, Utrecht University, 2009.

[98] J. Berndt, E. Kovacevic, I. Stefanovic, O. Stepanovic, S. H. Hong, L. Boufendi and J. Winter., "Some Aspects of Reactive Complex Plasmas," *Contrib. Plasma Phys.,* vol. 49, p. 107, 2009.

[99] W. W. Stoffels, E. Stoffels, G. M. W. Kroesen, and F. J. de Hoog., "Electron density fluctuations in a dusty Ar/SiH_4 rf discharge," *J. Appl. Phys.,* vol. 78, p. 4867, 1995.

[100] R. Martins, V. Silva, I. Ferreira, A. Domingues and E. Fortunato., "Role of the gas temperature and power to gas flow ratio on powder formation and properties of films grown by the PECVD technique," *Materials Science and Engineering: B,* vol. 69, p. 272, 2000.

[101] L. Landau and E. Teller., "Theory of sound dispersion," *Phys. Z. Sowjetunion,* vol. 10, p. 34, 1936.

[102] M. M. de Jong, A. Mohan, J.K. Rath, and R.E.I. Schropp., "Temperature Dependence of the Ion Energy Distribution in a Hydrogen Diluted Silane VHF Plasma," *AIP Conf. Proc,* vol. 1397, p. 411, 2011.

[103] E. Amanatides, S. Sfikas, D. Mataras, R. Bartlomé, G. Bugnon, F. Sculati-Meillaud, G. Parascandolo, C. Ballif., "Pressure and Flow Effect on Silane Consumption and Depletion in Microcrystalline Silicon Deposition Process," *EU PVSEC Proceedings,* p. 2624, 2012.

[104] G. Prabhuram and J. Goree, "Experimental observation of very low-frequency macroscopic modes in a dusty plasma," *Phys. Plasma,* vol. 3, p. 1212, 1996.

[105] M. Mikkian, L. Couëdel, M. Cavarroc, Y. Tessier, and L. Boufendi., "Self-excited void instability in dusty plasmas: plasma and dust cloud dynamics during the heartbeat instability," *New J. Phys.,* vol. 9, p. 268, 2007.

[106] G. Parascandolo, R. Bartlome, G. Bugnon, T. Söderström, B. Strahm, A. Feltrin, and C. Ballif., "Impact of secondary gas-phase reactions on microcrystalline silicon solar cells deposited at high rate," *Appl. Phys. Lett.,* vol. 96, p. 233508, 2010.

[107] P. Roca i Cabarrocas, J. B. Chévrier, J. Huc, A. Lloret, J. Y. Parey and J. P. M. Schmitt, "A fully automated hot-wall multiplasma-monochamber reactor for thin film deposition," *J. Vac. Sci. Technol. A,* vol. 9, p. 2331, 1991.

[108] B. J. Hinds, T. Yamanaka, and S. Oda, "Emission lifetime of polarizable charge stored in nano-crystalline Si

based single-electron memory," *J. Appl. Phys.,* vol. 90, p. 6402, 2001.

[109] K. D. Hirschman, L. Tsybeskov, S. P. Duttagupta and P. M. Fauchet, "Silicon-based visible light-emitting devices integrated into microelectronic circuits," *Nature ,* vol. 384, p. 338, 1996.

[110] A. Gupta, M. T. Swihart and H. Wiggers, "Luminescent Colloidal Dispersion of Silicon Quantum Dots from Microwave Plasma Synthesis: Exploring the Photoluminescence Behavior Across the Visible Spectrum," *Adv. Funct. Mater.,* vol. 19, p. 696, 2009.

[111] N. Chaabane, V. Suendo, H. Vach and P. R. i. Cabarrocas, "Soft landing of silicon nanocrystals in plasma enhanced chemical vapor deposition," *Appl. Phys. Lett,* vol. 88, p. 203111, 2006.

[112] S. Thompson, C. R. Perrey, C. B. Carter, T. J. Belich, J. Kakalios and U. Kortshagen, "Experimental investigations into the formation of nanoparticles in a⁄nc-Si:H thin films," *J. Appl. Phys.,* vol. 97, p. 034310, 2005.

[113] A. Bapat, M. Gatti, Yong-Ping Ding, S. A. Campbell and U. Kortshagen, "A plasma process for the synthesis of cubic-shaped silicon nanocrystals for nanoelectronic devices," *J. Phys. D: Appl. Phys.,* vol. 40, p. 2247, 2007.

[114] A. Bouchoule and L. Boufendi, "Particulate formation and dusty plasma behaviour in argon-silane RF discharge," *Plasma Sources Sci. Technol,* vol. 2, p. 204, 1993.

[115] C. Hollenstein, "The physics and chemistry of dusty plasmas," *Plasma Phys. Control. Fusion,* vol. 42, p. R93, 2000.

[116] G. M. Jellum, J. E. Daugherty and D. B. Graves, "Particle thermophoresis in low pressure glow discharges," *J. Appl. Phys,* vol. 69, p. 6923, 1991.

[117] L. Conde and L. Leon, "Visual observation of multiple double layers," *Plasma Science IEEE transactions,* vol. 27, p. 80, 1999.

[118] L. M. Ivan, G. Amarandei, M. Aflori, M. Mihai-Plugaru, C. Gaman, D.G. Dimitriu and M. Sanduloviciu, "Experimental observation of multiple double Layers structures in Plasma-part II: nonconcentric multiple double Layers," *Plasma Science, IEEE Transactions,* vol. 33, p. 544, 2005.

[119] M. Chesaux, A. A. Howling and Ch Hollenstein, "Funnelling of rf current via a plasmoid through a grid hole in an rf capacitive plasma reactor," *Plasma Sources Sci. Technol,* vol. 22, p. 055006, 2013.

[120] V. A. Volodin and V. A. Sachkov, "Improved model of optical phonon confinement in silicon nanocrystals," *Journal of Experimental and Theoretical Physics,* vol. 116, no. 1, p. 87, 2013.

[121] H. Richter, Z.P. Wang and L. Ley, "The one phonon Raman spectrum in microcrystalline silicon," *Solid State Communications,* vol. 39, p. 625, 1981.

[122] J. Söderlund, L. B. Kiss, G. A. Niklasson, and C. G. Granqvist, "Lognormal Size Distributions in Particle Growth Processes without Coagulation," *Phys. Rev. Lett,* vol. 80, p. 2386, 1998.

[123] K. Denpoh, "Locally enhanced discharges at gas hole outlets of a showerhead in a plasma etching reactor," *J. Phys. D: Appl. Phys,* vol. 42, p. 032003, 2009.

[124] M. Hirasawa, T. Orii and T. Seto, "Size-dependent crystallization of Si nanoparticles," *Appl. Phys. Lett.,* vol. 88, p. 093119, 2006.

[125] Y. Watanabe, M. Shiratani, Y. Kubo, I. Ogawa and S. Ogi, "Effects of low-frequencymodulation on rf discharge chemical vapor deposition," *Appl. Phys. Lett.,* vol. 53, p. 1263, 1988.

[126] L. Boufendi, A. Bouchoule and T. Hbid, "Electrical characterization and modeling of a dust forming plasma in a radio frequency discharge," *J. Vac. Sci. Technol. A,* vol. 14, p. 572, 1996.

[127] A. Mohan, M. M. de Jong, I. Poulios, R. E. I. Schropp and J. K. Rath, "Gas phase synthesis of two ensembles of silicon nanoparticles," *J. Phys. D Appl. Phys.,* vol. 48, p. 375201, 2015.

[128] W. Tang, J. J. Eilers, M. A. van Huis, D. Wang, R. E. I. Schropp and M. Di Vece, "Formation and photoluminescence of ‘‘Cauliflower” silicon nanoparticles," *J. Phys. Chem. C,* vol. 119, p. 11042, 2015.

[129] M. Shiratani, S. Maeda, K. Koga and Y. Watanabe., "Effects of gas temperature gradient, pulse discharge modulation, and hydrogen dilution on particle growth in silane RF discharges," *Jpn. J. Appl. Phys.,* vol. 39, p. 287, 2000.

[130] P. Francis, S. Patil, C. Rajesh, S. Chakraborty, S. Mahamuni, C. V. Dharmadhikari and S. V. Ghaisas, "Electronic and optical properties of agglomerated hydrogen terminated silicon nanoparticles," *Eur. Phys. J. D ,* vol. 67, p. 144, 2013.

[131] T. Hawa and M. R. Zachariah, "Coalescence kinetics of bare and hydrogen-coated silicon nanoparticles: a molecular dynamics study," *Phys. Rev. B. ,* vol. 71 , p. 165434, 2005.

[132] A. A. Howling, L. Sansonnens, J. L. Dorier and Ch. Hollenstein , "Time-resolved measurements of highly polymerized negative ions in radio frequency silane plasma deposition experiments," *J. Appl. Phys.,* vol. 75, p. 1340, 1994.

[133] S. J. Choi and M. J. Kushner, "The role of negative ions in the formation of particles in low pressure plasmas," *J. Appl. Phys. ,* vol. 74, p. 853, 1993.

[134] J. Costa, G. Sardin, J. Campmany, J. L. Andujar, A. Canillas and E. Bertran, "Production of silicon powder by square-wave modulated RF silane plasma," *MRS Proceedings,* vol. 286, p. 155, 1992.

[135] A. Mohan, R. E. I. Schropp, I. Poulios, W. J. Goedheer and J. K. Rath, "Optimizing the parameter space for increased crystallinity of silicon nanoparticles grown in the gas phase," *Phys. Status Solidi A,* vol. 1826, p. 213, 2016.

[136] T. Kakeya, K. Koga, M. Shiratani, Y. Watanabe and M. Kondo, "Production of crystalline Si nano-clusters using pulsed H_2 + SiH_4 VHF discharges," *Thin Solid Films,* vol. 506–507, p. 288, 2006.

[137] J. Zhao, V. Singh, P. Grammatikopoulos, C. Cassidy, K. Aranishi, M. Sowwan, K. Nordlund and F. Djurabekova, "Crystallization of silicon nanoclusters with inert gas temperature control.," *Phys. Rev. B,* vol. 91, p. 035419, 2015.

[138] D. B. Williams and C. B. Carter, Transmission Electron Microscopy: A Textbook for Materials Science, New York: Springer, 2009.

[139] R. E. Algra, M. A. Verheijen, L. F. Feiner, W. G. G. Immink, R. Theissmann, W. J. P. van Enckevort, E. Vlieg and E. P. A. M. Bakkers, "Paired twins and 112 morphology in GaP nanowires," *Nano Lett.,* vol. 10, p. 2349, 2010.

[140] I. Sunagawa, Crystals: Growth, Morphology & Perfection, Cambridge: Cambridge University Press, 2005.

[141] N. J. Kramer, R. J. Anthony, M. Mamunuru, E. S. Aydil and U. R. Kortshagen, "Plasma-induced crystallization of silicon nanoparticles," *J. Phys. D: Appl. Phys.,* vol. 47, p. 075202, 2014.

[142] D. Carter, "Optimized Process Performance Using the Paramount/Navigator Power Delivery/Match Solution," *Advanced Energy Industries Inc,,* p. White paper, 2007.

[143] R. Anthony and U. Kortshagen, "Photoluminescence quantum yields of amorphous and crystalline silicon nanoparticles," *Phys. Rev. B,* vol. 80, p. 115407, 2009.

[144] L. Mangolini and U. Kortshagen, "Selective nanoparticle heating: Another form of nonequilibrium in dusty plasmas," *Phys. Rev. E,* vol. 79, p. 026405, 2009.

[145] H. R. Maurer and H. Kersten, "On the heating of nano- and microparticles in process plasmas," *J. Phys. D Appl. Phys.,* vol. 44, p. 174029, 2011.

[146] L. Houben, C. Scholten, M. Luysberg, O. Vetterl, F. Finger and R. Carius, "Growth of microcrystalline nip Si solar cells: role of local epitaxy," *J. Non Cryst. Solids,* vol. 299, p. 1189, 2002.

[147] F. Galli, M. Mamunuru and U. R. Kortshagen, "The energy distribution function of ions impinging on nanoparticles in a collisional low-pressure plasma," *Plasma Sources Sci. Technol.,* vol. 21, p. 035002, 2012.

[148] M. Shiratani, H. Kawasaki, T. Fukuzawa, T. Yoshioka, Y. Ueda, S. Singh and Y. Watanabe, "Simultaneous in situ measurements of properties of particulates in RF silane plasmas using a polarization-sensitive laser-light-scattering method," *J. Appl. Phys.,* vol. 79, p. 104, 1996.

[149] M. R. Zachariah, M. J. Carrier and E. B. Barojas, "Properties of silicon nanoparticles: a molecular dynamics study," *J. Phys. Chem.,* vol. 100, p. 14856, 1996.

[150] S. Oda and K. Nishiguchi, "Nanocrystalline silicon quantum dots prepared by VHF plasma enhanced chemical vapor deposition," *Journal De Physique IV,* vol. 11, p. 1065, 2001.

[151] N. Lalic and J. Linnros, "Light emitting diode structure based on Si nanocrystals formed by implantation into thermal oxide," *JOL,* vol. 80, p. 263, 1998.

[152] S. Fujita and N. Sugiyama, "Visible light-emitting devices with Schottky contacts on an ultrathin amorphous silicon layer containing silicon nanocrystals," *Appl. Phys. Lett.,* vol. 74, p. 308, 1999.

[153] M. Molinari, H. Rinnert and M. Vergnat, "Effects of the amorphous-crystalline transition on the luminescence of quantum confined silicon nanoclusters," *Europhys. Lett.,* vol. 66, p. 674, 2004.

[154] S. Askari, V. Svrcek, P. Maguire and D. Mariotti, "The Interplay of Quantum Confinement and

Hydrogenation in Amorphous Silicon Quantum Dots," *Adv. Mater.,* vol. 27, p. 8011, 2013.

[155] H. K. Lee, B. Y. Jang, C. H. Ko, J. C. Lee and Y. K. Park, "Effects of Process Conditions on the Properties of Silicon Nanoparticles Synthesized by Gas Phase Reactions Using Inductive Coupled Plasma," *J. Nanosci. Nanotechnol.,* vol. 12, p. 1589, 2012.

[156] Y. Xu, Y. Han, C Liu, W. Yu, C. Ge, J. Li and L. Wang, "Experimental investigations into the formation of nanocrystal silicon thin film synthesized at low substrate temperature," *Superlattices and Microstructures,* vol. 75, p. 496, 2014.

[157] J. K. Rath, A. D. Verkerk, Y. Liu, M. Brinza, W. J. Goedheer and R. E. I. Schropp, "Gas phase considerations for the growth of device quality nanocrystalline silicon at high rate," *Mater. Sci. Eng. B,* vol. 159, p. 38, 2009.

[158] D. Mataras, S. Cavadias and D. E. Rapakoulias, "Spatially resolved LIF and OES in silane discharges," *Proceedings of the 9th International Symposium on Plasma Chemistry, Pugnochiuso,* p. 423, 1989.

[159] D. Mataras, S. Cavadias and D. Rapakoulias, "Power dissipation mechanisms in radio-frequency driven silane discharges: The influence of discharge geometry," *J. Vac. Sci. Technol. A ,* vol. 11, p. 664 , 1993.

[160] Y. Liu, A. D. Verkerk, J. K. Rath, R. E. I. Schropp and W. J. Goedheer, "Effects of pressure and inter-electrode distance on deposition of nanocrystalline silicon under high pressure conditions," *Phys. status solidi (c),* vol. 7, p. 575, 2010.

[161] R. C. Ross and J. Jaklik Jr., "Plasma polymerization and deposition of amorphous hydrogenated silicon from rf and dc silane plasmas," *J. Appl. Phys.,* vol. 55, p. 3785, 1984.

[162] S. Ishihara, M. Kitagawa, T. Hirao, K. Wasa, T. Arita and K. Mori, "Effects of discharge parameters on deposition rate of hydrogenated amorphous silicon for solar cells from pure SiH_4 plasma," *J. Appl. Phys.,* vol. 62, p. 485, 1987.

[163] B. Strahm and Ch. Hollenstein, "Powder formation in SiH_4–H_2 discharge in large area capacitively coupled reactors: A study of the combined effect of interelectrode distance and pressure," *J. Appl. Phys.,* vol. 107, p. 023302, 2010.

[164] K. B Chai, C.R. Seon, S.Y. Moon and W. Choe, "Parametric study on synthesis of crystalline silicon nanoparticles in capacitively-coupled silane plasmas," *Thin Solid Films,* vol. 518, p. 6614, 2010.

[165] C. Kendrick, G. Klafehn, T. Guan, I. Anderson, H. Shen, J. Redwing and R. Collins, "Controlled growth of SiNPs by plasma synthesis," *Solar Energy Materials & Solar Cells,* vol. 124, p. 1, 2014.

[166] B. N. Jariwala, N. J. Kramer, M. C. Petcu, D. C. Bobela, M. C. M. van de Sanden, P. Stradins, C. V. Ciobanu and S. Agarwal, "Surface Hydride Composition of Plasma-Synthesized Si Nanoparticles," *J. Phys. Chem. C,* vol. 115, p. 20375, 2011.

[167] M. J. Kushner, "Monte-Carlo simulation of electron properties in rf parallel plate capacitively coupled discharges," *J. Appl. Phys.,* vol. 54, p. 4958, (1983).

[168] C. Chan, Z. Jin and C. Whitaker, "Parametric investigation of the sheath potential in a low-frequency rf discharge," *J. Appl. Phys.,* vol. 62, p. 1633, (1987).

[169] J. Heitmann, F. Müller, M. Zacharias and U. Gösele, "Silicon Nanocrystals: Size Matters," *Adv. Mater.,* vol. 17, p. 795, 2005.

[170] S. D. Barry, Z. Yang, J.A. Kelly, E.J. Henderson and J.G.C. Veinot, "Synthesis of Si_xGe_{1-x} Nanocrystals Using Hydrogen Silsesquioxane and Soluble Germanium Diiodide Complexes," *Chem. Mater.,* vol. 23, p. 5096, 2011.

[171] S. C. Erwin, L. Zu, M. I. Haftel, A. L. Efros, T. A. Kennedy and D. J. Norris, "Doping semiconductor nanocrystals," *Nature,* vol. 436, p. 91, 2005.

[172] E. Jang, S. Jun and L. Pu, "High Quality CdSeS Nanocrystals Synthesized by Facile Single Injection Process and Their Electroluminescence.," *Chem. Commun,* vol. 24, p. 2964, 2003.

[173] R. E. Bailey and S. Nie, "Alloyed Semiconductor Quantum Dots: Tuning the Optical Properties without Changing the Particle Size," *J. Am. Chem. Soc.,* vol. 125, p. 7100, 2003.

[174] S. Takeoka, K. Toshikiyo, M. Fujii, S. Hayashiand and K. Yamamoto, "Photoluminescence from $Si_{1-x}Ge_x$ alloy nanocrystals," *Phys. Rev. B,* vol. 61, p. 15988, 2000.

[175] M. Fujii, D. Kovalev,J. Diener, F. Koch, S. Takeoka and S. Hayashi, "Breakdown of the k-conservation rule in $Si_{1-x}Ge_xSi_{1-x}Ge_x$ alloy nanocrystals: Resonant photoluminescence study," *J. Appl. Phys.,* vol. 88, p. 5772,

2000.

[176] C. Y. Liao, S. Y. Lin, S. C. Lee and C. T. Chia, "Spherical SiGe quantum dots prepared by thermal evaporation," *Appl. Phys. Lett.,* vol. 4328, p. 77, 2000.

[177] X. D. Pi, O. H. Y. Zalloum, A. P. Knights, P. Mascher and P. J. Simpson, "Electrical conduction of silicon oxide containing silicon quantum dots," *J. Phys.: Condens. Matter,* vol. 18, p. 9943, 2006.

[178] K. K. Lew, L. Pan, E.C. Dickey and J. M. Redwing, "Vapor- Liquid-Solid Growth of Silicon-Germanium Nanowires," *Adv. Mater.,* vol. 15, p. 2073, 2003.

[179] D. M. Rowe, Handbook of thermoelectric materials, CRC Press, 1995.

[180] M. S. Dresselhaus, G. Chen, M. Y. Tang, R. G. Yang, H. Lee, D. Z. Wang, Z. F. Ren, J. P. Fleurial and P. Gogna, "New Directions for Low-Dimensional Thermoelectric Materials," *Adv. Mater.,* vol. 19, p. 1043, 2007.

[181] S. K. Bux, R. G. Blair, P. K. Gogna, H. Lee, G. Chen, M. S. Dresselhaus, R. B. Kaner and J.P. Fleurial, "Nanostructured Bulk Silicon as an Effective Thermoelectric Material," *Adv. Funct. Mater,* vol. 19, p. 2445, 2009.

[182] Y. Maeda, "Visible photoluminescence from nanocrystallite Ge embedded in a glassy SiO_2 matrix: evidence in support of the quantum-confinement mechanism," *Phys. Rev. B,* vol. 51, p. 1658, 1995.

[183] T. Takagahara and K. Takeda, "Theory of the quantum confinement effect on excitons in quantum dots of indirect-gap materials," *Phys. Rev. B,* vol. 46, p. 15578, 1992.

[184] Y. Ming, C. S. Jayanthi, D. A. Drabold and S. Y. Wu, "Enhanced radiative transition in SinGem nanoclusters," *Phys. Rev. B,* vol. 68, p. 035404, 2003.

[185] A. D. Zdetsis, C. S. Garoufalis and E. N. Koukaras, "Mixed silicon–germanium nanocrystals: a detailed study of Si_xGe_{47-x}:H," *J. Math. Chem.,* vol. 46, p. 942, 2009.

[186] N. A. P. Mogaddam, A. S. Alagoz, S. Yerci, R. Turan, S. Foss and T. G. Finstad., "Phase separation in SiGe nanocrystals embedded in SiO_2 matrix during high temperature annealing," *J. Appl. Phys.,* vol. 104, p. 124309, 2008.

[187] J. Tarus, M. Tantarimäki, K. Nordlund, "Segregation in SiGe clusters," *Nucl. Instr. Meth. Phys. Res. B,* vol. 228, p. 51, 2005.

[188] W. Jacob and J. Roth, Chemical sputtering, in: Sputtering by Particle Bombardment , pp. 329–400., Berlin-Heidelberg: Springer-Verlag, 2007.

[189] E. Kasper and K. Lyutovich, Properties of Silicon Germanium and SiGe:Carbon, London: INSPEC, 2000.

[190] P. Becker, P. Scyfried and H. Siegert, "The lattice parameter of highly pure silicon single crystals," *Z. Phys. B: Condens. Matter,* vol. 48, p. 17, 1982.

[191] I. Dogan and M. C. M. van de Sanden, "Direct characterization of nanocrystal size distribution using Raman spectroscopy," *J. Appl. Phys.,* vol. 114, p. 134310, 2013.

[192] M. I. Alonso and K. Winer, "Raman spectra of c-$Si_{1-x}Ge_x$ alloys," *Phys. Rev. B,* vol. 39, p. 10056, 1989.

[193] J. S. Reparaz, I. C. Marcus, A. R. Goni, M. Garriga and M. I. Alonso, "Influence of alloy inhomogeneities on the determination by Raman scattering of composition and strain in $Si_{1-x}Ge_x$/Si(001) layers," *J. Appl. Phys.,* vol. 112, p. 023512, 2012).

[194] R. Gresback, Z. Holman and U. Kortshagen , "Nonthermal plasma synthesis of sizecontrolled, monodisperse, freestanding germanium nanocrystals," *Appl. Phys. Lett,* vol. 91 , p. 093119, 2007.

Summary

Bulk crystalline silicon (Si) is the dominant semiconductor material in the photovoltaics and microelectronics industry. Downscaling bulk Si to the nanometer regime opens up a world of opportunities as in this way the optoelectronic properties can be tuned over a large range. Si nanocrystals (NCs) less than 5 nm in size have optoelectronic properties not found in bulk material. Other desirable properties of Si NCs such as improved charge storage capacity and non-toxicity render them useful in lithium ion batteries and bio-labeling applications respectively. Alloying Si with germanium (Ge) provides an even larger degree of freedom in tailoring optoelectronic properties, by changing the relative contents of both materials. Alloy NCs can be used to meet multiple requirements of nanoparticles size and properties. The main objective of the thesis is the controlled synthesis and characterization of Si and SiGe NCs in a dedicated plasma reactor. We also investigate the influence of plasma properties on NC growth and crystallization.

Prior to synthesizing NCs in the dedicated plasma reactor, we investigate the oscillations found in the optical emission intensity and plasma current intensity to get an estimate of dust formation time scales. The motivation behind this is to obtain a suitable parameter space for use in pulsing plasmas to obtain precise particle sizes. Our interest in dusty plasmas originates from our goal to produce quantum dots (QDs), QDs are the polymerization precursors leading to powder, and a thorough understanding of their formation and growth is the key to control dust. Dust formation can be divided into two phases: the first phase starts with a dust free plasma (α regime), where negatively charged clusters are formed through polymerization reactions in the plasma. When the clusters reach a critical size and density, clusters coagulate and dust starts to form. Further growth proceeds by acquiring negative charge until charging effects prevent further agglomeration. The onset of the second phase, the dusty plasma (γ' regime) begins with the growth of individual dust particles by attachment of neutral particles or positive ions. This transition from dust free to dusty plasma is accompanied by significant changes in plasma characteristics, such as higher bulk emission and reduction in self-bias voltage, which we have investigated optically with in situ optical emission spectroscopy (OES) and electrically with a built-in VI probe. The output parameters of both optical and electrical measurements showed a patterned periodic oscillation in the dusty regime. However, for the same measurements performed in the non-dusty regime, there was no fluctuation in either optical or electrical measurements. For a deeper understanding, the trends of the fluctuation frequency with varying substrate temperatures and gas flows are studied. We observed that an increase in substrate temperature has an inverse effect on fluctuation frequency, whereas increasing the total gas flow increases the pulsing frequency. In the literature, similar fluctuations have been observed in dusty plasmas, each with different

periods of fluctuation, depending on the plasma parameters and the type of particles in the plasma. However, most of the research is based on a SiH_4:Ar plasma, and only a limited study on fluctuations has been done on the SiH_4:H_2 plasma. Based on our observation and those in the literature, it can be hypothesized that the fluctuations arise from periodic formation and ejection of a dust cloud from the plasma bulk when a critical dust size is reached. Our experimental results support this hypothesis; the fluctuation frequency increases with silane flow rate, which may be attributed to faster growth of dust with increased precursor flux, whereas it decreased with increasing substrate temperature, which may be attributed to slower polymerization reactions in the gas phase.

The details of the design and operation of a dedicated custom designed nanoparticle (NP) reactor to synthesize silicon (Si) NPs is provided. This reactor is a recent addition to the existing reactors in a multi-chamber VHF PECVD system ASTER (Amorphous Silicon Thin Film Experimental Reactor). The main advantage of our NP reactor design is that it is well adapted to standard capacitively coupled plasma reactors. Our reactor design is a triode system, in which the RF electrode and the electrode with the substrate holder are similar to that of the other reactors of ASTER, thus, allowing the handling of the substrate and gas feeding similar to other chambers and making it possible to fabricate a complete silicon quantum dot solar cell. The grounded grid electrode, placed between the RF electrode and the substrate electrode, controls and confines the plasma. The presence of holes in the grounded grid electrode has a prominent effect on the plasma in the vicinity of the holes, and produces a locally enhanced discharge. The enhancement can be attributed to the stream of highly dense group of electrons which increase the local ionization rate. The specialty of this NP reactor is that the bulk plasma creation of NPs can be tuned by a wide range of parameters such as inter-electrode distance, *p.d* product, pulsing of applied power, etc., independent of the substrate (as the substrate is not located in the plasma zone). The substrate, mounted to the grounded electrode, can be biased (floating potential) and even cooled (by liquid N_2), to vary the particles collection.

The proof of concept of the operation of this reactor is provided by demonstrating a fast and simple technique to synthesize non-embedded, non-agglomerated free standing silicon nanoparticles. Two ensembles of particles have been synthesized and the origin of these nanoparticles can be traced to two different locations in the plasma; one being created in the bulk and the other due to the locally enhanced plasma in the holes of grounded electrode. They have significantly different characteristics in terms of size, shape, and crystallinity. Particles produced in the bulk of the plasma are aggregates of cauliflower shaped crystalline particles. Particles produced in the locally enhanced plasma regions at the holes present in the grounded electrode are a mixture of free-standing quantum sized crystalline (mean size of 2.95 nm) and amorphous particles (mean size of 15 nm). We provide insight in different plasma processes leading to the formation of aggregates and free-standing particles. We highlight that the locally enhanced plasma has a pronounced effect on the particle formation and it contributes to the formation of, among other

particles, free standing quantum sized crystalline nanoparticles due to the presence of excess energetic electrons.

Precise size control of NPs can be obtained by varying the gas residence time in the discharge region or by pulsing the RF power ON (t_{ON}) and OFF times (t_{OFF}). By changing t_{ON} we have shown that both the size and crystallinity of the particles can be controlled. Higher power and longer t_{ON} leads to higher electron density which aids in particle heating resulting in a higher crystalline fraction of particles at longer t_{ON}. As largely reported in literature, multistep growth process of NPs in a SiH_4:Ar discharge is interpreted by invoking a process that involves nucleation and agglomeration, followed by silicon deposition on growing particles. Our study contradicts this claim and shows that NCs do not always grow according to the above agglomeration mechanism.

We study the time evolution of the formation of particles as a function of t_{ON} using HRTEM (High resolution transmission electron microscopy) and FFT (Fast Fourier transform) studies and identify three phases. We propose a mechanism that ultimately leads to the observed cauliflower structured particles. The particles formed at the beginning of phase I which are mostly amorphous are composed of branched networks of particles with sizes of a few nm, that can be attributed to polymerization. The beginning of crystallinity sets in at the end of the first phase in the process, phase I, and these particles display a polycrystalline nature. Comparison of FFT patterns of selected regions within the particle did not yield any basic symmetry relations between individual crystallites of the particle. We hypothesize that the complex polycrystalline particle could originate from a single nucleus and the gas phase species are subsequently added to this growing nucleus. When it becomes energetically more favorable for the formation of a new nucleus or crystal defect on the growing surface, another crystalline domain starts. A new nucleus is formed on the surface of the growing particle and local-epitaxial growth continues enabling the formation of multiple domains leading to cauliflower shaped particles. We cannot rule out that the cauliflower shaped NPs could be formed by coalescence of more than one nucleus or coalescence of different ‘‘branches” of the cauliflower particles. However, the absence of any voids or less dense regions in phase I between the multiple domains and HAADF (High-angle annular dark field) images which clearly indicate a center from which these branches of the cauliflower emerge out strengthen our one nucleus hypothesis compared with agglomeration.

The role of t_{OFF} is studied to tailor the size of the silicon NPs. This study infers that when t_{OFF} is less than the gas residence time, growth of complex multi-sized nanostructures occurs because some NPs which are not pumped out of the reactor stay between the electrodes and their growth continues for several pulses. This situation is overcome for longer t_{OFF}, which allows the source gas to be refreshed and the precursors of each growth cycle to be pumped away making conditions beneficial for obtaining quantum sized monodisperse NPs. Although deposition times are longer, this presents a clear advantage with regard to NP size

and homogeneity. TROES (Time resolved OES) studies confirmed that the number of hot electrons and the resulting radicals at the onset of plasma are strongly dependent on t_{OFF}.

We investigate the relationship between the various plasma parameters such as power density (*P*), pressure (*p*) and inter-electrode distance (*d*) on the crystallinity of the Si NPs obtained in the gas phase. One of the less studied parameters for NP growth in PECVD reactors is the inter-electrode distance. We specially focus on the effect of *d* and demonstrate how a plasma reactor with larger *d* (refers to *d* = 30 mm) is a simple method to enhance the crystalline fraction of NPs produced in them compared with a standard *d* (refers to *d* = 10 mm). The crystalline fraction increases dramatically when *d* increases from 10 mm to 30 mm. The morphology of the NPs is also significantly improved, low density polymeric chains and clustered NPs at *d* = 10 mm are replaced by compact single crystalline NPs at *d* = 30 mm. The transition from amorphous aggregates to completely crystalline single particles at higher electrode distance can be attributed to a higher collision probability of plasma species due to the higher residence times in the plasma volume at larger *d*. This enables a higher number of ion-electron recombination events at each particle, increasing the energy available for crystallization per NP.

We show that the crystalline fraction for the NPs increases with increasing power density concurrent with studies in the literature. An increase in plasma power density leads a significant increase in particle heating, creating particles with higher crystallinity.

We show that a higher process pressure leads to a higher residence time in the plasma volume if the gas flow in sccm is kept constant, which results in a higher frequency of collisions of electrons/ions with hydrogen, leading to particle heating and higher crystalline fraction.

We studied the entire *p* and *d* process parameter space possible for our reactor and show that the optimum parameter space for the growth of NPs with improved morphology and crystallinity is the regime of higher *p* and larger *d*. For our reactor it is most effective to use *p* above 0.8 mbar at d = 30 mm to obtain purely crystalline NPs. Increasing *d* or *p* is not strictly equivalent, and we establish how a higher *d* opens up a wider parameter space for obtaining single crystalline particles even at low process pressures and powers.

Reports on NC alloys are sparse, especially on alloys of Si and Ge formed in the gas phase. The difficulty in fabricating $Si_{1-x}Ge_x$ alloy QD lies in the segregation of the two phases which has also been predicted by molecular dynamics simulations. The segregation is attributed to differences in atomic size, surface energy, and surface diffusion disparity between Si and Ge, leading to inhomogeneous structures, which are more stable and energetically favorable than homogeneous structures. We have successfully synthesized highly crystalline and homogeneously alloyed $Si_{1-x}Ge_x$ NCs in continuous and pulsed plasmas. Agglomerated NCs have been produced with remarkable control over their composition by altering the precursor GeH_4 gas flow in a continuous plasma. The presence of $Si_{1-x}Ge_x$ alloy particles is

confirmed with multiple techniques, i.e. Raman spectroscopy, XRD (X-Ray diffraction) and HRTEM, with all of these methods consistently yielding the same composition. We specially highlight that in the pulsed plasma mode, we obtain quantum-sized free standing alloy NCs with a mean size of 7.3 nm. Thus far, we have not found other published reports on homogeneous SiGe NCs produced in pulsed plasma. The NCs synthesized here have potential applications in band-gap engineering for multijunction solar cells.

Samenvatting

Kristallijn silicium (Si) is de meest gebruikte halfgeleider in de fotovoltaïsche en micro-elektronica industrie. Het miniaturiseren van silicium van bulk- naar nanometerdimensies opent een wereld van mogelijkheden omdat de opto-elektronische eigenschappen van het materiaal op die manier over een groot bereik kunnen worden afgestemd. Si nanokristallen met een grootte van minder dan 5 nm hebben opto-elektronische eigenschappen die afwijken van die van bulkmateriaal. Si nanokristallen hebben een verbeterde opslagcapaciteit voor lading en zijn niet giftig. Dit zijn zeer gewilde eigenschappen voor nanodeeltjes, hetgeen Si nanokristallen geschikt maakt voor toepassingen in respectievelijk lithium-ion batterijen en bio-labels. Het legeren van Si met germanium (Ge) en het variëren van de relatieve concentratie van de elementen zorgt voor een nóg grotere vrijheid in het afstemmen van de opto-elektronische eigenschappen. Nanokristallen van deze legeringen kunnen worden gebruikt om te voldoen aan uiteenlopende eisen aan de afmetingen en aan andere eigenschappen van nanodeeltjes. Het hoofddoel van dit proefschrift is de gecontroleerde synthese en karakterisatie van Si en SiGe nanokristallen in een speciale plasmareactor.

Voordat nanokristallen werden gesynthetiseerd in deze speciale plasma reactor zijn de oscillaties onderzocht die werden gevonden in de intensiteit van zowel de optische emissie als in de plasmastroom, om zo een afschatting te maken van de relevante tijdschalen bij de formatie van stof. De motivatie hiervoor is dat een geschikte parameterruimte moest worden gevonden waarbinnen nanokristallen — gemaakt met pulserende plasma's — met de juiste afmetingen kunnen worden verkregen. Onze interesse in dergelijke stoffige plasma's komt voort uit ons doel om kwantumdots (KD) te produceren. KD zijn de polymerisatieprecursors die uiteindelijk leiden tot poeder en een gedegen begrip van hun formatieproces is dus cruciaal voor het beheersen van stof. Stofvorming kan worden opgedeeld in twee fases. De eerste fase start met een stofvrij plasma (α regime), waar negatief geladen clusters worden gevormd door polymerisatiereacties in het plasma. Wanneer de clusters een kritische grootte en concentratie bereiken, hopen ze zich op en begint de vorming van stof. Verdere groei vindt plaats doordat de clusters negatieve lading verzamelen totdat ladingseffecten verdere ophoping ervan verhindert. Het begin van de tweede fase, het stoffige plasma (γ' regime), begint met de groei van individuele stofdeeltjes door aanhechting van neutrale deeltjes of positief geladen ionen. Deze overgang van stofvrij tot stoffig plasma wordt vergezeld door significante veranderingen van de plasmakarakteristieken zoals een hogere bulkemissie en een verlaging van de eigen bias-spanning, die door ons optisch is bestudeerd door middel van in situ optische emissie spectroscopie (OES) en elektrisch door middel van een ingebouwde V-I sonde. Zowel de optische als elektrische metingen in het stoffige plasma lieten een oscillatie zien. Echter, dezelfde metingen, uitgevoerd in het stofvrije plasma, lieten geen periodieke fluctuaties

zien. Om dit beter te kunnen begrijpen zijn de trends in de fluctuatiefrequentie bij variërende substraattemperaturen en gasstroomsnelheden bestudeerd. We hebben gezien dat een verhoging van de substraattemperatuur de fluctuatiefrequentie verlaagt, terwijl het verhogen van de gasstroomsnelheid een tegengesteld effect heeft. In de literatuur zijn vergelijkbare fluctuaties waargenomen in stoffige plasma's, waarbij verschillende fluctuatieperioden zijn gevonden, afhankelijk van de plasmaparameters en het type deeltjes in het plasma. Het meeste onderzoek is echter uitgevoerd met SiH_4:Ar plasma's, terwijl onderzoek naar fluctuaties in SiH_4:H_2 plasma's maar in beperkte mate is uitgevoerd. Naar aanleiding van zowel onze waarnemingen als die in de literatuur hebben we de hypothese kunnen opstellen dat de fluctuaties worden veroorzaakt door periodieke vorming van een stofwolk en uitstoting van deze wolk vanuit de bulk van het plasma wanneer een kritische stofgrootte is bereikt. Onze experimentele resultaten ondersteunen deze hypotheses; de fluctuatiefrequentie neemt toe met de gasstroomsnelheid van silaan. De verhoogde fluctuatiefrequentie kan worden toegewezen aan een snellere groei van stof bij een hogere precursor flux. De fluctuatiefrequentie neemt daarentegen af met toenemende substraattemperatuur, wat zou kunnen worden toegewezen aan langzamere polymerisatiereacties in de gasfase.

De details van het ontwerp en het gebruik van een speciaal ontworpen reactor voor nanodeeltjes (NDs) worden in dit werk behandeld. Deze reactor is een recente toevoeging aan de reeds bestaande reactors in het multireactor VHF PECVD systeem ASTER (*Amorphous Silicon Thin Film Experimental Reactor*). Het grootste voordeel van ons ontwerp van de NDs reactor is dat deze goed aansluit bij de gangbare capacitief gekoppelde plasmareactors. De door ons ontworpen reactor heeft een triode systeem, waarin zowel de RF-elektrode als de elektrode met de substraathouder vergelijkbaar zijn met die van de andere reactors in het ASTER systeem. Hierdoor kan het substraat op een vergelijkbare manier worden behandeld en het gassysteem op een vergelijkbare manier worden aangesloten als in de andere reactors, wat het mogelijk maakt om een volledige silicium kwantumdot zonnecel te fabriceren. De geaarde roosterelektrode, die tussen de RF-elektrode en de substraatelektrode geplaatst is, biedt controle over het plasma. De aanwezigheid van gaten in deze electrode heeft een prominent effect op het plasma in de nabijheid van de gaten en produceert lokaal versterkte ontladingen. De versterking kan worden toegewezen aan de stroom van elektronen met hoge dichtheid, hetgeen de ionisatiesnelheid lokaal verhoogt. Het bijzondere van deze NDs reactor is dat de vorming van NDs in het bulkplasma kan worden beheerst door een grote hoeveelheid parameters zoals de afstand tussen de elektrodes, het druk-afstand (*p.d*) product, het pulseren van het toegepaste vermogen, etc., onafhankelijk van het substraat (omdat het substraat zich niet in het plasmagebied bevindt). Op het substraat, dat is bevestigd op de geaarde elektrode, kan een biasspanning worden aangebracht en het kan zelfs worden gekoeld (door vloeibaar N_2) om zo het verzamelen van de deeltjes te bevorderen.

Het concept van de werking van de reactor is bewezen door het demonstreren van een snelle en simpele techniek om vrijstaande, niet-ingebouwde en niet-samengeklonterde, silicium nanodeeltjes te maken. Twee deeltjesverzamelingen werden gefabriceerd en de oorsprong van de nanodeeltjes kan worden herleid naar twee verschillende locaties in het plasma. Het ene soort deeltje is gevormd in de bulk van het plasma en het andere in het lokaal versterkte plasma nabij de gaten van de geaarde elektrode. Deze twee soorten deeltjes hebben significant verschillende eigenschappen zoals grootte, vorm en kristalliniteit. Deeltjes die zijn gevormd in de bulk van het plasma zijn samenklonteringen van bloemkoolvormige kristallijne deeltjes. Deeltjes die zijn gevormd in de lokaal versterkte plasmagebieden bij de gaten in de geaarde elektrode zijn een mix van vrijstaande kristallijne deeltjes van kwantumdimensies (met een gemiddelde grootte van 2.95 nm) en amorfe deeltjes (met een gemiddelde grootte van 15 nm). Vanuit het inzicht dat is bereikt in de verschillende plasmaprocessen die leiden tot de vorming van samenklonteringen en vrijstaande deeltjes benadrukken we dat het lokaal versterkte plasma een sterk effect heeft op de vorming van deeltjes en dat het bijdraagt aan de vorming van onder andere vrijstaande kristallijne nanodeeltjes met kwantumgrootte, vanwege de aanwezigheid van een overmaat aan energetische elektronen.

Precieze controle over de grootte van NDs kan worden bereikt door het variëren van de verblijftijd van het gas in de ontlading of door het variëren van de AAN (t_{AAN}) en UIT (t_{UIT}) tijd van het pulserende RF-vermogen. We hebben laten zien dat we zowel de grootte als de kristalliniteit van de deeltjes kunnen beheersen door t_{AAN} te veranderen. Een hoger vermogen leidt tot een hogere elektronendichtheid, wat helpt bij het verhitten van de deeltjes en zorgt voor een hogere mate van kristalliniteit van de deeltjes bij een langere t_{AAN}. Zoals in hoofzaak wordt gerapporteerd in de literatuur, wordt het multi-stap groeiproces van NDs in een SiH_4:Ar ontlading geïnterpreteerd als een proces waarin zowel nucleatie als samenklontering een rol spelen, waarna de depositie van silicium volgt op de deeltjes, waardoor ze groeien. Onze studie spreekt deze bewering tegen en laat zien dat nanokristallen niet altijd groeien volgens het bovenstaande mechanisme van samenklontering.

We bestuderen het tijdsverloop van de formatie van deeltjes als functie van t_{AAN} met behulp van HRTEM (hoge resolutie transmissie elektronenmicroscopie) en FFT (*fast Fourier transform*) onderzoek en identificeren drie fases. We stellen een mechanisme voor dat uiteindelijk leidt tot de waargenomen bloemkoolvormige deeltjes. De deeltjes die grotendeels amorf zijn en die worden gevormd aan het begin van de eerste fase, fase I, bestaan uit vertakte netwerken van deeltjes met afmetingen van enkele nanometers, veroorzaakt door polymerisatie. Het kristallisatieproces begint aan het einde van fase I. Deze deeltjes hebben polykristallijne eigenschappen. De vergelijking van FFT-patronen van geselecteerde regio's in een deeltje heeft geen basis symmetrierelaties tussen individuele kristallieten van het deeltje aangetoond. We veronderstellen dat het complexe polykristallijne deeltje kan zijn ontstaan vanuit een enkele kern en dat deeltjes uit de gasfase

vervolgens zijn toegevoegd aan deze groeiende kern. Wanneer de vorming van een nieuwe kern of kristaldefect op het groeiende oppervlak energetisch voordeliger is, start de vorming van een nieuw kristaldomein. Een nieuwe kern wordt gevormd op het oppervlak van het groeiende deeltje en de lokaal-epitaxiale groei gaat verder, wat zorgt voor de vorming van meerdere domeinen en bloemkoolvormige deeltjes. We kunnen niet uitsluiten dat de bloemkoolvormige deeltjes gevormd worden door het samensmelten van meer dan één kern of het samensmelten van verschillende "takken" van bloemkoolvormige deeltjes. Echter, zowel de afwezigheid van holtes of minder dichte gebieden tussen de verschillende domeinen, als HAADF (*High-angle annular dark field*) afbeeldingen die een duidelijk centrum laten zien van waaruit de verschillende vertakkingen van de bloemkoolvorm groeien, versterken onze hypothese van één kern ten opzichte van samensmelting van meerdere kernen.

De rol van t_{UIT} is bestudeerd in de beheersing van de grootte van de NDs. Dit onderzoek wijst uit dat wanneer t_{UIT} kleiner is dan de verblijftijd van het gas, de groei van complexe nanostructuren met verschillende groottes plaatsvindt omdat sommige NDs niet uit de reactor worden gepompt maar achterblijven tussen de elektrodes, waardoor hun groei meerdere pulsen voortduurt. Deze situatie kan worden voorkomen door een langere t_{UIT} te kiezen, waardoor het brongas kan worden ververst, de precursors van elke groeicyclus weggepompt kunnen worden en de condities voor het verkrijgen van NDs met een specifieke grootte verbeteren. Hoewel de depositietijd hierdoor langer wordt, zorgt dit voor een duidelijk voordeel wat betreft de grootte en homogeniteit van de NDs. Met TROES (*time resolved OES*) studies hebben we bevestigd dat het aantal hete elektronen en de resulterende radicalen bij de start van het plasma sterk afhangen van t_{UIT}.

We onderzoeken de relatie tussen de verschillende plasmaparameters zoals vermogensdichteid (*P*) druk (*p*) en inter-elektrodeafstand (*d*) op de kristalliniteit van de Si NDs die zijn verkregen in de gasfase. Een van de minder bestudeerde parameters voor de groei van NDs in PECVD reactors is de inter-elektrodeafstand. We richten ons met name op het effect van *d* en demonstreren hoe een plasmareactor met een grotere *d* (*d* = 30 mm) de kristalliniteit van de geproduceerde NDs op een eenvoudige manier verhoogt vergeleken bij een reactor met een standaard *d* (*d* = 10 mm). De kristalliniteit wordt drastisch verhoogd wanneer *d* wordt vergroot van 10 mm naar 30 mm. De vorm van de NDs is ook significant verbeterd. Samengeklonterde NDs polymeerketens van lage dichtheid bij *d* = 10 mm worden vervangen door compacte volledig kristallijne NDs bij *d* = 30 mm. De overgang van amorfe en samengesmolten deeltjes naar volledig kristallijne losse deeltjes bij de grotere elektrodeafstand kan worden verklaard door de hogere botsingskans van plasmadeeltjes vanwege de langere verblijfstijden in het plasmavolume bij grotere *d*. Dit zorgt voor een hoger aantal ion-elektron recombinatiegebeurtenissen per deeltje, wat de beschikbare energie voor kristallisatie vergroot.

We laten zien dat de kristalliniteit van de NDs toeneemt met toenemend plasmavermogen, hetgeen in overeenstemming is met studies in de literatuur. We laten zien dat een hogere procesdruk leidt tot een langere verblijfstijd in het plasmavolume wanneer de gasstroomsnelheid constant wordt gehouden. Dit resulteert in een hogere botsingsfrequentie van elektronen/ionen met waterstof, wat zorgt voor verhitting van de deeltjes en een hogere kristalliniteit. We hebben de volledig mogelijke paramaterruimte van *p* en *d* in onze reactor bestudeerd en we laten zien dat de optimale paramaterruimte voor de groei van NDs met verbeterde vorm en kristalliniteit het regime van hogere *p* en grotere *d* is. Voor het verkrijgen van volledig kristalline NDs is het in onze reactor het meest effectief om een druk *p* boven 0.8 mbar bij een inter-elektrodeafstand *d* van 30 mm te gebruiken. Het verhogen van *d* of *p* is niet noodzakelijk equivalent en we stellen vast dat een hogere *d* een ruimere parameterruimte opent voor het verkrijgen van volledig kristallijne deeltjes, zelfs bij lage procesdruk en vermogen.

List of publications

Publications within the scope of this thesis

A. Mohan, C.M. van der Wel, R.E.I. Schropp, and J.K. Rath. "Probing periodic oscillations in a silane dusty plasma in a very high-frequency plasma enhanced chemical vapor deposition process." *Can. J. Phys.* **92** 744–748 (2014) http://dx.doi.org/10.1139/cjp-2013-0611

A. Mohan, M.M. de Jong, I. Poulios, R.E.I. Schropp and J.K. Rath. "Gas phase synthesis of two ensembles of silicon nanoparticles" *J. Phys. D: Appl. Phys.* **48** 375201 (2015) DOI: 10.1088/0022-3727/48/37/375201

A. Mohan, I. Poulios, R.E.I. Schropp and J.K. Rath. "Size control of gas phase grown silicon nanoparticles by varying the plasma OFF time in silane pulsed plasma" *Mater. Res. Soc. Symp. Proc* **1803** (2015) DOI: https://doi.org/10.1557/opl.2015.476

A. Mohan, R. E. I. Schropp, I. Poulios, W. J.Goedheer and J. K Rath."Optimizing the parameter space for increased crystallinity of silicon nanoparticles grown in the gas phase" *Physica Status Solidi (A)* **213** 1-5 (2016) DOI: 10.1002/pssa.201532938

A. Mohan, F. D. Tichelaar, M. Kaiser, M. A. Verheijen, R. E. I. Schropp and J. K. Rath. "Gas phase grown silicon germanium nanocrystals." *Chem. Phys. Lett.* **661** 185–190 (2016) http://doi.org/10.1016/j.cplett.2016.08.066

A. Mohan, R.E.I. Schropp and J.K. Rath "Gas phase growth of Si and SiGe nanoparticles." *Nevac Blad*. **54** 22 (2016)

A. Mohan, M. Kaiser, M. A. Verheijen, R.E.I. Schropp and J.K. Rath "Microscopic studies of polycrystalline nanoparticle growth in free space." *J. Cryst. Growth* **467** 137 (2017) http://doi.org/10.1016/j.jcrysgro.2017.03.044

Publications outside the scope of this thesis

M.M. de Jong, A. Mohan, J.K. Rath, and R.E.I. Schropp, "Temperature dependence of the ion energy distribution in a hydrogen diluted silane VHF plasma." *AIP Conference Proceedings*. **1397** 411-412 (2011) doi: http://dx.doi.org/10.1063/1.36598

Acknowledgements

Thanking people in a few words after receiving such immense support and guidance and learning so much is the hardest and most incomplete part of this thesis.

First I would like to express my heartfelt gratitude to prof. Ruud Schroop for giving me an opportunity to pursue my PhD in his group. His in depth knowledge, constant feedback and criticism has been crucial on the outcome of this thesis. Special thanks for helping me participate in excellent conferences in Hawaii, Toronto, San Francisco; it helped me get a lot of exposure and gave me a lot of confidence to present my work. Especially the last one year, when I had almost given up on the thesis, thank you so much for charting plans and deadlines for me and being so patient when I couldn't adhere to some! I would like to express my sincerest gratitude and appreciation to my direct supervisor Jatin Rath, who constantly took special care of me from my first day of interview in the group till the day of the defense. He has always made himself available to me for discussion and advice, no matter how busy he has been. We have had countless discussions, both academic and nonacademic which would not have been possible without his patient, down to earth and compassionate personality. I am truly privileged that I could avail such rich scientific expertise and I thank you both from the bottom of my heart for such an enriching experience!

I would like to convey my gratitude to Prof. Wim Goedheer for providing his extensive theoretical insights, and his kindness when I was in Nieuwegein. I would like to thank the committee members, Prof. Tom Gregorkiewicz, Prof. Jaap Dijkhuis, Prof. Marjolein Dijkstra, Prof. Petra de Jongh and Prof. Peter van der Straten for their quick feedback and comments on this thesis. I genuinely wish to thank Prof. Jaap Dijkhuis who has always had a kind word to spare, which meant a lot to me. I would also like to thank Marcel Di Vece for his encouragement and optimism towards my work.

I would like to thank my collaborators, Marcel Verheijen and Monja Kaiser from PINS (Philips Innovation Service) for the innumerous colorful TEM images which have adorned my thesis! It was a certainly a laborious task, catching my tiny particles under your powerful microscope, but we triumphed and translated my blob of particles to informative high resolution images. Special thanks to Olaff Steinke and Ulf Stephan from FAP (Forschungs- und Applikationslabor Plasmatechnik) Dresden, for your help in realizing the plasma reactor and always providing me with useful tricks and tips every time we had trouble igniting the plasma. Sincere thanks to Maria and the FOM team for taking care of the extensions and handling the finances throughout my PhD and especially during the movement of the lab.

I am grateful to all my colleagues at Utrecht University and High tech Campus for their support, long coffee breaks, lab babysitting and friendship! Thank you so much Riny for

all your help with the paper work and house hunting during my initial days at Utrecht. Thank you so much Pim for all the Dutch translations, Raman peak fitting software and many other things and just being the generous and compassionate person that you are! Merci beaucoup Jan Willem for picking me up from the airport, being such a charming office mate and providing me with all the gossips in the group and sharing all your knowledge about women, HF Dip and hetrojunction solar cells! A big thanks to the extraordinary technician team Caspar, Karine, Martin, Arjen, Bart, Ioannis for your invaluable help with repairing and maintaining ASTER, PASTA and SALSA and all the safety training. Your safety training came a long way while working with highly toxic and inflammable gases and coming out unscathed. Special mention to them for helping pack and move the lab in record time! While setting up and experimenting I have broken and damaged ASTER in more ways than you can imagine, but you have always been one step ahead of me and helped me fix it back! Klass and Marteen, thanks for adopting all our lab equipment and giving me the freedom to use all the characterization equipment available. Casper and Diewertje, you were the first Master students I supervised and it was such a pleasure learning plasma physics with you!

A big thanks to Henriette, Lourens, Silvester, Kees, Yinghuan, Jan Willem and Pim for painstakingly proof reading my thesis! Thank you so much Diederick for such a great time in Toronto! It was one hell of trip, thanks for being my chauffer, although I was scared to death when I learnt it was the first time you were driving a car after you got your license. It was so much fun spotting wolves and bears together in the wild! Dank je wel Minne for trying to teach me Dutch and bike like the Dutch, although you failed miserably at both! Marites, I cannot thank you enough for your hospitality at your home and such amazing Philippine's food and desserts and your guidance during my job hunting. Thank you so much Silvester, Yinghuan, Zachar, Xin, Jessica for being so warm and welcoming. Zachar, my FOM companion, Danke, for fun times we've had during our long flights and insightful conversations. Ioannis, you came like an angel when nothing in the lab seemed to work and you took things in control and always fixed things up! Thank you so much for sticking by and cheering us up with your fancy cakes! Henriette, Pim, Lourens, Yinghuan, Ioannis and Kees, I cannot imagine surviving those long hours of deposition, if it was not for your company. Our all-time favorite conversation was if we will get through the tough days and make it, and I am so proud we all have exceeded our own expectations with our work. It's comforting to have some company in a sinking ship! Caterina, thank you so much for being my Paranimf, you have always been so cheerful and supportive! Grazie for learning to cook so many delicious vegetarian dishes for me, the incredible Corsica trip and for giving the best presentations the group has witnessed!

Phew! Seven long years! End of an era! It has given me endless memories and some friends for life! Deepa, my partner in crime! You were partly the reason I came to Netherlands and now Netherlands feels like home! Thanks for always making things seem much easier than they were! Ram, Sai, Suresh, Prajakta, Deepa, thanks for providing me with a strong foundation in cooking and the great times, dinner, movie nights we had in

Bunnik house! Ram, thank you so much for your help with moving! A very special thanks to my Eindhoven gang (Mukul, Archana, Preetham, Hrishi, Gayathri, Mrinal, Vaishali, Chetna, Shubhendu, Mrunmayee, Siddesh, Pooja, Arjun, Mayur, Prachi, Bobby, Sneha, Vidya) for the wonderful trips, innumerous dinners and parties, violent Pictionary games and some of the best times in Netherlands! Sneha, Archana, Vidya I've always admired your kind heart and brave spirit! Thank you so much Vidya for so graciously accepting to be my parnimph and being so eager to do your paranimph duties and for all your long mails which I enjoy reading profusely! Eindhoven and you guys was like home, away from home.

My Integrated MSc batch working in some of the best research labs around the world has always been a very special inspiration! Manu, thanks for providing me with reference papers at lightning speed. Thanks to Jamuna for always motivating me to finish my thesis and sharing my little joys. Nikhil, thanks for being on WhatsApp, most times! Harin, Kavana and Nu, I cannot thank you girls for putting up with all my frustrating woe laden PhD stories and making me feel better and stronger at the end of it.

A very special gratitude to Gopal sir for the opportunity he provided at TIFR, laying a firm foundation to my future world. I would like to extend my gratitude to various people who mentored me at various stages, shared their invaluable experiences and nourished my growth, a few of them being Usha Maam, Abhas Mitra, H. S Mani, M.V. N. Murthy, N.D Haridas, R. Srinivasan and all my professors at University of Mysore. I would like to thank my colleagues at UL, especially Willem Lysen for adjusting the group meetings to suit my convenience.

I shall forever be indebted to my family for allowing me to pursue my dreams and being my biggest strength. Sachin, I have been a very difficult person to deal with, during the last stressful year; with a full time job, travelling and writing my thesis. Thanks for reassuring me during my bad days, subduing me during my ecstatic days and maintaining the calm during all the chaos! Thanks to my brother, Achyu for creating difficult footsteps for me to follow and for nagging me to complete my PhD. Appa and Amma, my eternal cheer leaders; for teaching me to do the hardest things with a smile!

Curriculum Vitae

Personal information

Name: Akshatha Mohan

Place of birth: Mysore, India

Education Information

2010 - 2017	PhD in Physics on “Pulsed plasma synthesis of Si and SiGe Nanocrystals”, Utrecht University, The Netherlands
2004 - 2009	Integrated MSc in Physics, University of Mysore, India

Employment Information

2016 - present	Technical Analyst at UL transaction security, Leiden, The Netherlands
2016 - present	Technical Consultant at Adyen Payments, Amsterdam, The Netherlands
2010 - 2016	PhD researcher, FOM , Utrecht, The Netherlands
2009 - 2010	Junior research fellow, TIFR, Mumbai, India
2008	Visiting project student, BARC, Mumbai and RRI, Bangalore, India